The Astrophysical Journal, 970:95 (32pp), 2024 July 20 https://doi.org/10.3847/1538-4357/ad4a54

The Coherent Magnetic Field of the Milky Way

Michael Unger[1,2] and Glennys R. Farrar[3]
[1] Institute for Astroparticle Physics (IAP), Karlsruhe Institute of Technology (KIT), Karlsruhe, Germany; michael.unger@kit.edu
[2] Institutt for fysikk, Norwegian University of Science and Technology (NTNU), Trondheim, Norway
[3] Center for Cosmology and Particle Physics, Department of Physics, New York University, New York, NY 10003, USA; gf25@nyu.edu
Received 2024 February 6; revised 2024 May 9; accepted 2024 May 10; published 2024 July 19

Abstract

We present a suite of models of the coherent magnetic field of the Galaxy based on new divergence-free parametric functions describing the global structure of the field. The model parameters are fit to the latest full-sky Faraday rotation measures (RMs) of extragalactic sources and polarized synchrotron intensity (PI) maps from the Wilkinson Microwave Anisotropy Probe and Planck. We employ multiple models for the density of thermal and cosmic-ray electrons in the Galaxy, needed to predict the sky maps of RMs and PI for a given Galactic magnetic field (GMF) model. The robustness of the inferred properties of the GMF is gauged by studying many combinations of parametric field models and electron density models. We determine the pitch angle of the local magnetic field ($11^\circ \pm 1^\circ$), explore the evidence for a grand-design spiral coherent magnetic field (inconclusive), determine the strength of the toroidal and poloidal magnetic halo fields below and above the disk (magnitudes the same for both hemispheres within ≈10%), set constraints on the half-height of the cosmic-ray diffusion volume ($\gtrsim$2.9 kpc), investigate the compatibility of RM- and PI-derived magnetic field strengths (compatible under certain assumptions), and check if the toroidal halo field could be created by the shear of the poloidal halo field due to the differential rotation of the Galaxy (possibly). A set of eight models is identified to help quantify the present uncertainties in the coherent GMF spanning different functional forms, data products, and auxiliary input. We present the corresponding sky maps of rates for axion–photon conversion in the Galaxy and deflections of ultrahigh-energy cosmic rays.

Unified Astronomy Thesaurus concepts: Milky Way magnetic fields (1057); Galaxy magnetic fields (604); Milky Way Galaxy physics (1056); Cosmic rays (329); Cosmic ray astronomy (324)

1. Introduction

Spiral galaxies are known to be permeated by large-scale magnetic fields with energy densities comparable to the turbulent and thermal energy densities of the interstellar medium; see, e.g., Beck (2016) for a recent review. A good knowledge of the global structure of these fields is important for understanding their origin, inferring their effect on galactic dynamics, estimating the properties of the diffuse motion of low-energy Galactic cosmic rays, and studying the impact of magnetic deflections on the arrival directions of extragalactic ultrahigh-energy cosmic rays. The Galactic magnetic field (GMF) is also important for new physics studies, for instance, axion–photon conversion in the GMF or the interpretation of possible signatures of astrophysical dark matter annihilation.

The determination of the large-scale structure of the magnetic field of our Galaxy is particularly challenging since one must infer it from the vantage point of Earth, located inside the field. Previous attempts to model the GMF are summarized by Jaffe (2019). In this paper, we focus on the coherent magnetic field of the Galaxy, leaving the study of its turbulent component to the near future. Following Jansson & Farrar (2012a; hereafter JF12), we derive the GMF by fitting suitably general parametric models of its structure to the two astrophysical data sets that are the most constraining of the coherent magnetic fields: the *rotation measures* (RMs) of extragalactic polarized radio sources and the *polarized intensity* of the synchrotron emission of cosmic-ray electrons in the Galaxy.

The relation of these two astrophysical observables to the magnetic field is detailed in Section 2, followed by a description of the RM and PI data in Section 3. The interpretation of these data relies on the knowledge of the three-dimensional density of thermal electrons and cosmic-ray electrons in the Galaxy. We discuss these *auxiliary models* in Section 4. The parametric models of the GMF investigated in this paper are introduced in Section 5, and the model optimization is described in Section 6.

The combination of different data sets, auxiliary models, and parametric functions yields an ensemble of GMF models that reflect the uncertainties and degeneracies inherent in the inference of the global field structure from the limited information provided by the RM and PI data. In Section 7, we narrow down these model variants to a few benchmark models that encompass the largest differences within the ensemble.

A typical application of the global magnetic field models is the inference of the arrival direction of cosmic rays at the edge of the Galaxy and the determination of the conversion probability of axions in the magnetic field of the Galaxy. In Section 8, we briefly comment on the implications of our study on these topics.

We conclude this paper by giving a brief summary of our findings in Section 9 and addressing the question: what is known and not known about the coherent magnetic field of the Galaxy?

2. Observables

In this work, we derive the global structure of the GMF from two astrophysical observations, Faraday RMs and PI. These

two quantities provide complementary information on the parallel and perpendicular components of the coherent magnetic field along the line of sight from the observer at Earth through the Galaxy.

The RM relates the Faraday-rotated polarization angle χ of an astrophysical source observed at a wavelength λ to its intrinsic polarization angle χ_0 after passing through the magnetized plasma of the Galaxy via

$$\chi(\lambda) = \chi_0 + \mathrm{RM}\ \lambda^2. \tag{1}$$

We follow the IAU convention based on Manchester (1972; see also Ferrière et al. 2021) in which the RM is positive for a photon traveling in the same direction as the magnetic field points through an ambient medium with free electrons. In our notation, taking the observer to be at the origin and the positive unit vector $\boldsymbol{u}_r$ pointing away from the observer, RM is given by

$$\mathrm{RM} = -C_{\mathrm{RM}} \int_0^\infty n_\mathrm{e}(\boldsymbol{x}(r))\boldsymbol{B}(\boldsymbol{x}(r))\,\boldsymbol{u}_r\,dr,$$

where the position $\boldsymbol{x}$ at a distance r from an observer located at $\boldsymbol{x}_0$ is $\boldsymbol{x}(r) = \boldsymbol{x}_0 + \boldsymbol{u}_r\, r$,[4] n_e denotes the density of the thermal electron plasma in the interstellar medium (ISM), and $C_{\mathrm{RM}} = e^3/(8\,\varepsilon_0\,\pi^2\,m_e^2\,c^3) \approx 0.8119\,(\mathrm{rad\,m^{-2}})\,(\mathrm{cm^3\,pc^{-1}}\,\mu\mathrm{G})$ (e.g., Bradt 2008). Thus, RM is negative for a magnetic field oriented away from the observer.

The interpretation of RM becomes more complicated if one considers the possibility of a small-scale correlation or anticorrelation of magnetic fields and thermal electrons. An anticorrelation could arise if the magnetic field is in pressure equilibrium with the thermal electron plasma. In this case, the local Faraday rotation would be systematically diminished, and interpreting the RM assuming no anticorrelation would underestimate the magnitude of the integrated line-of-sight magnetic field. A positive correlation could be caused by compression enhancing both the magnetic field and electron density. These effects were studied by Beck et al. (2003; see also Seta & Federrath 2021), who provide the following approximate relation between the RM for the uncorrelated case, RM_0, and the general case with a correlation coefficient κ,

$$\mathrm{RM} = \mathrm{RM}_0\left(1 + \frac{2}{3}\,\kappa\,\frac{\langle b^2\rangle}{B^2 + \langle b^2\rangle}\right), \tag{2}$$

where B denotes the coherent field and $\langle b^2\rangle$ is the mean squared field strength of the turbulent magnetic field. In one of our model variants, we will allow for a nonzero κ.

The *polarized synchrotron intensity (PI)* originates from cosmic-ray electrons and positrons spiraling in the coherent magnetic field of the Galaxy. The observed PI depends on the cosmic-ray electron-density-weighted incoherent superposition of synchrotron emission along the line of sight. For long wavelengths, the effect of Faraday rotation along the path between emission and observation needs to be taken into account. At the magnetic field strengths and frequencies relevant for this analysis (a few μG and 30 GHz), the typical cosmic-ray energy responsible for synchrotron emission is of the order of tens of GeV (e.g., Longair 2011), and the Faraday depolarization is not significant.

The relationship between the synchrotron volume emissivity and the magnetic field strength is particularly simple for the case of electrons with an energy distribution following a power law, $n_{\mathrm{cre}}(E) = n_0\,E^{-p}$:

$$j_\nu \propto n_0\,\nu^{\frac{-(p-1)}{2}}\,B_\perp^{\frac{p+1}{2}} \overset{p=3}{=} n_0\,\nu^{-1}\,B_\perp^2, \tag{3}$$

where in the last step, the approximation of $p \approx 3$ was used, which is applicable for a canonical E^{-2} spectrum at the source softened to E^{-3} due to energy losses from synchrotron cooling and inverse Compton scattering.

However, the cosmic-ray electron spectrum is not expected to be an exact power law (e.g., Orlando & Strong 2013). To obtain the local volume emissivity at the position $\boldsymbol{x}$, we therefore integrate the single-electron emissivity over energy,

$$j_\nu(\boldsymbol{x}) = \int_0^\infty j(E, B_\perp(\boldsymbol{x}))\,n_{\mathrm{cre}}(\boldsymbol{x}, E)\,dE, \tag{4}$$

where the emissivity $j(E)$ of an electron of energy E is given in Equations (8.56) and (8.57) of Longair (2011) and can be conveniently evaluated using the synchrotron functions provided by the GSL library.[5] The integral over the emissivities along the line of sight given the three-dimensional distribution of $n_{\mathrm{cre}}(\boldsymbol{x}, E)$ and $B_\perp(\boldsymbol{x})$ yields the Stokes parameters Q and U of the PI. Q and U add up quadratically to the total PI[6] via

$$\mathrm{PI}^2 = Q^2 + U^2, \tag{5}$$

and their ratio defines the observed polarization angle,

$$\psi_{\mathrm{PA}} = \frac{1}{2}\arctan(U/Q). \tag{6}$$

ψ_{PA} is perpendicular to the line-of-sight average of the n_{cre}-weighted magnetic field angle in the plane of the sky,

$$\langle\psi_{\mathrm{mag}}\rangle = \psi_{\mathrm{PA}} + \pi/2; \tag{7}$$

i.e., the analysis of Q and U is sensitive to both the strength and the orientation of the perpendicular projection of the magnetic field along the line of sight.

Isotropic random magnetic fields do not contribute to the PI, but an anisotropic random field results in a net PI, because Q and U define only the plane of polarization and are thus invariant under a 180° rotation of the magnetic field. Anisotropic random magnetic fields can originate from magnetohydrodynamic turbulence (Goldreich & Sridhar 1995) or from the stretching or compression of a flux-frozen isotropic random magnetic field (Laing 1980). The latter can lead to basically one-dimensional fluctuations along a preferred orientation, termed "ordered random" by Jaffe et al. (2010) or "striated" by Jansson & Farrar (2012a). A striated random field does not make a net contribution to the RM since the contributions of opposite-sign regions cancel out. However, it does contribute to the polarized synchrotron emission since that depends only on the orientation and not the direction of the

[4] Throughout this work, we assume an observer at $\boldsymbol{x}_0 = \boldsymbol{x}_\odot = (-r_\odot, 0, z_\odot)$ in a right-handed Galactic coordinate system. The vertical distance of the Sun from the Galactic plane $z_\odot$ is somewhere between 0.006 ± 0.001 kpc (Joshi et al. 2016) and 0.026 ± 0.003 kpc (Majaess et al. 2009) and can thus be neglected for the purpose of this work; i.e., we set $z_\odot \to 0$. For the distance of the Sun to the Galactic center, we adopt the precise measurement of the GRAVITY collaboration, $r_\odot = 8.178 \pm 0.025$ kpc (Abuter et al. 2019).

[5] https://www.gnu.org/software/gsl/doc/html/specfunc.html#synchrotron-functions

[6] Note that instrumental noise on Q and U leads to a positive bias in PI when estimated via Equation (5) (e.g., Wardle & Kronberg 1974). Since we will fit the measured Q and U data, but not PI, the bias is not important for this work.

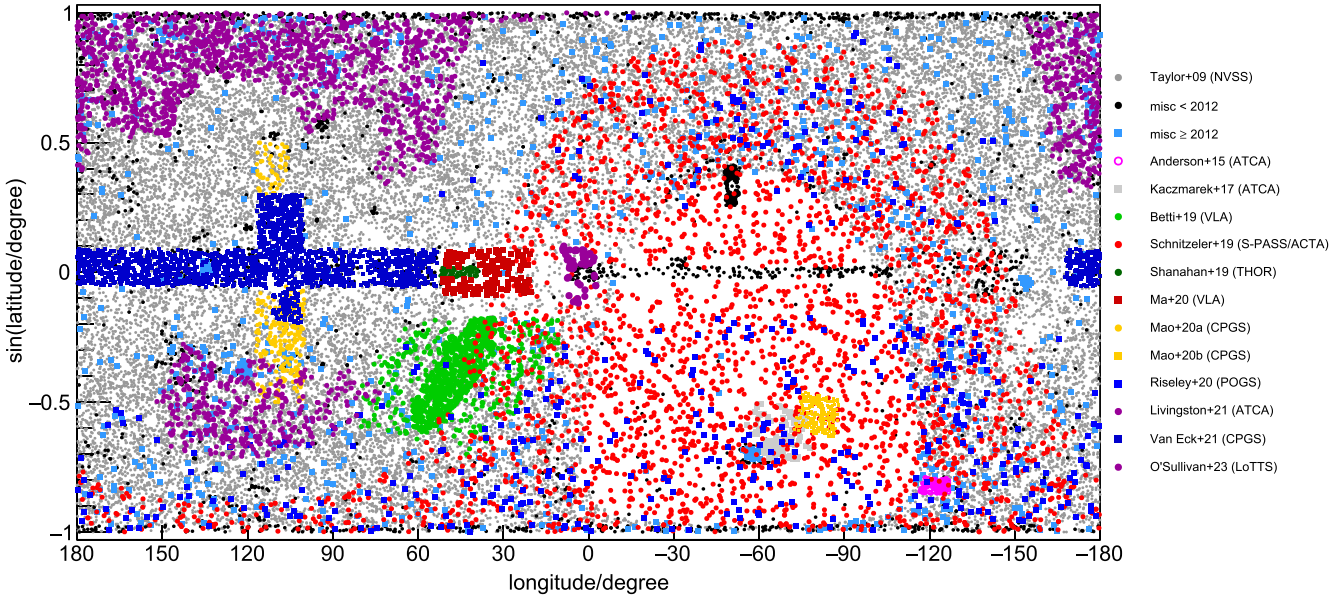

Figure 1. Overview of the RM data used in this analysis. Measurements are shown in Galactic coordinates using a cylindrical projection that visually preserves the point density per solid angle. RMs published before 2012 (and thus available for the JF12 analysis) are shown as gray and black circles.

field. Jansson & Farrar (2012a) considered different values of the striation factor for different components of the field but found them to be all the same. Here we model the possible striation via a simple spatially independent multiplicative factor to the coherent field,

$$B' = (1 + \xi)B. \tag{8}$$

The striation factor ξ is related to the striation factor β used in JF12, for which a cosmic-ray electron energy spectrum with a spectral index of $p = 3$ was assumed, via $(1 + \xi) = \sqrt{1 + \beta}$.

3. Data Products

3.1. RMs

We assemble a sky map of extragalactic RMs based on individual measurements from various catalogs and surveys as illustrated in Figure 1. Most of the currently known extragalactic RMs were derived by Taylor et al. (2009) from the two-band polarization data of the NVSS survey (Condon et al. 1998) leading to 37,543 RMs with a decl. of $> -40°$. Since only two frequencies are available in this data set, the derived RMs are susceptible to $n\pi$ ambiguities in Equation (1) for high values of |RM|. We replace the values of 20 of these high-RM sources with the ones obtained by the broadband follow-up observations of Ma et al. (2019); three are discarded based on these reobservations.

For measurements predating the year 2014, we use the catalog of 4553 high-quality RMs curated by Xu & Han (2014). Notable surveys with $N_{\rm RM} > 100$ collected in this catalog are from Simard-Normandin et al. (1981), Broten et al. (1988), Brown et al. (2003, 2007), Klein et al. (2003), Broderick et al. (2007), Feain et al. (2009), Heald et al. (2009), Mao et al. (2010, 2012a, 2012b), and Van Eck et al. (2011).

A total of 3220 RMs in the southern equatorial hemisphere are taken from the S-PASS/ATCA wide-band radio polarimetry survey (version 0.9) of Schnitzeler et al. (2019; applying the quality cuts given in Section 4 of that paper and requiring emission at a single Faraday depth as well as model fits with $\chi^2/\mathrm{ndf} < 10$). This survey is of particular significance, since it complements the sky coverage of the NVSS survey. GMF model fits predating the S-PASS/ATCA release, e.g., JF12, were constrained by only a very small number of RMs in the 18% southernmost equatorial sky.

A further 5999 RMs published in the years 2014–2022 are taken from the data compilation of Van Eck et al. (2023; v1.1.0 at Van Eck et al. 2022). Notable surveys with $N_{\rm RM} > 100$ in this compilation are from Farnes et al. (2014), Anderson et al. (2015), Kaczmarek et al. (2017), O'Sullivan et al. (2017), Betti et al. (2019), Ma et al. (2020), Riseley et al. (2020), and Van Eck et al. (2021). In addition, we include the 2461 recent extragalactic RMs of O'Sullivan et al. (2023).

In this data set of 53,773 RMs, we identify obvious multiple measurements of the same extragalactic object if their coordinates correspond to the same pixel ID on a high-resolution Hierarchical, Equal Area, and iso-Latitude Pixelation of the sphere (HEALPIX) sky map with $N_{\rm side} = 2048$ (angular pixel width of 1.′7).[7] All duplicate RMs but the measurement with the best frequency coverage are dropped, leaving 47,054 RMs of unique extragalactic objects.

In the next step of data selection, we apply a two-pass algorithm to reject outliers caused by either a large source-intrinsic RM or a wrong resolution of the $n\pi$ ambiguity. The procedure is similar in spirit but different in detail to that used for the data set of JF12. For each RM measurement, we accumulate surrounding measurements within an angular collection radius starting at 1°. The collection radius is increased until a sample of at least 10 independent surrounding RM measurements are found that differ by less than three median absolute deviations from the median RM of that

[7] The HEALPIX package is used to subdivide the sky into equal-area pixels (Górski et al. 2005). The resolution $N_{\rm side}$ of a HEALPIX map is related to the number of pixels via $N_{\rm pix} = 12\,N_{\rm side}^2$. For a map with $N_{\rm side} = 16$, the standard resolution used in this paper, the number of pixels is $N_{\rm pix} = 3072$ with an angular width of approximately $\theta \approx \sqrt{4\pi/N_{\rm pix}}\ 180°/\pi = \sqrt{3/\pi}\ 60°/N_{\rm side} = 3.°66$

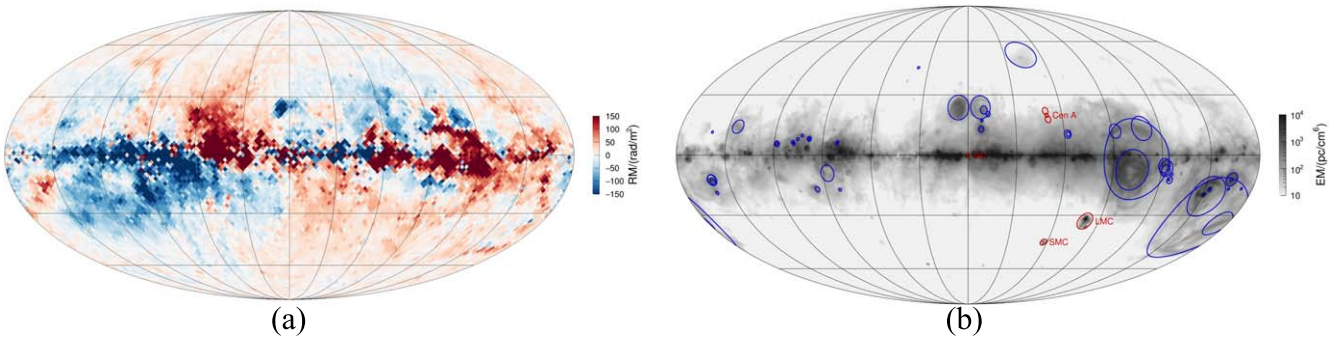

Figure 2. Sky map of RMs (left) and masked regions (right). (a) Sky map of extragalactic RMs (44,857 RMs averaged over $N_{\rm side} = 32$ HEALPIX pixels). The color scale is saturated at $|{\rm RM}| \geqslant 150$ rad m^{-2}. (b) Masked region for the RM analysis. Selected astrophysical objects (red) and H II regions (blue). The gray-scale background shows the sky map of emission measures.

sample. In the second pass, these sources are then used to calculate the mean and standard deviation of the RM in the region surrounding each object. We keep objects if their RM value is closer than three standard deviations from the surrounding mean.

The remaining 44,857 RMs are displayed in Figure 2(a). For this figure, we show the average of RMs in an $N_{\rm side} = 32$ HEALPIX map.[8] For the purpose of this figure, 1524 pixels (12%) without a measurement were inpainted with the average of their surrounding pixels. At this somewhat higher resolution than the one used for the analysis (see below), both the large- and small-scale features of the extragalactic RMs are visible. The most salient large-scale features of the RM sky have been known since the early advent of RM catalogs; see, e.g., the discussion in Andreasyan & Makarov (1988) and Han et al. (1997). For the inner Galaxy (longitudes between $-90°$ and $90°$), there is an antisymmetry in both the longitude and latitude of the sign of the average RMs, whereas in the outer Galaxy (longitudes from $90°$ to $270°$), the average RMs have the same sign above and below the plane, as summarized by the following schematic of an RM sky map,

$$\mathrm{RM}(\ell, b) \approx \left(\begin{array}{cc} - & + \\ \hline - & + \end{array}\right)\left(\begin{array}{cc} - & + \\ \hline - & + \end{array}\right). \tag{9}$$

In addition, many small-scale features can be identified, some of which can be attributed to foreground objects. We remove some of the most obvious regions, indicated by circles in Figure 2(b). First, we discard lines of sight if they pass through magnetized objects with a large angular size, i.e., M31, the Small and Large Magellanic Clouds, Centaurus A (core and lobes), and the Galactic center. The excluded regions around these objects are shown in red in Figure 2(b). Second, we deselect RMs if the thermal electron density along the line of sight is dominated by a single object. Such local overdensities in the diffuse warm ionized medium (WIM) are caused by the ultraviolet light of young massive stars ionizing the ISM around them, creating an H II region. RMs in lines of sight passing through H II regions are often dominated by the product $n_{\rm e} B_{\parallel} \Delta$ inside the region of thickness Δ; see, e.g., Heiles et al. (1981) and Harvey-Smith et al. (2011). These RMs are thus not representative of the large-scale GMF. Regions of locally enhanced thermal electron density can, e.g., be identified by the emission measure, ${\rm EM} = \int_0^\infty n_{\rm e} dl$, which is displayed in Figure 2(b) based on the composite of Hα surveys (VTSS, SHASSA, and WHAM) from Finkbeiner (2003). More than 8000 Galactic H II regions are known in the Galaxy (Anderson et al. 2014), but most of them are far away, and thus of small angular extent, and/or at low Galactic latitudes, where the overall RM integral through the plane is large enough that it is not overshadowed by the contribution of a single H II region. We therefore deselect only the lines of sight that overlap with an H II region if it is either of large angular extent ($r > 10°$) or at high latitudes, $|b| > 5°$. These regions are displayed in blue in Figure 2(b) if their size is $>0.^\circ 5$.

The final 41,686 RMs are then binned in 3072 angular pixels of an $N_{\rm side} = 16$ HEALPIX map with an angular diameter of $\sim 3.^\circ 7$. For each pixel, we calculate the mean and unbiased sample variance to be used in the model optimization (see Equation (48) below). If the number of RMs within 1 pixel is <10, then the variance (but not the mean) is calculated using the 10 RMs with the closest angular distance to the center direction of the pixel. This leads to 2838 pixels with RM data, where 46 pixels are excluded because no data were observed in this direction and another 188 pixels are excluded by the masks displayed in Figure 2. The final masked and binned RM data are shown in Figure 10(b) in Section 7.

3.2. Polarized Synchrotron Emission

The polarized synchrotron emission from the Galaxy is best observed at high frequencies, where the depolarization of the signal due to Faraday rotation is negligible. At Faraday depths typical for the Galaxy, the change in polarization angle becomes negligible in the tens of GHz range; see Equation (1). The received PI in units of Rayleigh–Jeans antenna temperature, $T = c^2/(2\nu^2 k_{\rm B})$PI, decreases as $\nu^{\beta_{\rm s}}$ with frequency. Here the synchrotron spectral index $\beta_{\rm s} \approx -3$ for a cosmic-ray electron spectrum with index $p = 3$; see Equation (3). Another source of polarized emission from the Galaxy originates from thermal dust with a spectral index of $\beta_{\rm d} \approx +1.6$ (Ade et al. 2015). Empirically, the crossover between the two components is at around 100 GHz.

The "sweet spot" for the observation of synchrotron emission is therefore at high enough frequencies such that Faraday depolarization is negligible, but not too high, such that

[8] This and subsequent maps shown in this paper are area-preserving Mollweide projections of the sky in Galactic coordinates with the Galactic center at the origin. The longitude increases toward the left from $0°$ at the center to $+180°$ and decreases toward the right from $+360°$ at the center to $+180°$ (or, equivalently, from $0°$ to $-180°$).

the signal is not dominated by polarized dust emission. The Wilkinson Microwave Anisotropy Probe (WMAP) and Planck satellites operated in this frequency regime, with a frequency threshold of 20 and 30 GHz, respectively.

From WMAP, we use the final 9 yr results (DR5) on the polarized synchrotron emission at 22.5 GHz provided at a HEALPIX resolution of $N_{\rm side} = 64$ (Bennett et al. 2013). Four variants of Q and U sky maps are available, differing mainly by the constraints placed on $\beta_{\rm s}$ during analysis. These four variants of the derived PI are in good agreement outside of the Galactic plane, which is masked in our analysis (see below). We use the "base" model, which is the most data-driven variant in which the synchrotron spectral index was allowed to float freely in each sky pixel. We inpaint the pixels that are flagged as having an erroneous component separation (2.7%) with the Q and U averages of their eight surrounding neighbor pixels.

From Planck, we use the third release (R3.0) of the polarized synchrotron foreground at 30 GHz derived from component separation using the COMMANDER software (Akrami et al. 2020). These sky maps are provided at a high resolution of $N_{\rm side} = 2048$, and we average the Q and U values to obtain maps with $N_{\rm side} = 64$ to match the resolution of WMAP. During this averaging, spurious outliers in the high-resolution maps are identified and discarded if the value is more than 5σ away from the median of the values within the low-resolution pixel. This procedure removes 0.18% of the high-resolution data points.

We then combine the Q and U sky maps from WMAP and Planck into a lower-resolution map at $N_{\rm side} = 16$ by taking the simple arithmetic average of all 32 measurements in each pixel (16 from each experiment). WMAP intensities are extrapolated to the Planck frequency with a spatially constant synchrotron spectral index of $\beta_{\rm s} = -3.15$ based on the mean value predicted by our simulations described in Section 4.2. Note that due to the proximity of the WMAP and Planck frequencies, even a large difference between the actual and assumed value of $\Delta\beta_{\rm s} = 0.2$ would introduce a variation in extrapolated intensity of only $1 - (22.5\ {\rm GHz}/30\ {\rm GHz})^{\pm\Delta\beta_{\rm s}} = \pm 6\%$. The variance of the 32 data points per pixel is used to calculate the weights in the χ^2 minimization as discussed in Section 6.

The Stokes parameters derived by the WMAP and Planck collaborations exhibit systematic large-scale differences; see Figure 22 in Appendix A. These differences could be attributed either to large-scale spatial variation of the synchrotron spectral index or to residual calibration uncertainties in one or both of the data sets. A combined analysis of WMAP and Planck data was recently presented by the COSMOGLOBE Collaboration (Watts et al. 2023, 2024), performing the component separation and the calibration of the data sets simultaneously. We will use the COSMOGLOBE results as an alternative to our average and study the effect on the parameters of GMF models in Section 7.

Our combined maps of Stokes Q and U and the PI of the Galactic synchrotron emission at 30 GHz are shown in Figure 3. As can be seen, both Q and U exhibit large-scale features, which we will interpret in the following as imprints of the large-scale features of the GMF. However, care must be taken not to include regions with strong local features that could bias our fits. We therefore mask out some regions of the sky in fitting to the GMF parameters.

The elements of our mask when fitting the PI data are shown in Figure 4. Red indicates the mask used in the original WMAP analysis. It excludes regions of high PI along the Galactic plane and the north polar spur and pixels containing strong extragalactic sources such as the radio lobes of Centaurus A. The blue region depicts the additional PI mask introduced by Jansson & Farrar (2012a) mainly to remove a presumably local, high-latitude polarized emission at $90° < \ell < 180°$. Finally, we also mask the green regions as an attempt to remove further large circular arcs (called loops, spurs, or filaments) visible in PI. Here we exclude data in the direction of loops I–IV, as defined by Berkhuijsen et al. (1971), and further filaments identified by Vidal et al. (2015). The union of the above leads to our final PI mask. The cumulative application of these three masks leaves 73.1% (WMAP), 63.4% (WMAP + JF12), and 57.8% (WMAP + JF12 + loops) of the sky for analysis.

It is worthwhile to note that the exact attribution of features in the polarized radio sky to local or global phenomena in the Galaxy is still under debate; see, e.g., Lallement (2023). Some of the loops and filaments could be caused by local supernova remnants expanding into the surrounding ambient magnetic field (Spoelstra 1973), whereas others might be related to large-scale magnetized outflow from the Galactic center (Carretti et al. 2013), related to the so-called "Fermi bubbles" observed in gamma rays (Ackermann et al. 2014) and surrounded by "eROSITA bubbles" in X-rays (Predehl et al. 2020). These are shown as violet and orange regions in Figure 4, demonstrating that our mask retains some directions that contain contributions from the Fermi and eROSITA bubbles.

4. Auxiliary Models

4.1. Thermal Electrons

The magnetized plasma responsible for the Faraday rotation of extragalactic radio sources resides mostly in the WIM of the Galaxy (e.g., Ryden & Pogge 2021). To interpret the RMs, a three-dimensional model of the density, $n_{\rm e}(\boldsymbol{x})$, of these free thermal electrons is needed. Here we use two models of $n_{\rm e}$: NE2001 of Cordes & Lazio (2002) and YMW16 of Yao et al. (2017). Both models were tuned to describe the *dispersion measure* (DM) of Galactic pulsars, which is given by the line-of-sight integral from Earth to the pulsar at a distance d, ${\rm DM} = \int_0^d n_{\rm e}(\boldsymbol{x}(r))\, dr$. More than 3000 pulsars with measured DMs are listed in the current version (1.70) of the ATNF pulsar catalog (Manchester et al. 2005), but only for a few is the distance d well known: NE2001 was tuned to the DMs of 112 pulsars, and YMW16 used 189. Given the large number of parameters of these models (e.g., the YMW16 model has 82 fixed parameters and 32 fitted parameters) and the scarcity of data, they rely, to a large extent, on astrophysical priors for the geometrical topology of the thermal electron density.

Particularly important for the modeling of the large-scale structure of the GMF is the vertical structure of the Galactic WIM, which is relatively well constrained by the DMs of pulsars in high-latitude globular clusters (Gaensler et al. 2008). Since the fit of NE2001 predates most of these data, we replace the original value of the exponential scale height of the diffuse WIM of $h_{\rm WIM} = 0.95$ kpc with $h_{\rm WIM} = 1.3 \pm 0.2$ kpc as derived by Schnitzeler (2012) for this model. A larger value of $h_{\rm WIM} = 1.67 \pm 0.05$ kpc was inferred by Yao et al. (2017) for their YMW16 model.

An illustration of the thermal electron densities of YMW16 and NE2001 is shown in Figure 5. As can be seen, the two models differ substantially, especially regarding the positions

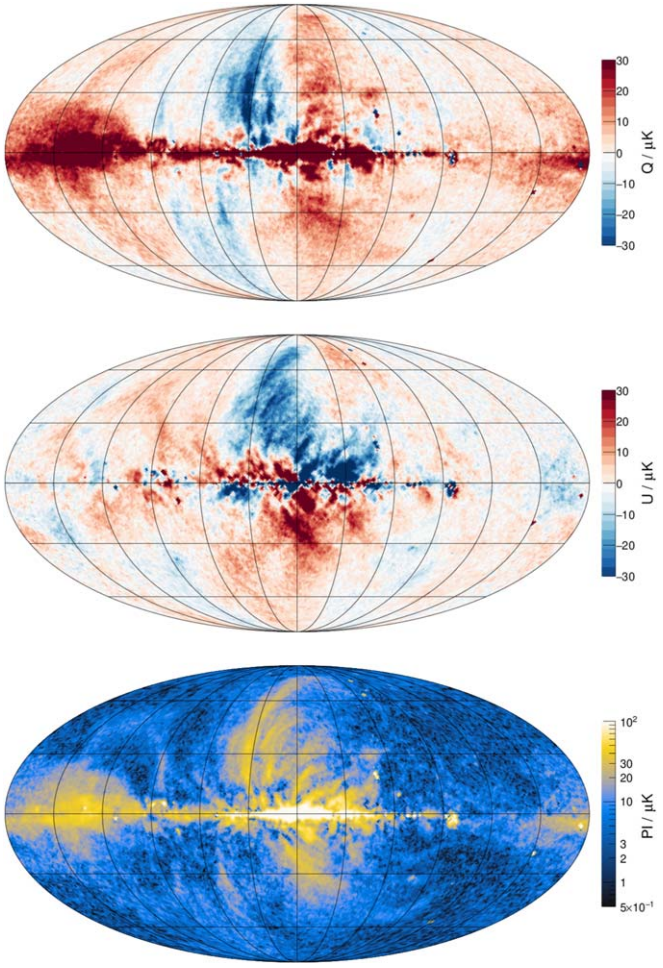

Figure 3. Stokes Q (top panel) and U (middle panel) parameters and PI (bottom panel) from the averaged synchrotron maps of Planck and WMAP at 30 GHz.

and widths of the spiral arms, the density in the molecular ring at $r \approx 5$ kpc and in the Galactic center, and the scale height of the thick disk of the WIM. Whereas YMW16 can predict pulsar DMs with a somewhat higher fidelity than NE2001, the latter model remains a viable alternative to describe the large-scale features of the WIM (e.g., Price et al. 2021). By using both models in our GMF fits, we can study the systematic effects arising from different assumptions on the thermal electron density.

4.2. Cosmic-Ray Electrons

Calculating Galactic synchrotron emission requires not only a model of the GMF but also a model of the three-dimensional density distribution and energy spectrum of cosmic-ray electrons in the Galaxy, $n_{\rm cre}(\boldsymbol{x}, E)$.

In contrast to the purely phenomenological thermal electron models discussed in the previous section, predictions of $n_{\rm cre}$ are based on detailed modeling of the production and propagation of electrons and positrons in the Galaxy (e.g., Moskalenko & Strong 1998) to obtain a steady-state solution of the diffusion equation of cosmic rays in the Galaxy (Ginzburg & Syrovatskii 1964). In its simplest version (sometimes referred to as "plain diffusion"), the defining quantity of the model is the diffusion coefficient of charged particles in the ISM. Most calculations assume a homogeneous and isotropic Galactic

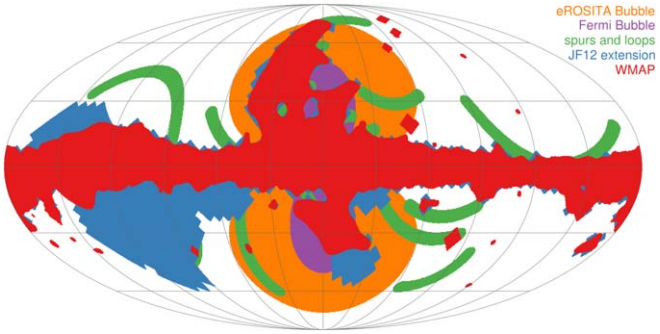

Figure 4. Polarized synchrotron mask used in this analysis. Masked regions are shown in red, blue, and green (see text). For comparison, the outlines of the Fermi and eROSITA bubbles are shown in violet and orange.

diffusion coefficient D within a "diffusion volume" approximated as a cylinder of half-height h_D.

The normalization and rigidity[9] dependence of D is determined from measurements of the fluxes of secondary and primary cosmic-ray nuclei at Earth. The most precise estimates (in terms of the uncertainty of both cosmic-ray flux and nuclear cross sections) are derived from the ratio of the flux of secondary boron nuclei and (mostly) primary carbon nuclei. However, secondary-to-primary ratios can only constrain the ratio, D/h_D (e.g., Maurin et al. 2001). Estimates of D/h_D in a plain diffusion scenario range from $0.03\,{\rm kpc\,Myr^{-1}}$ (Yuan et al. 2017; Génolini et al. 2019) to $0.10\,{\rm kpc\,Myr^{-1}}$ (Cummings et al. 2016) at a reference rigidity of 10 GV.

The degeneracy between h_D and D can in principle be broken by data on "cosmic clocks" (e.g., ^{10}Be/^{9}Be or Be/C), but due to the poor quality of the current data and uncertainties in the spallation cross sections, only mild constraints on the halo height can be derived, and the current estimates of h_D are in the range 2–10 kpc (e.g., Evoli et al. 2020; Weinrich et al. 2020; Maurin et al. 2022). We therefore consider diffusion volumes having $h_D = 2$, 4, 6, 8, and 10 kpc and derive the corresponding $n_{\rm cre}$ for each to allow us to assess the uncertainty in the GMF due to the present uncertainty in h_D. For each of the five different values of the height of the diffusion volume, h_D, we solve the cosmic-ray diffusion equation with the DRAGON program (Evoli et al. 2008).[10]

For each value of h_D, we obtain the diffusion coefficient at 10 GV from $D/h_D = 0.046\,{\rm kpc\,Myr^{-1}}$, and we take the rigidity dependence of $D(\mathcal{R})$ to be the one derived for the "PD2" model of Cummings et al. (2016). At high rigidities ($\mathcal{R} \gtrsim 5$ GV), the diffusion coefficient scales as $D \propto \mathcal{R}^{0.578\pm0.073}$, i.e., compatible with the power-law scaling $\mathcal{R}^{1/2}$, typical for a turbulent magnetohydrodynamical cascade (Iroshnikov 1964; Kraichnan 1965). The spatial distribution of Galactic cosmic-ray sources is taken to follow the radial distribution of pulsars in the Galaxy (Lorimer et al. 2006), used as a proxy for the distribution of supernova remnants, and we use the JF12 magnetic field model to calculate the cooling of cosmic-ray electrons due to synchrotron radiation. The maximum Galactocentric radius of the diffusion volume was set to $R_{\rm max} = 18$ kpc.

[9] The rigidity of a particle with charge Ze and momentum p (energy E) is $\mathcal{R} = pc/(Ze) \simeq E/(Ze)$.

[10] We choose DRAGON over the other widely used solver GALPROP (Strong & Moskalenko 1998) because at the time of setting up our analysis chain, only DRAGON supported spatially varying diffusion coefficients. In this paper, however, we investigate only homogeneous diffusion.

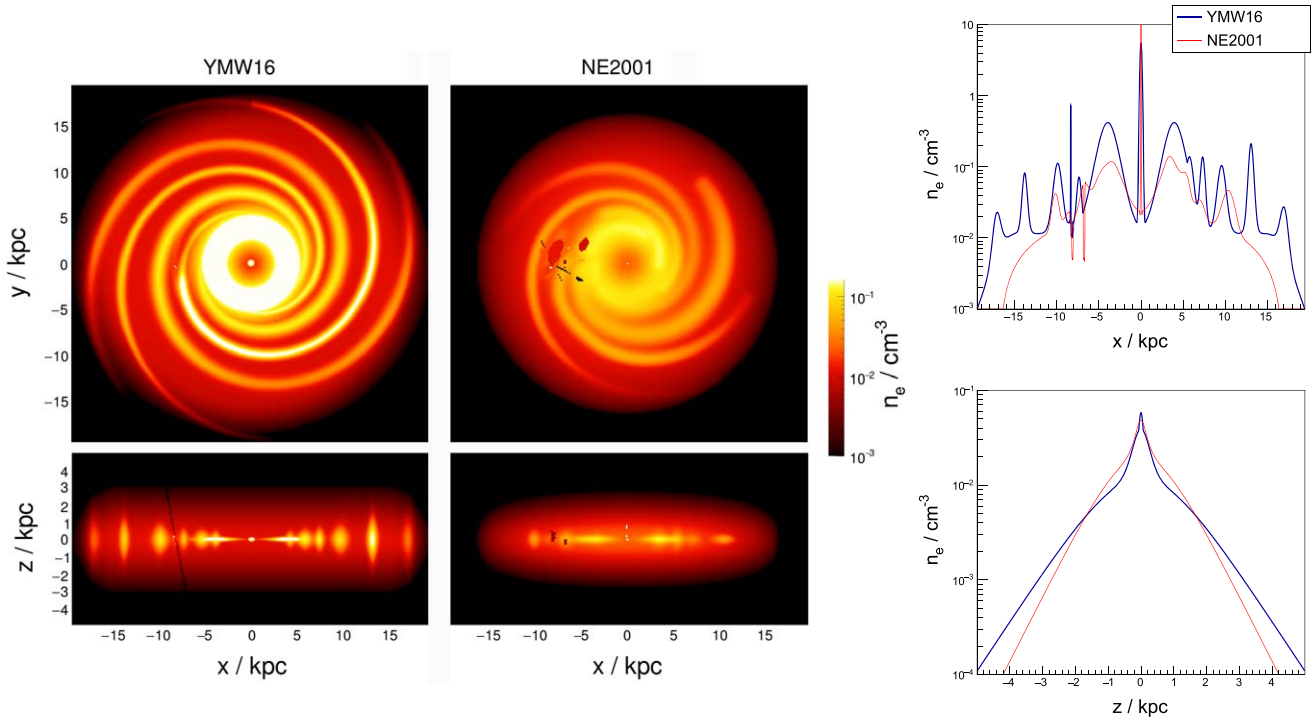

Figure 5. Left: thermal electron density, n_e, for the YMW16 and NE2001 models. The top panel shows the midplane density at $z = 0$, and the bottom panel gives an edge-on view of the density at $y = 0$ in the x–z plane. Structures visible at around the position of the Sun ($\approx(-8.2, 0, 0)$ kpc) are due to the modeled under- and overdensities of the local ISM. Right: thermal electron density along the Galactic x-axis at $z = y = 0$ (top) and along the z-axis at $x = -6$ kpc and $y = 0$.

We constrain the solutions of the diffusion equations by the measurements of cosmic-ray proton and lepton fluxes in the local ISM from the Voyager I satellite (Cummings et al. 2016) and inside the heliosphere from AMS-02 orbiting Earth on the International Space Station (Aguilar et al. 2014, 2015, 2019). We first find the proton spectrum at the source; this then fixes the contribution to the lepton flux at Earth coming from proton interactions with cosmic rays and the ISM ($p_{CR} + p_{ISM}$), accounting for a small adjustment due to contributions from nuclei. We then attribute the remaining lepton flux to the injected lepton spectrum. Thus, in this simplified ansatz, the well-known "positron anomaly" (Adriani et al. 2009), i.e., the excess of positron flux beyond expectations from secondary production at energies $\gtrsim$10 GeV, is attributed to the injected lepton spectrum. Such an ansatz is plausible if the astrophysical sources of primary positrons have a similar spatial distribution as the sources of primary electrons, e.g., if pulsars are the sources of the "anomalous" positrons and electrons (Hooper et al. 2009) and the bulk of the electrons are accelerated in supernova remnants. Then, if the interest is only in the sum of electrons and positrons, as it is in our case, the two sources can be lumped together into a single source class. Due to the fast cooling time of electrons and positrons at high energies, the high-energy flux at Earth might be dominated by a local source and thus not representative of the average lepton flux in the Galaxy (e.g., Di Mauro et al. 2014; Joshi & Razzaque 2017; Mertsch 2018). However, these effects are expected to play a role only above 100 GeV and are thus not important for the synchrotron frequencies of interest in this study. An example of our fit of the cosmic-ray lepton flux is shown in the left panel of Figure 6.

As a further systematic check, we also interpret the synchrotron data using the `z10LMPDE` cosmic-ray electron model, a GALPROP calculation of Orlando & Strong (2013, hereafter OS13) used in Adam et al. (2016) for GMF modeling (T. R. Jaffe 2017, private communication). This model assumes a half-cylinder height of $h_D = 10$ kpc, a maximum radius of $R_{max} = 20$ kpc, and the source distribution from Strong & Moskalenko (1998) with a radial cutoff at 15 kpc. Further differences to our fiducial GALPROP calculation include a different magnetic field (Sun & Reich 2010) for electron cooling and a different value of $D/h_D = 0.031$ at 10 GV. We normalized this model to match the flux of electrons and positrons at 35 GV measured by the Alpha Magnetic Spectrometer.

The vertical and radial distribution of the cosmic-ray lepton density at 10 GV for different values of h_D and the OS13 model are shown in the middle and right panels of Figure 6. As expected, a larger half-height of the diffusion volume leads to a larger cosmic-ray occupation in the halo, while the density in the disk is approximately constant due to the normalization at Earth. The different source distribution assumed for the OS13 results is mainly responsible for the very different radial distribution of cosmic-ray leptons.

Of course, further variations beyond the scale height are possible, and we studied the effect on synchrotron maps of several other type of variations, as described below. However, only the variation of h_D makes a significant change in the PI predictions outside of the mask we use, so we only include the six n_{cre} models outlined above in our GMF model fitting.[11] A spiral distribution of sources can affect the PI up to 25% in the Galactic plane but has negligible effects outside of the polarization mask used in this work. Using the Planck tune of the JF12 random field (Adam et al. 2016) for synchrotron

[11] Note that in the framework of a tunable striation parameter, an overall factor in the PI does not affect the derived coherent magnetic field, but only the striation factor.

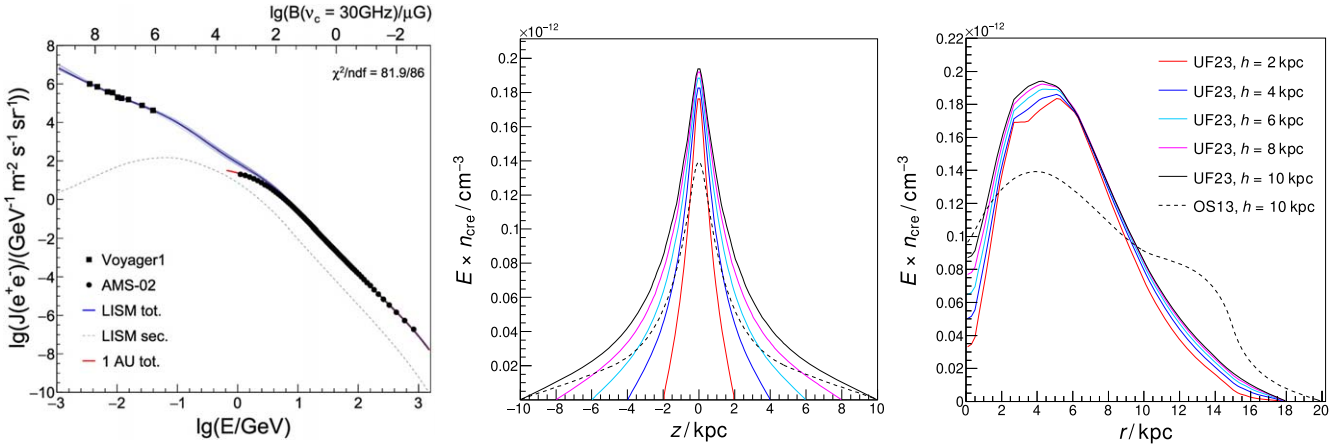

Figure 6. Left: flux of cosmic-ray electrons and positrons at Earth. Black points show the measurements. The calculated flux in the local ISM (LISM) for the $h_D = 6$ kpc case is shown as a blue band, and the contribution from secondary production ($p_{CR} + p_{ISM}$ interactions) is indicated by a dashed line; the solar-modulated flux at Earth is shown as a red line. The additional x-axis at the top of the figure shows the magnetic field strength needed to obtain a synchrotron peak at $\nu_c = 30$ GHz (i.e., the frequency for which the Planck collaboration reports the polarized synchrotron emission used here) for the electron energy given in the x-axis at the bottom of the figure. Middle: density of 10 GV cosmic-ray electrons at a Galactocentric radius $r = 4$ kpc as a function of Galactic height z and (right) as a function of radius r at the midplane ($z = 0$). Different choices of the half-height h_D of the diffusion volume are shown as lines with different colors. The dashed line is the result of Orlando & Strong (2013) for $h_D = 10$ kpc.

cooling instead of the original model (Jansson & Farrar 2012b) affects the intensity by up to 16% in the outer Galaxy (where a spiral arm with a large random field is present in the original model to describe the intensity from the "fan region"), but the differences are again negligible outside the masked region used in this paper. The same holds for n_{cre} models using a three-dimensional model of the interstellar radiation field from Porter et al. (2017). Moreover, in this study, we did not iteratively readjust the magnetic field used for the synchrotron energy losses in the n_{cre} calculations. But the resulting refitted coherent fields are of the same order of magnitude as the ones of JF12; therefore, the electron cooling is dominated by the sum of the contributions from the random magnetic field and inverse Compton scattering. Finally, it was shown by Orlando (2018) that the cosmic-ray electron spectrum above a few GeV is insensitive to the inclusion of reacceleration and/or convection in the diffusion equation; therefore, we do not consider it here.

The six models shown in Figure 6 will be used in this paper to study the systematic effect of the three-dimensional model of n_{cre} on the derived structure of the GMF.

We note that future systematic studies should include an investigation of the effects of a more realistic particle propagation with an inhomogeneous and/or anisotropic diffusion coefficient (e.g., Di Bernardo et al. 2013; Merten et al. 2017; Giacinti et al. 2018; AL-Zetoun & Achterberg 2018), ideally with a self-consistent description of the relation between the magnetic field and the diffusion coefficient (e.g., Kuhlen et al. 2022; Blasi 2023).

5. Magnetic Field Models

5.1. General Considerations

The goal of this work is provide the best possible analytic approximation to the large-scale coherent GMF, given the limitations of the present data and other required input. To this end, we describe the field as a superposition of functions that are general enough to capture the main large-scale features of its structure.

Inspired by previous models of the coherent GMF (e.g., Stanev 1997; Prouza & Šmída 2003; Sun et al. 2008; Pshirkov et al. 2011; Jansson & Farrar 2012a), we describe the global structure of the GMF as a superposition of a large-scale halo field and a logarithmic spiral field in the Galactic disk beyond a minimum radius. The halo field is composed of a toroidal and a poloidal field as introduced by Jansson & Farrar (2012a). The need for each of these components to describe large-scale features of the RM and PI sky is discussed in Section 7. In this section, we give a brief overview of the different parametric descriptions investigated in this paper and note ways in which the actual coherent GMF is simpler than the most general case.

5.2. Disk Field

5.2.1. General Features

The observations discussed above of synchrotron polarization patterns in face-on external spiral galaxies, as well as the RMs of Galactic pulsars, suggest that the coherent field of the Milky Way follows a spiral pattern close to the disk, outside a few kpc from the Galactic center. A logarithmic spiral is inherently divergence-free, making it an attractive functional form.

In several previous GMF models, the magnetic field was assumed to be organized in "arms" with a predefined geometry with the pitch angle α fixed to a value motivated by that of the spiral matter density of the Milky Way (see, e.g., Brown et al. 2007; Jaffe et al. 2010; Jansson & Farrar 2012a; Han et al. 2018). The magnitude and sign within each arm were adjusted to match the data, with the total radial flux being constrained to be zero. Within a given arm, the field was approximated to be azimuthally constant, leading to strong discontinuities at the boundaries of the arms.

For a fixed-thickness disk with logarithmic spiral arms, flux conservation implies the field $\sim r^{-1}$, leading to an unphysical singularity at the origin. Therefore, the field in such models was assumed to vanish or transition to a purely toroidal configuration at some inner radius.

It should be noted that although the total radial flux vanishes for both the outer logarithmic spiral and inner toroidal regions, the radial flux does not vanish locally in the spiral arm region, whereas it does vanish locally in the inner region. Therefore,

the flux lines must be microscopically reorganized in some transition region at the boundary. This structure is physically plausible due to the mechanical action of the Galactic bar, which extends several kpc from the Galactic center and rotates significantly faster than the disk. The turbulence in the plasma due to the stirring of the bar entangles field lines that, at a larger radius, are ordered. In the inner, stirred region, these field lines either contribute to $B_{\rm rand}$ or reconnect, converting magnetic energy to thermal energy.

Global radial flux conservation is compatible with a nonzero toroidal coherent field in the inner zone, but in the picture above, the toroidal field strength would be small apart from fluctuations amplified by dynamo action. We allowed for a possible toroidal disk field in the inner Galaxy and found it to be consistent with zero (consistent with previous fits by Jansson & Farrar 2012a), so we dropped it from the modeling. In the next subsections, we describe our two basic models for the disk field and the variants we also investigated.

5.2.2. Fourier Spiral

Here we introduce a new description of the spiral arms of the disk field that provides flexibility to fit the geometry of the magnetic arms and also avoids discontinuities between them. To specify the spiral disk field, we need fix the pitch angle α, the width and angle of each arm at some reference radius, and the strength of each arm. For this purpose, we decompose the magnetic field strength at a reference radius $r_0 = 5$ kpc, as a function of angle ϕ_0, into n modes of strength B_m and phase ϕ_m:

$$B(r_0, \phi_0) = \sum_{m=1}^{n} B_m \cos\left(m(\phi_0 - \phi_m)\right). \tag{10}$$

The magnetic field in cylindrical coordinates at position (r, ϕ, z) is given by

$$\boldsymbol{B}_{\rm d} = (\sin\alpha, \cos\alpha, 0)\, \frac{r_0}{r}\, B(r_0, \phi_0) h_{\rm d}(z)\, g_{\rm d}(r), \tag{11}$$

where the ϕ_0 corresponding to the given (r, ϕ) is found by following the field line along the logarithmic spiral from (r, ϕ) to the reference radius r_0, the relation being

$$\phi_0 = \phi - \ln(r/r_0)/\tan\alpha. \tag{12}$$

Due to the expansion of $B(r_0, \phi_0)$ being in terms of a cosine series, we refer to this model of the disk field as "Fourier spiral" in the following. The solenoidality of this field model for $g_{\rm d}(r) = 1$ is assured because for each mode in Equation (10), the same amount of flux enters and exits along the circle at r_0, and, due to the $\frac{r_0}{r}$ factor in Equation (11), the magnetic flux in each arm is constant as a function of radius.[12] Independently of $g_{\rm d}(r)$, the total radial flux in this disk field model vanishes for every radius.

The functions $h_{\rm d}(z)$ and $g_{\rm d}(r)$ describe the fade-in and fade-out of the field in the vertical and radial direction, respectively. We choose the ansatz

$$h_{\rm d}(z) = 1 - \sigma\left(\frac{|z| - z_{\rm d}}{w_{\rm d}}\right), \tag{13}$$

and

$$g_{\rm d}(r) = \left[1 - \sigma\left(\frac{r - r_2}{w_2}\right)\right] \sigma\left(\frac{r - r_1}{w_1}\right)(1 - e^{-r^2}), \tag{14}$$

where $\sigma(x)$ denotes the logistic sigmoid function,

$$\sigma(x) = \frac{1}{1 + e^{-x}}, \tag{15}$$

such that the disk field is suppressed to half of its value at $z_{\rm d}$, r_1, and r_2, and the suppression rate is given by the corresponding transition widths. The additional factor $(1 - e^{-r^2})$ is needed to assure that the factor $g_{\rm d}(r)/r$ in Equation (11) goes to 0 at $r = 0$.

Note that mathematically, $g_{\rm d}(r)$ violates the solenoidality of the field and is thus to be understood as an effective modeling of the behavior of the disk field at small and large radii. At large radii, we expect that the coherent magnetic flux gradually spreads out as the plasma confining it to the disk merges into the circumgalactic medium. At some point, the field is so weak and the electron densities so low that our observables are not sensitive to it. We represent this by an effective outer distance r_2. In the inner Galaxy, within a radius designated r_1, we expect that the coherent log spiral structure is replaced by a region of low coherent field or possibly a weak toroidal field, as discussed in the previous subsection.[13]

For consistency with the outer radius of the molecular ring in the YMW16 model, in this analysis, we set r_1 to 5 kpc; we fixed r_2 to 20 kpc having checked that the fit is insensitive to the exact choice. For the transition widths, we adopt $w_1 = w_2 = 0.5$ kpc. Whether the details of the inner transition can be constrained by the data is left for future work. Without loss of generality, we set the reference radius to $r_0 = 5$ kpc, such that the coefficients B_m in Equation (10) denote the amplitude of the modes in the inner Galaxy.

An example of a Fourier spiral disk field is shown in the right panel of Figure 7, and for comparison, a fixed-arm spiral field is displayed in the left panel. Apart from obvious differences in the arm topologies and field strengths, which are mostly due to the different data sets used to fit these models, it can be seen that the Fourier spiral results in a smooth disk field without the discontinuities inherent in the previous fixed-arm models.

5.2.3. Spiral Spur

As an alternative model to the grand-design magnetic spiral implied by the Fourier spiral, we investigate if a localized spiral segment can describe the data equally well. Such an isolated magnetic "spiral spur" in the disk is seen, e.g., in Figure 2 of the cosmological simulation of Pakmor et al. (2014), due predominantly to a local compression of field lines.

[12] Inclusion of an axisymmetric component of the $m = 0$ component implies a net inward or outward flux of the disk field. This excess flux would necessarily flow into the halo and imply a net vertical flux, but we do not find evidence of that in the data; see Section 7.6. Moreover, including the component does not improve the fit significantly ($\Delta\chi^2 = -2.9$).

[13] Further possibilities include that the magnetic flux of the disk field exits vertically in the inner Galaxy (Ferrière & Terral 2014; but see footnote 12) or that the inward- and outward-going field lines of the disk field connect at r_1 and r_2 as investigated by Kleimann et al. (2019). Both of these configurations entail regions of very high coherent field, which would be energetically disfavored, so we did not pursue them.

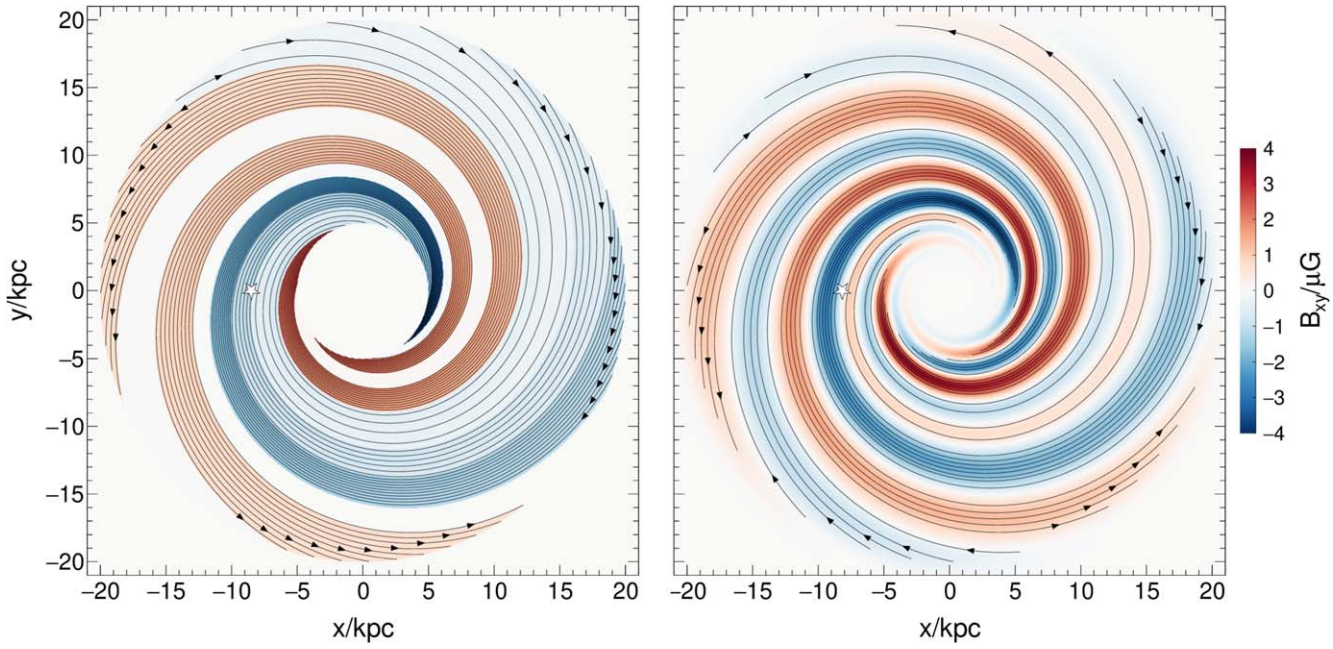

Figure 7. Left: fixed-arm spiral disk field of the JF12 model. Right: Fourier spiral of the "neCL" model; see Section 7. The position of the Sun is indicated with a star.

We model a spur as a Gaussian of width w_S at a reference radius r_0,

$$B(r_0, \phi_0) = B_1 \exp\left(-\frac{1}{2}((\phi_0 - \phi_1)/w_S)^2\right), \tag{16}$$

where ϕ_1 denotes the center of the spur and the angle ϕ_0 follows again from the logarithmic spiral via Equation (12). The field of the spur in cylindrical coordinates is, similar to Equation (11), given by

$$\boldsymbol{B}_S = (\sin\alpha, \cos\alpha, 0)\,\frac{r_0}{r}\,B(r_0, \phi_0) h_d(z)\, g_S(\phi), \tag{17}$$

where instead of using the radial attenuation $g_d(r)$, the size of the spur is determined from its angular center ϕ_C and angular half-length L_c. We attenuate the magnetic field at $\phi = \phi_c \pm L_c$ with

$$g_S(\phi) = 1 - \sigma\left(\frac{\Delta(\phi, \phi_c) - L_c}{w_c}\right). \tag{18}$$

In the following, we use a fixed attenuation width of $w_c = 5°$ and, without loss of generality, $r_0 = 8.2$ kpc, such that the parameter $B_{0,S}$ is close to the magnetic field strength at the center of the spur if it is located in the proximity of the solar radius, which is the main focus of the spiral spur model. The superficial lack of flux conservation is understood as a transition between a locally compressed and a more complex, broadly distributed flux distribution not captured in the global model function.

5.2.4. Further Considerations Regarding the Disk Field

Further variations to the Fourier spiral and spiral spur models were studied but not included in the fiducial models presented in this paper. We investigated a circular "ring field" at small Galactocentric radii. Such a field was introduced in JF12 at $3\,\mathrm{kpc} < r < 5\,\mathrm{kpc}$ with an estimated field strength of $0.1 \pm 0.1\,\mu$G. Here we confirmed that a ring field does not significantly improve our fits; therefore, we did not include it in our fiducial models.

We also investigated the sensitivity of the data to the particular choice of $h_d(z)$ and found no significant changes when replacing the logistic sigmoid with a Gaussian ($\Delta\chi^2 = -3$) and a slightly worse description when using an exponential ($\Delta\chi^2 = +30$).

Furthermore, we studied a flaring disk field, i.e., an increase of the vertical extent of the disk with Galactocentric radius as, e.g., observed for the atomic hydrogen of the disk (Kalberla & Kerp 2009). We also added the Galactic warp as determined by Levine et al. (2006) to the disk field model. Neither of the two variations improved our preliminary fits reported in Unger & Farrar (2019), and we therefore do not include them in this analysis.

A model variant we did not explore here is to allow a net inward or outward flux in the disk that is balanced by flux entering the disk due to an imbalance in the north–south halo fields; this was checked by D. Khurana (2016, private communication) for the JF12 model, and the flux transfer was found to be consistent with zero, compatible with our findings on the symmetry of the halo field as reported in Section 7.6 below.

5.3. Halo Field

Our knowledge of the global structure of the magnetic halo of Milky Way–like galaxies relies on a combination of edge-on observations of external galaxies and high-latitude RMs and radio emission (for a review, see, e.g., Haverkorn & Heesen 2012).

The large-scale antisymmetric features of extragalactic RMs, see Equation (9) and Figure 2, follow naturally from a large-scale toroidal[14] field of opposite sign above and below the plane, leading to the observed pattern in RM when

[14] Here we use the term toroidal field synonymously with a purely azimuthal field, $\boldsymbol{B} = (0, B_\varphi, 0)$, while the term poloidal field denotes a vector field with a vertical but not an azimuthal φ-component, $\boldsymbol{B} = (B_r, 0, B_z)$.

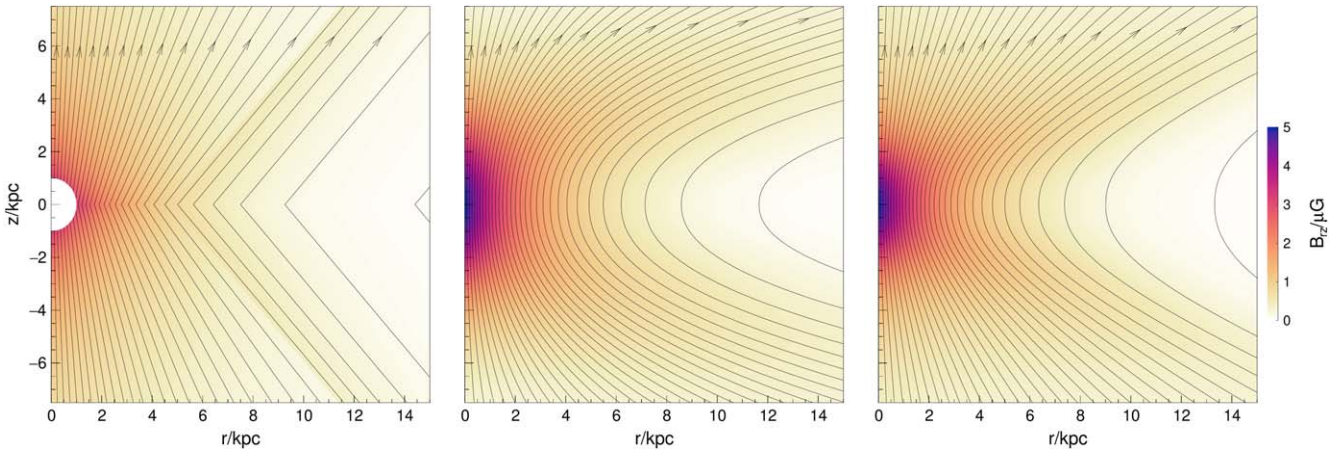

Figure 8. X-field models: JF12 (left), power-function (middle), and coasting X-field (right).

superimposed with the local spiral arm of the disk field, schematically

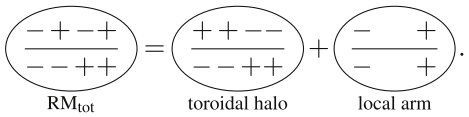

(19)

In addition, the large-scale patterns of the Q and U parameters, in particular the tilted nature of the corresponding polarization vectors, can be explained by the presence of an additional poloidal halo component, as suggested by Jansson & Farrar (2012a), who introduced a coherent "X-field" halo component inspired by the X-shaped radio polarization halos observed in edge-on spiral galaxies (e.g., Krause et al. 2020).

Here we will model the magnetic halo of the Galaxy either by the superposition of a separate toroidal and poloidal field or by a unified halo model, as described below.

5.3.1. Toroidal Halo

For the toroidal field, we adopt the logistic-exponential ansatz ("σ_r exp$_z$") of JF12. It is a purely azimuthal field,

$$\boldsymbol{B}_{\rm t} = (0, B_\phi, 0), \tag{20}$$

in cylindrical coordinates, with

$$B_\phi = (1 - h_{\rm d}(z))\, e^{-\frac{|z|}{z_{\rm t}}} \times\left(1 - \sigma\left(\frac{r - r_{\rm t}}{w_{\rm t}}\right)\right)\begin{cases} B_{\rm N} & z > 0 \\ B_{\rm S} & \text{otherwise} \end{cases}, \tag{21}$$

where $z_{\rm t}$ is the exponential scale height of the toroidal field and the radial cutoff of the toroidal halo is modeled by a logistic sigmoid function with a transition at $r_{\rm t}$ and a width $w_{\rm t}$. The maximum field strength above and below the Galactic plane is given by $B_{\rm N}$ and $B_{\rm S}$, respectively. $h_{\rm d}$ is defined in Equation (13); i.e., the toroidal halo field is phased in by the complement of the function that phases out the disk field.

Whereas in JF12, the radial extent of the northern and southern halos was allowed to be different, we use only one value $r_{\rm t}$, since our preliminary fits showed only a minor deterioration of the fit quality when enforcing a symmetric toroidal (Unger & Farrar 2018). We also checked whether the data are fit better with independent functions $h_{\rm d}(z)$ for the disk and the halo separately but found similar transition heights for the disk and halo, even if they were allowed to take on different values.

5.3.2. Poloidal Halo

Jansson & Farrar (2012a) introduced a coherent "X-field" model that is purely vertical at $r = 0$ and becomes increasingly tilted with increasing radius until reaching a constant asymptotic angle with respect to the Galactic plane, $\theta_X \sim 50°$, at a radius of $r_X \sim 5$ kpc. With this model, a good description of the polarized synchrotron data could be achieved. However, this X-field parameterization has three types of discontinuities: one in the inner Galaxy, one at the Galactic plane at $z = 0$, and one at $r = r_{\rm X}$, as can be seen in the left panel of Figure 8. These discontinuities are avoided by the improved X-field models described in the following.

(A) Power-function X-field—Ferrière & Terral (2014) employed a useful method to construct poloidal field models using Euler potentials. Given the equation of field lines in the form of $r = f(a, z)$ starting midplane at a radius a (i.e., $f^{-1}(r = a) = 0$), the divergence-free cylindrical components of the poloidal field ($B_\phi = 0$) are given by

$$B_r = -\frac{a}{r}\, B_0(a) \frac{\partial a}{\partial z} \tag{22}$$

and

$$B_z = \frac{a}{r}\, B_0(a)\, \frac{\partial a}{\partial r}, \tag{23}$$

where any function $B_0(a)$ of the radial dependence of the z-component of the field at $z = 0$ will preserve the solenoidality of the field.

We extend their parabolic "model C" for the z-evolution of the field lines to arbitrary powers p,

$$r = a\, (1 + |z/z_{\rm p}|^p), \tag{24}$$

corresponding to a midplane radius of

$$a(r, z) = \frac{r}{1 + |z/z_{\rm p}|^p}. \tag{25}$$

Using Equations (22) and (23), the radial and vertical field components are

$$B_r = p\,\frac{z\,a^3}{r^2\,z_{\rm p}^2}\,|z/z_{\rm p}|^{p-2}\,B_0(a) \tag{26}$$

and

$$B_z = \frac{a^2}{r^2}\,B_0(a) \tag{27}$$

for $p \geqslant 1$. In Section 7, we will study several possibilities for the radial midplane dependence of the field strength,

$$B_0(a) = B_{\rm p}\,f_{\rm X}(a), \tag{28}$$

with normalization constant $B_{\rm p}$ and one of the following radial functions:

$$\bullet\ \exp{:}\ f_{\rm X}(a) = e^{-\frac{a}{r_{\rm p}}}, \tag{29}$$

$$\bullet\ \text{gauss}{:}\ f_{\rm X}(a) = e^{-\frac{1}{2}\left(\frac{a}{r_{\rm p}}\right)^2}, \tag{30}$$

$$\bullet\ \text{sech2}{:}\ f_{\rm X}(a) = \text{sech}^2(a/r_{\rm p}), \tag{31}$$

$$\bullet\ \text{logistic}{:}\ f_{\rm X}(a) = 1 - \sigma((a - r_{\rm p})/w_{\rm p}), \tag{32}$$

where sech denotes the hyperbolic secant, $\text{sech}(x) = 1/\cosh(x) = 2/(e^x + e^{-x})$, and σ is the logistic sigmoid function defined in Equation (15).

An example of a power-function X-field is shown in the middle panel of Figure 8 (for $p = 2.2$ and an exponential radial dependence with $r_{\rm p} = 2.8$ kpc). As can be seen, the discontinuities present in the original JF12 X-field are avoided, but it differs qualitatively from the JF12 X-field in that the field lines become more and more parallel to the Galactic plane as the radius increases rather than reaching an asymptotic angle.

(B) Coasting X-field— A "coasting X-field" with parallel field lines beyond a certain reference radius $a_{\rm c}$ can be achieved by choosing the field line equation

$$r = \left(a^n + c\,\frac{a^n}{a^n + a_{\rm c}^n}\,|z|^p\right)^{\frac{1}{n}}. \tag{33}$$

The positive solution for a^n is[15]

$$a^n = \frac{1}{2}(\sqrt{\Delta^2 + 4a_{\rm c}^n r^n} - \Delta), \tag{34}$$

where $\Delta = a_{\rm c}^n + c|z|^p - r^n$. Inserting it into Equations (22) and (23), the radial and vertical field components are obtained as

$$B_r = B_0(a)\,\frac{c\,a^2\,p\,z\,|z|^{p-2}}{n\,r\,\sqrt{\Delta^2 + 4a_{\rm c}^n r^n}} \tag{35}$$

and

$$B_z = B_0(a)\left(\frac{r}{a}\right)^{n-2}\frac{a^n + a_{\rm c}^n}{\sqrt{\Delta^2 + 4a_{\rm c}^n r^n}}. \tag{36}$$

[15] Note that $\sqrt{x^2 + k} - x$ is of low numerical accuracy if $k \ll x$. Instead, we use $(\sqrt{x^2 + k} - x)\frac{\sqrt{x^2 + k} + x}{\sqrt{x^2 + k} + x} = \frac{k}{\sqrt{x^2 + k} + x}$ in our numerical implementation.

In this paper, we study X-fields for the special case $p = n$, for which Equation (33) becomes

$$r = a\left[1 + \frac{1}{1 + (a/a_{\rm c})^p}\left(\frac{|z|}{z_{\rm p}}\right)^p\right]^{\frac{1}{p}}, \tag{37}$$

and Equations (35) and (36) simplify accordingly. The new parameter $z_{\rm p}$ is given by $z_{\rm p} = \frac{a_{\rm c}}{c^{1/p}}$. For large values of the coasting radius $a_{\rm c}$ ($a \ll a_{\rm c}$), this three-parameter function simplifies further to the two-parameter equation

$$r = a\left[1 + \left(\frac{|z|}{z_{\rm p}}\right)^p\right]^{\frac{1}{p}}. \tag{38}$$

An example of a coasting X-field with $p = n = 2.2$ and $a_{\rm c} = 7$ kpc is shown in the right panel of Figure 8.

5.3.3. Unified Halo Model

A toroidal halo field with different directions in the northern and southern hemispheres can be the result of differential rotation of a poloidal halo field (e.g., Andreasyan & Makarov 1988; Men & Han 2003). Farrar (2014) pointed out that—given the sign of the dipolar field discovered by Jansson & Farrar (2012a)—the differential rotation of the Galaxy would create toroidal halo fields with the observed directions in the northern and southern hemispheres. However, the question of whether differential rotation can explain the observed toroidal field strength quantitatively, including its vertical and radial profiles, was not addressed. Here, we show that the toroidal field is in fact remarkably well described by the simplest possible model based on the observed differential rotation. The success of this initial simple treatment gives encouragement that a more fully developed treatment of the effects that limit the buildup of the toroidal field can eventually enable a physics-based model of the halo field to replace the ad hoc fitting approach that has been required up to now.

Consider a poloidal field that is dragged along with the rotation of the Galaxy and evolves via the induction equation,

$$\partial_t \boldsymbol{B} = \boldsymbol{\nabla} \times (\boldsymbol{v} \times \boldsymbol{B}) - \underbrace{\boldsymbol{\nabla} \times \eta(\boldsymbol{\nabla} \times \boldsymbol{B})}_{\to 0 \text{ for } \sigma \to \infty}, \tag{39}$$

where the "frozen-in condition" applies for perfect conductivity, $\sigma \to \infty$, for which the magnetic diffusivity vanishes, $\eta \propto 1/\sigma \to 0$ (e.g., Parker 1979). Under these conditions and for a purely azimuthal rotation velocity v, the induction equation simplifies to

$$\partial_t \boldsymbol{B} = \boldsymbol{\nabla} \times (\boldsymbol{v} \times \boldsymbol{B}) = \begin{pmatrix} -\frac{v}{r}\,\partial_\phi B_r \\ \partial_z(vB_z) + \partial_r(vB_r) \\ -\frac{v}{r}\,\partial_\phi B_z \end{pmatrix}. \tag{40}$$

Thus, for a magnetic field that is poloidal and azimuthally symmetric at $t = 0$ ($\partial_\phi B_r = \partial_\phi B_z = 0$), the poloidal components are constant, and only B_ϕ evolves with time,

$$B_\phi(t) = (B_z\,\partial_z v + rB_r\,\partial_r \omega)t, \tag{41}$$

where we introduced the angular velocity $\omega = \frac{v}{r}$ and used the solenoidality of the poloidal field.

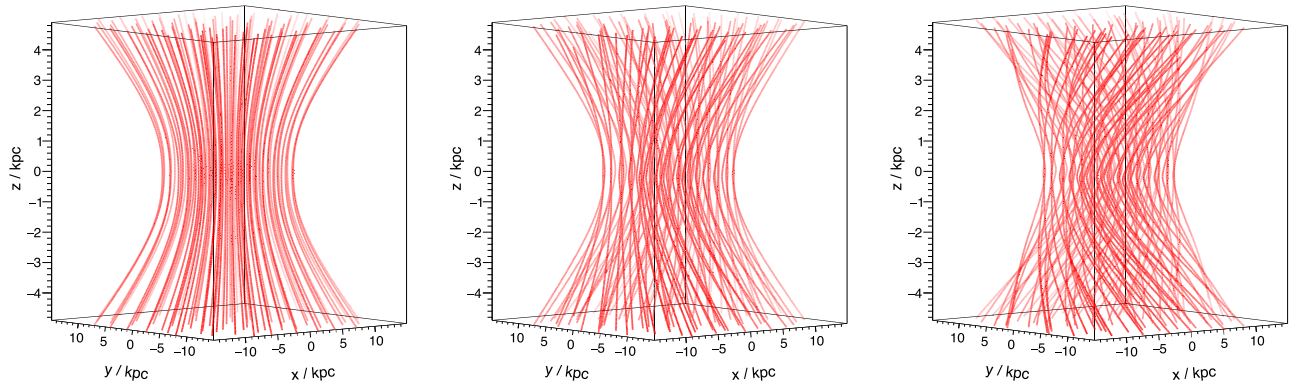

a: $t = 0$ Myr b: $t = 25$ Myr c: $t = 50$ Myr

Figure 9. Illustration of the unified halo model at different times $t = 0$, 25, and 50 Myr.

Equation (41) can be applied to evolve any type of poloidal field analytically, and it describes the linear increase of B_ϕ due to the differential motion of the plasma the magnetic field is embedded in. The large-scale motion of the plasma in the Galaxy follows the Galactic rotation curve, which we take to approximately factorize as

$$v(r, z) = v_0 f(r) g(z). \tag{42}$$

Using

$$f(r) = 1 - e^{-r/r_v} \equiv f_r, \tag{43}$$

we adjust v_0 and r_v to match the velocities of high-mass star-forming regions with parallax measurements from Reid et al. (2014), leading to $v_0 = -240\,\mathrm{km\,s^{-1}}$ (negative because the Galaxy rotates clockwise) and $r_v = 1.6$ kpc. For the vertical velocity gradient, we use

$$g(z) = 2/(1 + e^{2\,|z|/z_v}) \equiv g_z, \tag{44}$$

with $z_v = 10$ kpc, to reproduce $\partial_z v = (-22 \pm 6)\,(\mathrm{km\,s^{-1}})\,\mathrm{kpc^{-1}}$ as measured within 100 pc of the Galactic midplane by Levine et al. (2008).[16]

With this particular choice of f_r and g_z, the evolution of the azimuthal field via Equation (41) is

$$B_\phi(t) = (B_z\,\Delta_z + B_r\,\Delta_r)t, \tag{45}$$

with the two shear terms

$$\Delta_z = \partial_z v = -\mathrm{sgn}(z)\frac{v_0}{z_v} f_r\, g_z^2\, e^{2\,|z|/z_v} \tag{46}$$

and

$$\Delta_r = r\,\partial_r \omega = v_0\left(\frac{1 - f_r}{r_v} - \frac{f_r}{r}\right) g_z\,. \tag{47}$$

An example of a unified halo field is shown in Figure 9 starting at $t = 0$ with a poloidal coasting X-field with $B_\mathrm{p} > 0$ and a logistic sigmoid cutoff at $r = 8$ kpc. Due to the radial and vertical shear of the rotation curve, Equation (42), an azimuthal field is created at $t > 0$ that has a different sign in the northern and southern hemispheres to which both terms in Equation (41) contribute constructively. Obviously, this process cannot continue in this naive form over the lifetime of the Galaxy or it would overproduce the observed azimuthal field strength. A steady-state azimuthal field could be obtained by including a suitable dissipative term in the induction equation and possibly a source term from the α-effect of dynamo theory (e.g., Brandenburg & Ntormousi 2023), but for the purpose of this paper, we interpret the best-fit twisting time as an effective parameter of this simplest version of a unified halo model.

In summary, in this section, we introduced two variants of the disk field (grand spiral or spiral spur), two variants of the poloidal field (power-function or coasting), and two variants for the toroidal halo (explicit or from twisting). These magnetic field submodels as well as their parameters are listed in Table 1, together with a few other model parameters.

6. Model Optimization

The parameters $\boldsymbol{p}$ of a GMF model are optimized by minimizing the sum of the variance-weighted squared difference between the modeled m and measured d observables,

$$\chi^2 = \sum_{i=\mathrm{RM},Q,U} \sum_{j=1}^{N_i} \frac{(d_{ij} - m_{ij}(\boldsymbol{p}))^2}{\sigma_{ij}^2}, \tag{48}$$

where the second sum runs over the N_j lines of sight available for the RM and synchrotron data. Each line-of-sight datum d_{ij} is obtained by averaging available measurements over a finite solid angle around the line-of-sight direction. These angular *pixels* are defined by the HEALPIX resolution of the data. The predicted values m_{ij} of a GMF model, $\boldsymbol{B}(\boldsymbol{x};\boldsymbol{p})$, are given by the numerical evaluation of the line-of-sight integrals for RM, Q and U. Even for a perfect GMF model, the differences $d_{ij} - m_{ij}$ are expected to be distributed with a variance of σ_{ij}^2, since the data are subject to experimental uncertainties and the model prediction does not include "Galactic variance" originating from random magnetic fields and from fluctuations of the densities of thermal electrons and cosmic-ray electrons. In general, Galactic variance will introduce correlations between adjacent pixels if the size of the perturbations is larger than the angular size of 1 pixel. In that case, the full covariance matrix

[16] The toroidal field in the unified model is relatively insensitive to the uncertainty in $g(z)$, since the radial and vertical gradients contribute with the same sign to the twisting, contrary to the result reported in Men & Han (2003). Terral & Ferrière (2017) explored a twisted halo model introducing a generic "winding function" $g_\phi(r, z)$ of the field lines. Their Equation (27) is equivalent to Equation (41) for the choice $g_\phi = t\,v(r, z)/r$. However, they did not investigate this explicit connection of the winding function to the velocity field $v(r, z)$ of the Galaxy but used an ad hoc parametric winding function.

Table 1
List of Parameter Names of Different Model Components

Name	Explanation	Unit	Value
Disk Field			
Common Parameters			
α	Pitch angle	deg	Free
$z_{\rm d}$	Transition height	kpc	Free
$w_{\rm d}$	Vertical transition width	kpc	Free
(a) Grand-design spiral, Equations (10) and (11)			
B_m	Magnetic field strength of mode m	μG	Free
ϕ_m	Phase of mode m	deg	Free
r_0	Reference radius	kpc	5
r_1	Inner radius	kpc	5
w_1	Inner radial transition width	kpc	0.5
r_2	Outer radius	kpc	20
w_2	Outer radial transition width	kpc	0.5
(b) Spiral spur, Equation (16)			
B_1	Magnetic field strength at r_0	μG	Free
ϕ_1	Azimuth at r_0	deg	Free
$w_{\rm S}$	Gaussian width	deg	Free
$\phi_{\rm c}$	Central azimuth	deg	Free
$L_{\rm c}$	Half angular length	deg	Free
r_0	Reference radius	kpc	8.2
$w_{\rm c}$	Transition width	deg.	5
Toroidal Halo			
(a) Explicit, Equation (21)			
$B_{\rm N}$	Northern magnetic field strength	μG	Free
$B_{\rm S}$	Southern magnetic field strength	μG	Free
$z_{\rm t}$	Vertical scale height	kpc	Free
$r_{\rm t}$	Transition radius	kpc	Free
$w_{\rm t}$	Radial transition width	kpc	Free
(b) Twisted, Equation (41)			
t	Twisting time	Myr	Free
v_0	Galactic rotation velocity	km s^{-1}	-240
r_v	Scale radius of rotation curve	kpc	1.6
z_v	Scale height of rotation curve	kpc	10
Poloidal Halo			
Common Parameters			
$B_{\rm p}$	Magnetic field strength	μG	Free
p	Field line exponent	⋯	Free
$z_{\rm p}$	Scale height	kpc	Free
$r_{\rm p}$	Radial scale or transition radius	kpc	Free
$w_{\rm p}$	Transition width	kpc	Free
(a) Power-function, Equations (22) and (23)			
(b) Coasting, Equations (35) and (36)			
$a_{\rm c}$	Coasting radius	kpc	Free
Other Model Parameters			
κ	$n_{\rm e}$–B correlation coefficient, Equation (2)	⋯	Free
ξ	Magnetic striation factor, Equation (8)	⋯	Free

needs to be included in the calculation of the χ^2. It is, however, nontrivial to calculate the coefficients of the matrix, because one needs to know the spatial distribution of the turbulence and coherence length for the magnetic field and the thermal and cosmic-ray densities. Different approximations have been applied in previous analyses. Jaffe et al. (2010) and Adam et al. (2016) used a model of the three-dimensional random field strength with a constant coherence length and unperturbed electron densities to calculate the diagonal elements of the covariance matrix. In a more data-driven approach, one can measure the subpixel variance $\hat{\sigma}^2$ of the measurements within 1 pixel and use it as a weight in the fit. Naively, the average over N observations within 1 pixel would then reduce the fluctuations of the mean by a factor of $1/N$, but due to the aforementioned coherent effects, the effective variance will typically be larger. Based on a toy model of coherent cells along the line of sight, Pshirkov et al. (2011) suggested using $\hat{\sigma}^2/\delta^2$ as the pixel variance, with $\delta \approx 3$, but the exact value of δ depends on the integration distance in units of coherence length over which the GMF contributes to the observations (see also Terral & Ferrière 2017). Here we follow the procedure of JF12 and simply use $\hat{\sigma}^2$ itself to weight the data points.

In this paper, the χ^2 as defined in Equation (48) is used to optimize the parameters of a given model and to assess the relative quality of different models. The interpretation of the χ^2 value in terms of goodness of fit is less meaningful. A robust understanding of the statistical fluctuations in the data and their correlations is needed for that purpose. These can only be assessed after the random field and its coherence length have been determined, which will be the subject of near-future work. As an illustration, we apply Equation (48) to simulated data generated with the coherent `base` model derived in this paper and realizations of a turbulent magnetic field generated with the algorithm of Giacalone & Jokipii (1999) for the field strength of the JF12b model from Adam et al. (2016). For this case, the comparison of simulated sky maps d_{ij} to the undisturbed model predictions m_{ij}, together with the "measured" pixelwise standard deviation σ_{ij}, yields reduced χ^2 values of 0.8, 1.5, and 2.4 for a random field with a coherence length of 20, 40, and 80 pc, respectively.

The best set of n model parameters $\boldsymbol{p}$ are found performing a multidimensional optimization of Equation (48) with the MINUIT program (James & Roos 1975) using its MIGRAD method that implements a variable metric gradient descent (Fletcher & Powell 1963; Fletcher 1970). Deterministic gradient methods like MIGRAD descend quickly to a local minimum, which may not always coincide with the global minimum. To find this global optimum, we use the heuristic multistart method; i.e., we perform a number of gradient-descent minimization runs starting at different positions $\boldsymbol{p}_{\rm start}$ distributed uniformly in the n-dimensional hypercube of the parameter space. The run with the smallest local χ^2 is then considered to be the global minimum. For the model fits performed in this paper, we typically run $\mathcal{O}(100)$ minimizations. The fact that many runs from very different starting positions usually converge to the same minimum local χ^2 increases our confidence that the n-dimensional likelihood contour of the optimization problem at hand is well behaved and that we have indeed identified the global minimum of each model variation investigated. The main advantage of this simple multistart method is that such a repeated gradient descent can be trivially parallelized on a computing cluster; thus, it provides an efficient method to search for the global minimum of a model, since each gradient search is very fast.[17]

For each minimization run, a good first approximation of the covariance matrix of the best-fit parameters can be obtained by the parabolic estimates derived from the Hessian matrix of the second derivatives of the χ^2 with respect to the parameters at the minimum. For the final fiducial models presented in

[17] The optimization of the 20-parameter `base` model discussed in Section 7 needs, on average, 4000 χ^2 evaluations to converge. Each evaluation takes 4 s on an Intel® Xeon® E5 processor at 2.4 GHz. For each evaluation, $\boldsymbol{B}$, $n_{\rm e}$, $n_{\rm cre}$, and j_ν are calculated at $\mathcal{O}(10^6)$ positions throughout the Galaxy to calculate the adaptive line-of-sight integrals of RM, Q, and U.

Section 7, more precise confidence intervals of the parameters at the minimum are derived with the profile likelihood method, i.e., by finding for each parameter the two values $p_{\mathrm{up/low}}$ at which $\chi^2(p_{\mathrm{up/low}}) = \chi^2_{\mathrm{min}} + m$, while marginalizing over the other $n-1$ parameters. These estimates are obtained using the MINOS algorithm of MINUIT, and each evaluation of one $p_{\mathrm{up/low}}$ pair is about as computationally expensive as the overall minimization itself. Unless stated otherwise, we quote the 68% ("1σ") intervals obtained for $m=1$. More information on the uncertainties and parameter correlations can be found in Appendix C.

It is worth noting that our approach differs from that of previous GMF studies, which used Markov Chain Monte Carlo (MCMC) to explore the model parameters (e.g., Jansson et al. 2009; Jaffe et al. 2010; Jansson & Farrar 2012a; Terral & Ferrière 2017). MCMC is the preferred method to sample the posterior distribution of a model given the data, but it is not an efficient optimizer (e.g., Hogg & Foreman-Mackey 2018). Moreover, for most applications, the approximate covariance matrix and the confidence intervals derived with the profile likelihood method provide information equivalent to the MCMC samples; see, e.g., Ade et al. (2014) for a comparison of the two methods in the context of cosmological parameter estimation. Most importantly, the ability to efficiently optimize the parameters of many different models is of paramount importance for the GMF inference, since, as will be shown in Section 7, the systematic differences resulting from different model assumptions are typically much larger than the precision estimated for the parameter uncertainties of a particular model.

7. Results

7.1. Base Model

For the results presented in the following, we have optimized the parameters of more than 200 combinations of magnetic field models and auxiliary models to obtain an overview of the range of GMF models attainable in the full set of possible combinations.[18] Many of these model variations are performed with respect to our fiducial "base" model, which consists of a three-mode grand-design spiral disk field, an explicit toroidal halo, and a coasting X-field with a logistic sigmoid radial dependence; there is no correlation between n_e and B, and the striation is a free parameter. The sky maps of RM, Q, and U resulting from this model are calculated with the YMW16 thermal electron model and a cosmic-ray electron density derived for $h_D = 6$ kpc. The model parameters are adjusted to fit the data, yielding an optimum with an acceptable goodness of fit of $\chi^2/\mathrm{ndf} = 7923/6500 = 1.22$, where ndf denotes the number of degrees of freedom, i.e., the number of data points minus the number of free parameters, which is $n_{\mathrm{par}} = 20$ in this case. The contribution from RM pixels to the χ^2 is 4354 ($n_{\mathrm{RM}} = 2838$), and from the Q and U pixels, it is 3569 ($n_Q + n_U = 3682$); i.e., the model describes the polarized synchrotron data slightly better than the RMs.

The contributions of each model component (i.e., disk field and toroidal and poloidal halo) to RM, Q, and U are shown separately in the three top rows of Figure 10, and the predicted sky maps for the sum of all components are displayed in the fourth row. Here it is interesting to see how the interplay of different model components creates the large-scale features observed in the data. As pointed out above, the sum of the disk and toroidal field produces the large-scale structure of RMs; see Equation (19). The PI, on the other hand, is mostly generated by the toroidal and poloidal halo. And, whereas the overall RM can be obtained by summing the RM of each component ($\mathrm{RM} \propto \boldsymbol{B}_\parallel = (\sum \boldsymbol{B}_i)_\parallel = \sum \boldsymbol{B}_{i\parallel}$), the sky pattern of the Stokes parameters of the full model is not the sum of its components since, e.g., $Q, U \propto \boldsymbol{B}_\perp^2 = ((\sum \boldsymbol{B}_i)_\perp)^2 \neq (\sum \boldsymbol{B}_{i\perp})^2$.

The masked model, data, and "pull" are shown in the three bottom rows. The pull is the difference between the data and model in units of standard deviation of the data, and the sum of all squared pulls yields the χ^2, Equation (48). For a perfect match of data and model, the pull should fluctuate randomly around zero with a standard-normal distribution, but here several large regions exist in which the pull has consistently negative or positive values beyond $\pm 1\sigma$. Some of these are close to masked regions, e.g., at the edges of the masks for the north polar spur and loop III for Q and U and close to the mask for the Gum nebula for RM, implying a certain amount of leakage of these features beyond the mask. Others, like the large region of negative pull for RM below the Galactic plane at longitudes of $60° < \ell < 150°$, could indicate deficiencies in the modeling of the global structure of the GMF, e.g., an azimuthal variation of the scale height of the toroidal field. It is, however, plausible that most regions with large-scale deviations can be attributed to local perturbations that appear as structures of large angular scale due to their proximity. Excluding pixels with a large pull from the fit changes the values of the fit parameters, but the differences are of similar magnitude or smaller than the differences between the model variations explored below; see Appendix B for further details.

Apart from these potentially local structures, the base model successfully describes all the large-scale features of the data, in particular the antisymmetric structures of the RM sky and the tilted large-scale "lobes" of negative and positive Q and U. The parameters of the base model can be found in the first column of Table 2. The correlation matrix of the parameters is discussed in Appendix C.

7.2. Thermal and Cosmic-Ray Electrons

To study the dependence of the inferred GMF on the auxiliary models of the thermal and cosmic-ray electron density, we repeat our fits for the model variations discussed in Section 4. The best-fit χ^2 values for different half-heights of the cosmic-ray diffusion volume, h_D, and for the NE2001 and YMW16 models are shown in Figure 11(a). Here the functional forms for the GMF model are identical to the one used for the base model. As can be seen, the fit quality deteriorates rapidly for small values of the height of the diffusion volume, and it reaches a near-constant value at $h_D \gtrsim 4$ kpc. For small values of h_D, the decreasing vertical extent of the cosmic-ray electron halo cannot be compensated for by a larger magnetic halo.[19] Interpolating between the fit results at discrete values of h_D, we estimate a 5σ lower limit on the size of the diffusion volume of

$$h_D \geqslant 2.9 \text{ and } 3.5 \text{ kpc}, \tag{49}$$

[18] The combination of two disk field models, eight poloidal field models, two toroidal field models, two thermal electron models, two synchrotron products, six cosmic-ray electron models, and including an n_e–B correlation or not results in 1536 possible model variations.

[19] For illustration, assume an exponential height dependence of n_{cre} and B with scale heights z_{cre} and z_B. Then, using Equation (3), the height dependence of the synchrotron emissivity is $j_\nu \propto e^{-|z|/z_{\mathrm{syn}}}$ with $z_{\mathrm{syn}} = z_{\mathrm{cre}}/(1 + 2z_{\mathrm{cre}}/z_B)$. It follows that for a given z_{syn} of the data, z_{cre} has to be at least $\geqslant z_{\mathrm{syn}}$ ($z_B \to \infty$).

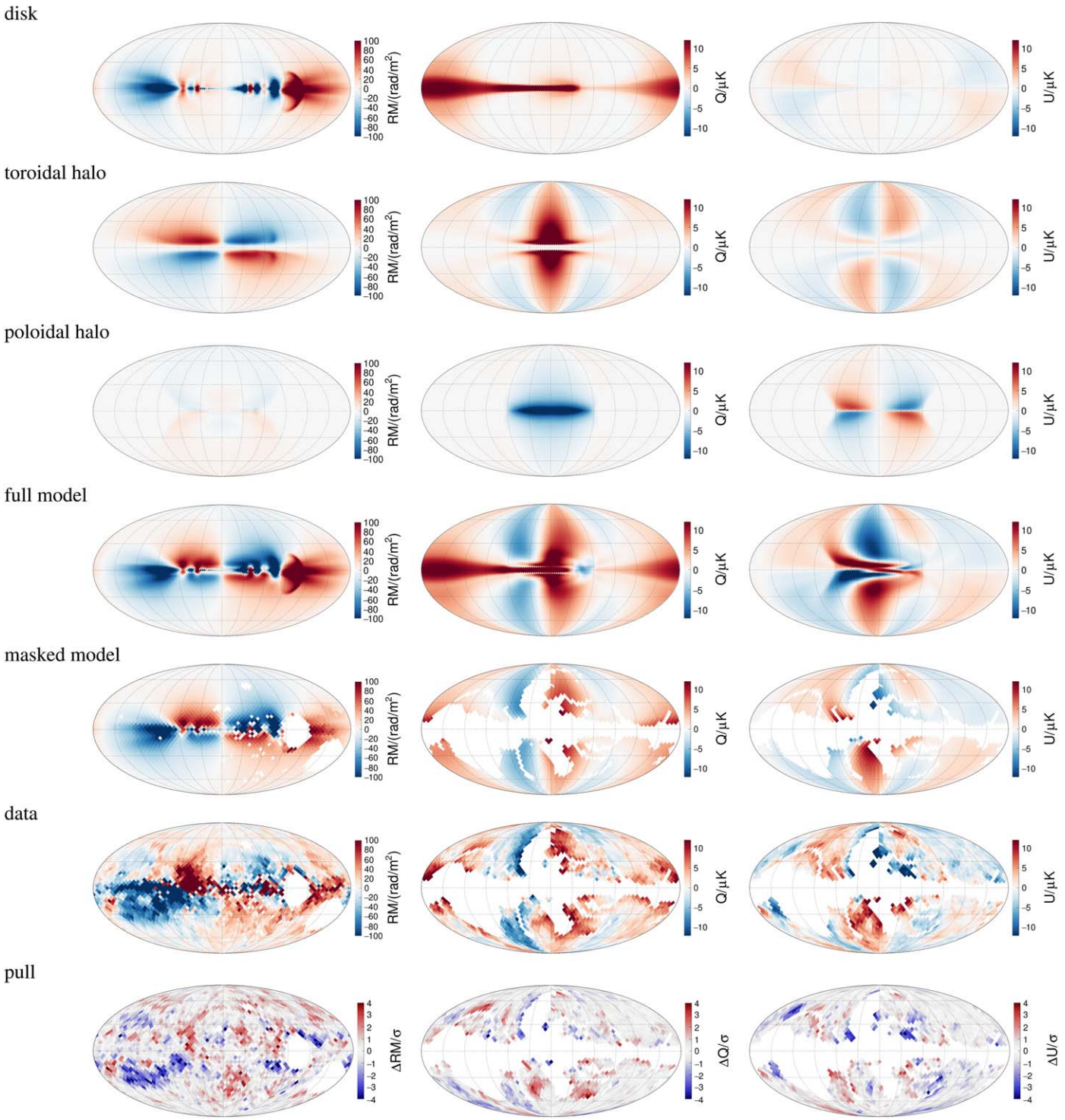

Figure 10. Data and base model prediction for RM, Q, and U. The predictions from the individual model components are shown in the top rows, followed by the full model prediction. The bottom three rows show the masked model, the data, and the pull, i.e., the difference between model and data in units of the standard deviation of the data.

where the two values correspond to the fits with NE2001 and YMW16, respectively. This lower limit is, however, only indicative, since in this analysis, there is no feedback between the derived magnetic field and the propagation of cosmic-ray electrons; see Section 4.2.

The interplay of diffusion height and derived magnetic field parameters can be seen in Figure 12, where the GMF model parameters of the different fits for $h_D \geqslant 4\,\mathrm{kpc}$ are displayed. Especially the fitted scale height z_t of the toroidal field depends strongly on h_D. For $h_D = 4\,\mathrm{kpc}$, only a lower limit on z_t can be estimated. In the following, we will therefore only investigate GMF models derived for n_cre densities within $6 \leqslant h_D/\mathrm{kpc} \leqslant 10$, for which the best-fit values of z_t are finite and compatible with current estimates of the size of the diffusive halo estimated from the analysis of unstable secondary cosmic-ray nuclei.

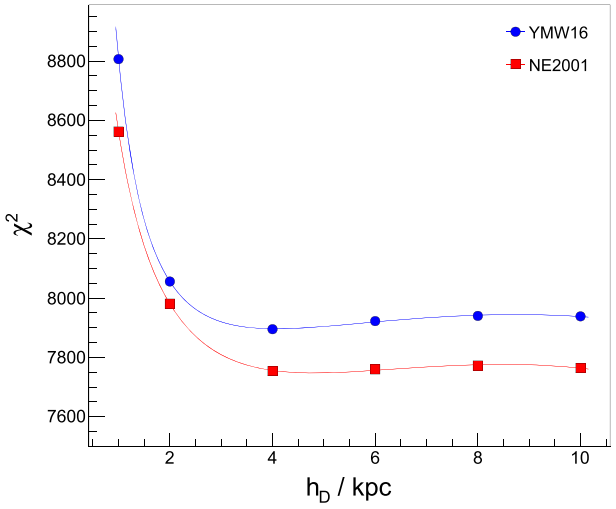

a: Half-height h_D of the cosmic-ray diffusion volume.

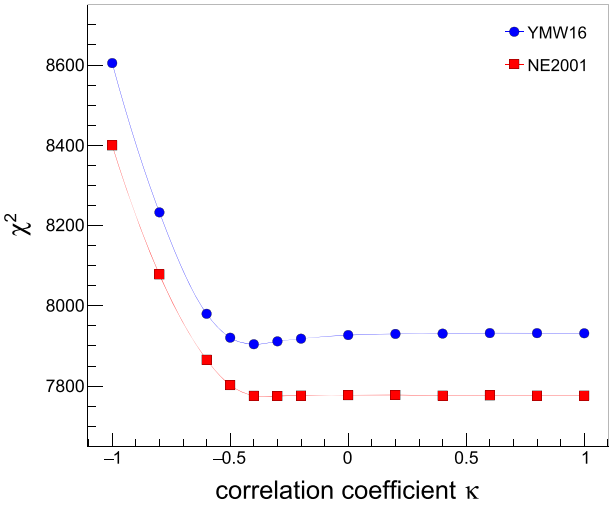

b: Correlation coefficient κ between the magnetic field and thermal electron density.

Figure 11. Goodness of fit, Equation (48), for two different models of the thermal electron density, NE2001 (red) and YMW16 (blue), and as a function of h_D (left) and κ (right).

Table 2
Preselection of Model Variations

ID	Disk	Halo		n_e		n_{cre}		QU	χ^2/ndf	Model Name
		Toroidal	Poloidal	Model	κ	Model	h			
Parametric Models										
a	GD	Explicit	CX-sigm	YMW16	0	DPD	6	(W+P)/2	7923/6500 = 1.22	base
b	GD	Twisted	CX-sigm	YMW16	0	DPD	6	(W+P)/2	8324/6504 = 1.28	
c	GD	Explicit	CX-Gauss	YMW16	0	DPD	6	(W+P)/2	8298/6500 = 1.28	
d	GD	Explicit	CX-sech2	YMW16	0	DPD	6	(W+P)/2	8381/6500 = 1.29	
e	GD	Explicit	CX-expo	YMW16	0	DPD	6	(W+P)/2	8431/6500 = 1.30	expX
f	GD	Explicit	PF-sigm	YMW16	0	DPD	6	(W+P)/2	7926/6500 = 1.22	
g	LS	Explicit	CX-sigm	YMW16	0	DPD	6	(W+P)/2	7991/6501 = 1.23	spur
Thermal Electrons										
h	GD	Explicit	CX-sigm	NE2001	0	DPD	6	(W+P)/2	7759/6500 = 1.19	neCL
i	GD	Twisted	CX-sigm	NE2001	0	DPD	6	(W+P)/2	8221/6504 = 1.26	twistX
j	GD	Explicit	CX-Gauss	NE2001	0	DPD	6	(W+P)/2	8079/6500 = 1.24	
k	GD	Explicit	CX-sigm	YMW16	−0.4	DPD	6	(W+P)/2	7905/6500 = 1.22	nebCor
Cosmic-Ray Electrons										
l	GD	Explicit	CX-sigm	YMW16	0	DPD	8	(W+P)/2	7940/6500 = 1.22	
m	GD	Explicit	CX-sigm	YMW16	0	DPD	10	(W+P)/2	7939/6500 = 1.22	cre10
n	GD	Explicit	CX-sigm	YMW16	0	OS13	10	(W+P)/2	7965/6500 = 1.23	
Synchrotron Data Product										
o	GD	Explicit	CX-sigm	YMW16	0	DPD	6	P	11,013/6500 = 1.69	
p	GD	Explicit	CX-sigm	YMW16	0	DPD	6	W	8845/6500 = 1.36	
q	GD	Explicit	CX-sigm	YMW16	0	DPD	6	CG	9758/6500 = 1.50	synCG
r	GD	Explicit	CX-sigm	NE2001	0	DPD	6	CG	9551/6500 = 1.47	

Note. GD: grand-design spiral; LS: local spur; CX: coasting X-field; PF: power function; OS13, Orlando & Strong (2013); DPD: Dragon plain diffusion; W: WMAP; P: Planck, CG: COSMOGLOBE. The last column gives the name assigned to the eight members of the final GMF ensemble, introduced in Section 7.8.

Concerning the models of the density of thermal electrons in the Galaxy, it can be seen in Figure 11 that the fits with the old NE2001 model result in a consistently better fit quality than the ones performed with the recent YMW16 model. Even though the difference is statistically significant ($\Delta\chi^2 = -167$ at $h_D = 6$), we consider both models in our analysis, since the latter n_e model gives a better description of Galactic pulsar DMs than the former. Switching between these two models has a larger systematic impact on the values of most GMF parameters than a change in h_D; see Figure 12.

7.3. Striation or Correlation?

It is well known that the magnetic field strength derived from the observed RMs is smaller than the one derived from the observed Galactic polarized synchrotron emission. One way to reconcile the two observables is to postulate the existence of an anisotropic or striated random field that fluctuates along the coherent field lines, which leads to an increase in PI without changing the RMs. For our base model, the best-fit value of the striation factor ξ, see

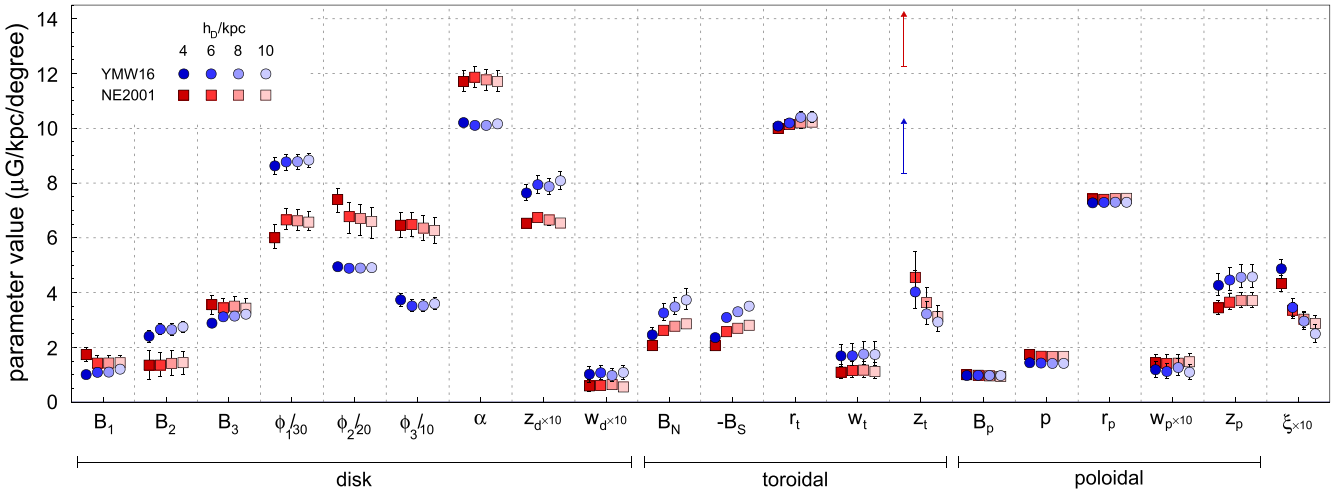

Figure 12. Best-fit parameter values of the disk, toroidal, and poloidal GMF components for different values of the half-height h_D of the cosmic-ray diffusion volume and for two different models of the thermal electron density, NE2001 (red) and YMW16 (blue). See Table 1 for a short explanation of each parameter. Some parameter values have been multiplied by a scale factor, as indicated in the axis labels, to fit in one panel with a single y-axis. 1σ uncertainties are shown as error bars, and arrows indicate the 84% CL lower limits on the parameters.

Equation (8), is

$$\xi_{\rm base} = 0.35 \pm 0.03, \tag{50}$$

implying that the energy density in the coherent and striated field components is almost equal (energy density $u_B \propto B^2$, $B' = (1+\xi)B$, $u_{B'}/u_B = (1+\xi)^2 = 1.8 \pm 0.1$).

Another reason for the mismatch between magnetic fields inferred from RM and PI observations could be an anticorrelation of the thermal electrons and the magnetic field, leading to smaller Faraday rotation than in the uncorrelated case. Here we perform, to our knowledge for the first time, an analysis of RM and PI allowing for a modified RM due to an $n_{\rm e}$–B correlation with coefficient κ, as derived by Beck et al. (2003; see Section 2). Here we use the random field b derived from the total synchrotron intensity measured by Planck (JF12b model of Adam et al. 2016) to evaluate Equation (2) for a fixed value of b but a coherent field B that is allowed to float freely during the fit.

The fits are performed for different values of κ, and the resulting dependence of the fit quality on the correlation coefficient is displayed in Figure 11(b). As can be seen, a large anticorrelation of $n_{\rm e}$ and B is disfavored, and the 5σ lower limit is found to be

$$\kappa \geqslant -0.52 \text{ and } -0.49, \tag{51}$$

where the two values correspond to the fits using the NE2001 and YMW16 models of $n_{\rm e}$, respectively. The optimal fit to the data is at $\kappa \approx -0.4$, but the χ^2 minimum is very broad, and all fits above this value fit the data similarly well. The reason for this degeneracy can be understood by examining the change of fit parameters with κ, as shown in Figure 13. Given the 2 degrees of freedom of rescaling the magnetic field strengths of each model component and the striation factor, it is always possible to match the RM and PI data as long as $\xi > 0$. In the following, we will not further investigate the fits with $\kappa > 0$, since our fiducial fits with $\kappa = 0$ already exhibit a large degree of striation close to equipartition with the coherent field (see above). Instead, we will concentrate on the best fit at $\kappa = -0.4$, where the striation parameter is 0, as an alternative to the fiducial model. At this value of κ, the magnetic field scale is set by the PI data, whereas at $\kappa = 0$, the scale is set by the RM data. In this extreme scenario, where no striated random fields contribute to the PI and the Faraday rotation is diminished by the anticorrelation of B and $n_{\rm e}$, the fitted magnetic field strengths (B_m, $B_{\rm N/S}$, and $B_{\rm p}$) are about a factor of 1.4 larger than in the fiducial case.

7.4. Synchrotron Data Products

The choice of data product for the Stokes Q and U parameters affects the GMF fit due to the differences in the large-scale structure of derived sky maps; see discussion in Section 3.2 and the comparisons shown in Figure 22 in Appendix A. Moreover, and perhaps more importantly, since these differences are relatively small, different products differ by the variance of Q and U within a pixel over which we average these values. Since we use these variances as a weight of the data when optimizing Equation (48), they also affect the outcome of the fit.

For our simple arithmetic average of the Q and U values of Planck and WMAP, the variance is calculated for all data points before averaging; therefore, we expect it to be the arithmetic average of the Planck and WMAP variances plus an additional contribution from the systematic difference between the two products. On average, the variance derived from the Planck and COSMOGLOBE maps is about a factor 0.8 smaller than the one of our default synchrotron map and about the same for the WMAP data. Keeping in mind that WMAP could measure at lower frequencies, where the synchrotron intensity is larger by a factor of $(22.5\,{\rm GHz}/30\,{\rm GHz})^{-3.1} = 2.4$, it is not clear to us to which extent the smaller variance of Planck (and by extension COSMOGLOBE) is actually due to an improved measurement of the synchrotron radiation or due to the use of more aggressive foreground smoothing priors in the analysis.

As a consequence of smaller variances, the fits using Planck and COSMOGLOBE have a χ^2 that is worse than the one of the `base` model by a factor of 1.4 and 1.2, respectively. We have checked that the worse fit is indeed mostly due to the different variances (and not the different values of Q and U) by

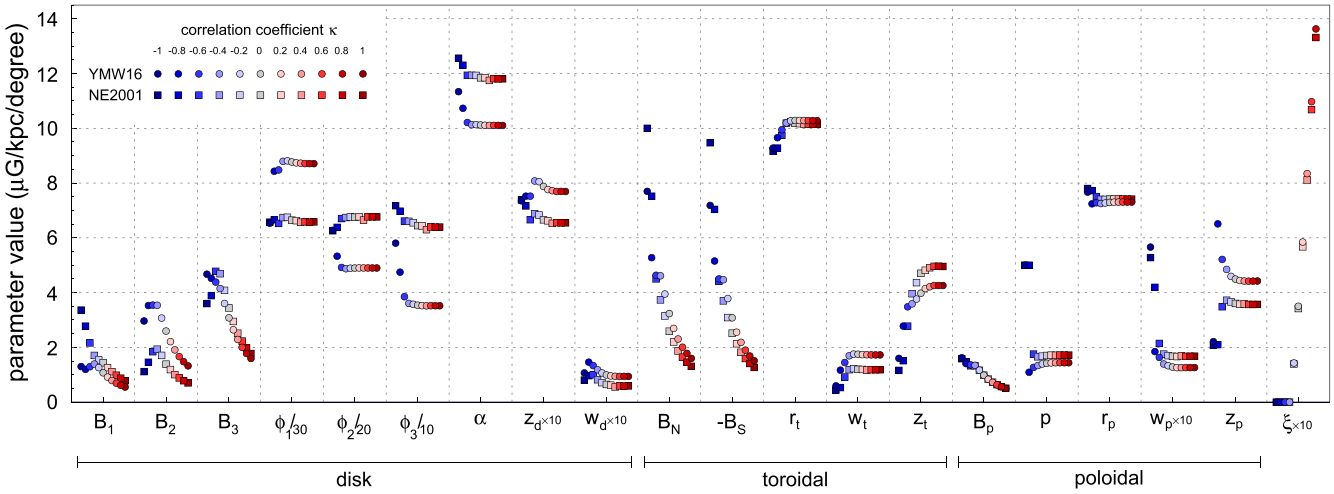

Figure 13. Best-fit parameter values of the disk, toroidal, and poloidal GMF components for different values of the correlation coefficient between the magnetic field and thermal electron density κ and for two different models of the thermal electron density, NE2001 (red) and YMW16 (blue). See Table 1 for a short explanation of each parameter. Some parameter values have been multiplied by a scale factor, as indicated in the axis labels, to fit in one panel with a single y-axis. No parameter uncertainties are shown here; see Figure 12.

performing a fit of the Planck data with our default variances, in which case the fit quality was only worse by a factor of 1.03.

The GMF models obtained with alternative data products are qualitatively similar, but the parameters obtained in these fits differ from the one of the `base` model. The differences are mostly not driven by the systematic differences between the sky maps but rather caused by the larger relative "pull" on the χ^2 of Q and U data with respect to RM data. The sensitivity of the parameter values on the data-driven weights is intrinsic to the method used in this analysis and needs to be considered when estimating the GMF model uncertainties; see Section 7.8 below.

7.5. Disk Field

7.5.1. Grand-design Spiral

Many of the previous attempts to model the global structure of the disk field enforced a certain number of "magnetic arms," often following the inferred large-scale structure of matter density in the Galaxy. Due to our more flexible decomposition of the spiral field into azimuthal Fourier modes, we can let the data decide how much spiral structure is needed. We have fit the RM and PI data using a different number of Fourier modes ranging from one to five. As expected, the fit quality continuously improves with the number of modes $n_{\rm mode}$, since each adds two more free parameters (amplitude and phase) to the fit. Using the Wilks theorem (Wilks 1938), we find that the improvements of the fit quality of the `base` model are significant up to $n_{\rm mode} = 3$, with a $\Delta\chi^2 = 153.2$ going from two to three modes and $\Delta\chi^2 = 12.7$ from three to four modes. The same conclusion is reached using the Bayesian information criterion, BIC $= \chi^2 + n_{\rm par}\ln(n_{\rm data})$ (Schwarz 1978), which is minimal at $n_{\rm mode} = 3$. We have also tested that the required number of modes remains three when changing the height of the diffusion volume, h_D, used to calculate $n_{\rm cre}$ and when using a twisted X-field.

Three azimuthal modes correspond to six "magnetic arms" of alternating polarity. The grand-design configuration of our `neCL` fit variant (using the NE2001 thermal electron model) has already been shown above in the right panel of Figure 7. The best-fit disk field of the `base` model is displayed in the left panel of Figure 14, where we also show the location of tracers of the spiral structure of the matter density of the Milky Way, given here by the measurements of trigonometric parallaxes of high-mass star-forming regions from Reid et al. (2019). As can be seen, we find a remarkable alignment of the fitted magnetic spiral structure and these tracers. Large coherent field strengths are present in the interarm regions, but the coherent field strength is close to zero at the location of the spiral matter segments derived by Reid et al. (2019), shown as lines in Figure 14. This result is similar to what is observed in external galaxies, where the strongest ordered fields are detected in the interarm regions (Beck 2016).

The fitted pitch angle, α, of the disk field is found to be nearly independent of the assumed cosmic-ray halo size, n_e–B correlation coefficient ($\kappa \geqslant -0.4$), and functional form of the magnetic halo. However, the fits with different models of the thermal electron density result in pitch angles that are systematically different with respect to each other by $\pm 1°$; see Figure 12. The average of the value obtained using the NE2001 and YMW16 thermal electron models is

$$\alpha = (11.0 \pm 0.3\ (\text{stat.}) \pm 1.0\ (\text{n}_\text{e}))°. \quad (52)$$

This value is in good agreement with the pitch angle of the local (Orion–Cygnus) spiral arm of ($11\overset{\circ}{.}4 \pm 1\overset{\circ}{.}9$) (Reid et al. 2019) and the pitch angles of $\alpha = (9\overset{\circ}{.}87, ..., 11\overset{\circ}{.}43)$ of the grand-design logarithmic spiral model fitted by Hou & Han (2014) using H II regions as spiral tracers. Thus, the pitch angles of the spiral structure of the magnetic field and the matter density in the Milky Way are about equal, similar to what is observed for external spiral galaxies (Van Eck et al. 2015).

7.5.2. Local Spur

What drives the fit of the grand-design spiral disk field? Is it the RM values at longitudes where the line of sight is tangential to a spiral arm? These magnetic tangents are clearly visible in the predicted RMs in the top left plot of Figure 10, but they are

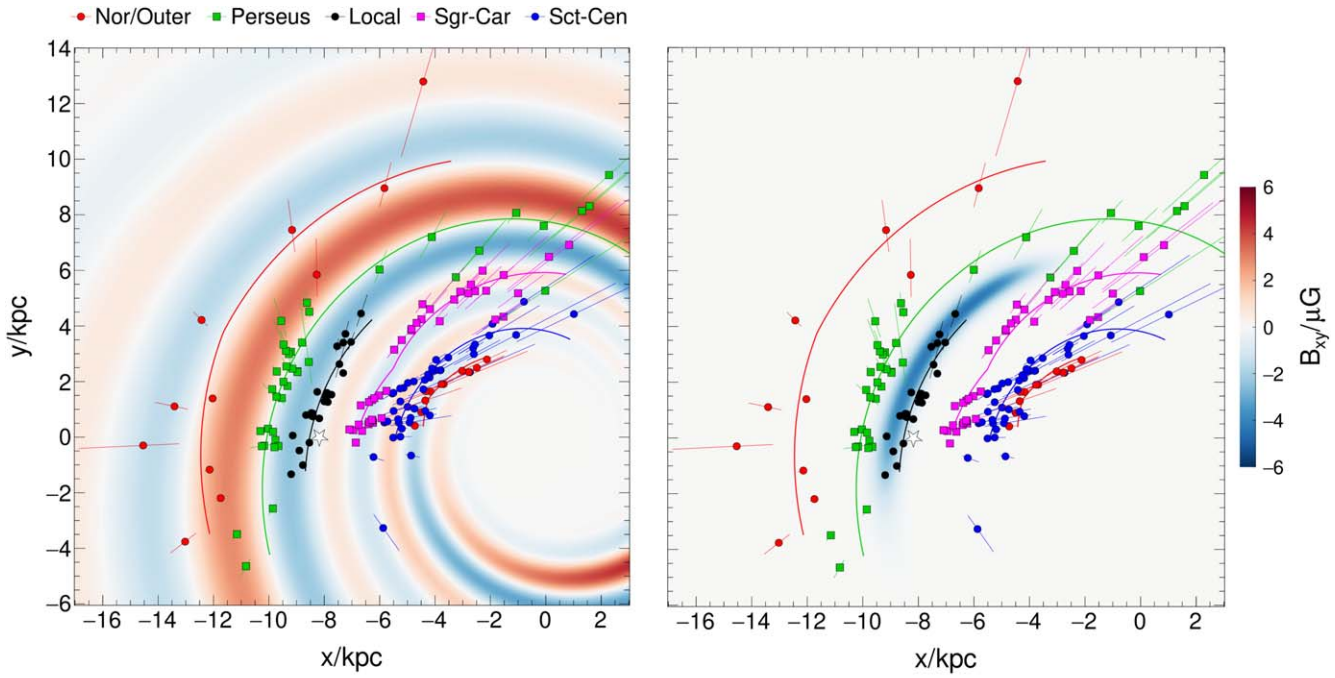

a: Grand-design spiral b: Spiral spur.

Figure 14. Magnetic field of the disk component for the grand-design spiral (left) and spiral spur (right) GMF model. The horizontal magnetic field strength in the x–y plane at $z = 0$ is displayed with colors ranging from blue (counterclockwise field) to red (clockwise field). Superimposed points with distance error bars are the locations of tracers of the spiral structure of the matter density of the Milky Way (high-mass star-forming regions with parallax distances), and the curved colored lines are the inferred location of spiral arm segments, both from Reid et al. (2019).

not so obvious in the RM of the data, possibly due to the large variance present in the data at low latitudes. Alternatively, the fit of the disk field might be mostly determined by the large-scale "butterfly pattern" of RMs, see Equation (19), and therefore mostly from the disk field in the vicinity of the Sun.

To test this possibility, we fit the data without a grand-design magnetic pattern but include only one local magnetic spur, as introduced in Section 5.2.3. The fitted pitch angle of the local spur is $(12\overset{\circ}{.}1 \pm 0\overset{\circ}{.}6)$ and does not depend on the thermal electron model used. The best-fit local spur is displayed in the right panel of Figure 14. It is located at the edge of the local Orion–Cygnus spur and has a magnetic field strength of 4.30 μG at the reference radius of 8.2 kpc. The quality of this fit is found to be slightly worse than the one of the `base` model (7991 instead of 7923) but close enough to conclude that both models are approximately equivalent.

For a closer look at the differences between the `spur` and `base` models, we show the RM values in bands of latitude for the data and the two models in Figure 15. As can be seen, both models give the same overall good description of the longitude-dependence of the RM of the data. The `base` model (shown as red open circles) exhibits distinct RM features at low latitudes, shown in the middle panel for $|b| < 5°$, but none of these are visible in the data.

The near-equivalence of these two radically different disk field models is a consequence of the fact that the extragalactic RMs used in the fit constrain only the integrated Faraday rotation to the edge of the Galaxy. The model degeneracy could, in principle, be broken by including RMs from Galactic pulsars into the fit to provide cumulative RMs at different distances. However, pulsar RMs are currently of limited use, since the distances to most pulsars are not known with sufficient precision. Some previous GMF studies used the "DM distance" (i.e., the distance d at which $\mathrm{DM}' = \int_0^d n_\mathrm{e}(\boldsymbol{x}(r))\, dr$ equals the observed DM) to calculate the model RMs, but this introduces an additional dependence on thermal electron density models that is difficult to account for in the GMF model optimization. Notwithstanding these caveats, it is interesting to note that Han et al. (2018) derived a six-arm grand-design spiral model from the RMs of pulsars and extragalactic sources, which is qualitatively very similar to the disk field of our `base` model. More studies are needed, however, to unequivocally prove the existence of a grand-design magnetic spiral in our Galaxy. Until then, a conservative approach is to consider the two models introduced in this section as extreme possibilities for the coherent magnetic field in the disk of the Milky Way.

7.6. Poloidal Field

We begin by reassessing the need for a poloidal component to describe the data, performing a fit without including such a component. The resulting fit quality deteriorates tremendously, by $\Delta\chi^2 > +2100$ with respect to the `base` model, irrespective of the thermal electron model used in the fit. As can be seen in Figure 10, the poloidal component contributes only a little to the RMs. However it would be incorrect to conclude that the fit cannot determine whether the X-field is coherent or striated, since the Stokes parameters of the model components do not add up linearly (see discussion in Section 7.1). In fact, if a striated X-field were equivalent to a coherent one, then the fit quality would only depend on the orientation and not the direction of the coherent X-field, but the $\Delta\chi^2$ is +8679 when reversing the direction of the X-field.

We also tried to fit the data with a north–south reflection-symmetric X-field (characteristic of an S1 dynamo) instead of a

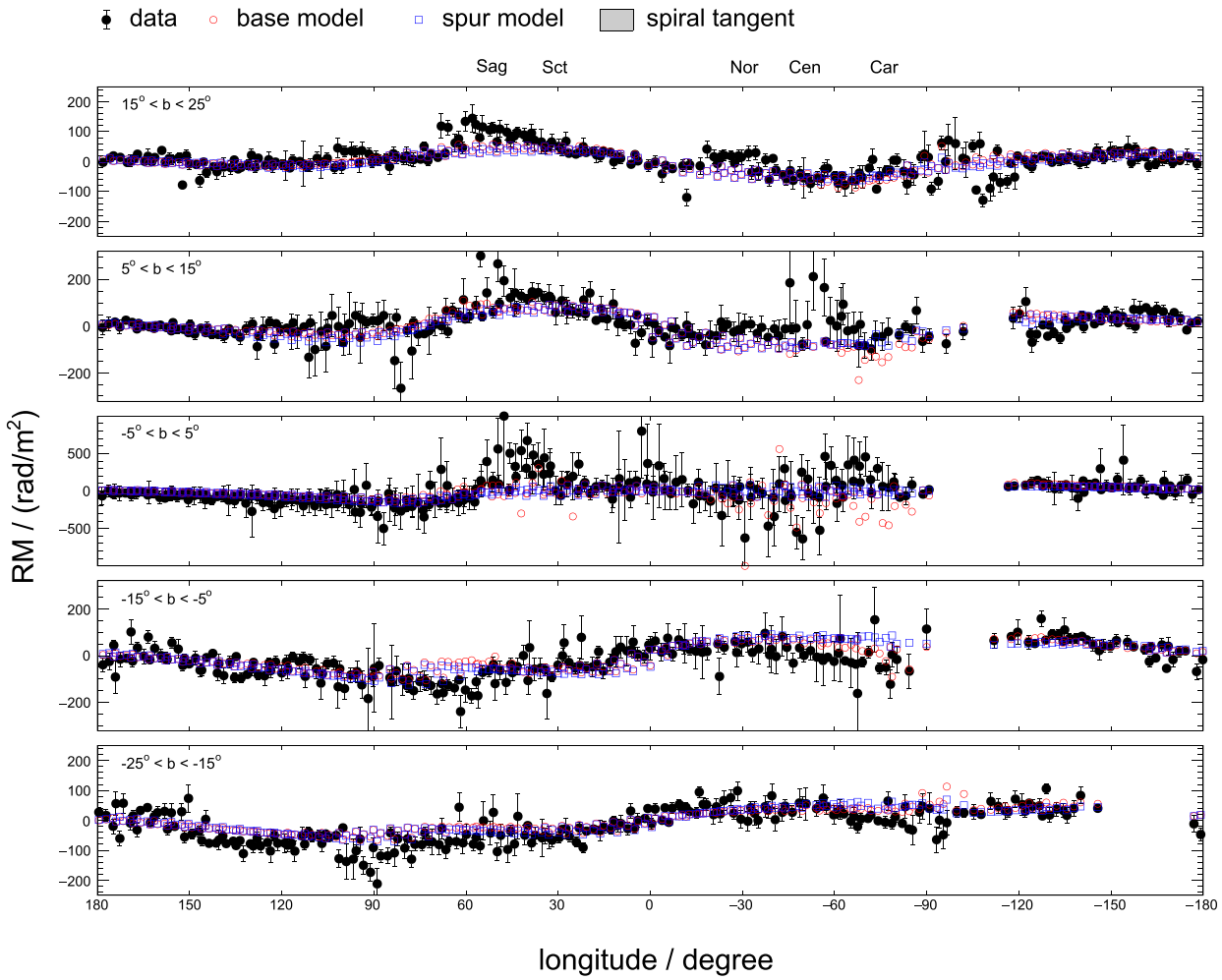

Figure 15. Comparison of data (black points with error bars) and models (red open circles: `base` model with a grand-design spiral disk field; blue open squares: spiral spur model) in five latitude slices around the Galactic plane. Every point is the RM value detected/predicted in one HEALPIX pixel ($N_{\rm side} = 16$). Gray bands are drawn at the longitudes of tangent points of the spiral arms of the Galaxy. The width indicates the range of tangent positions in different observables cataloged by Vallée (2022).

dipolar one (A0 dynamo); however, the fit is much worse ($\Delta\chi^2 > +1700$). Furthermore, we checked for the `base` model if different strengths of the magnetic field normalization $B_{\rm p}$ in the northern and southern hemisphere are preferred by the data. A different value in the two hemispheres would be required by flux conservation if there were a net inward or outward flux in the disk in an $m = 0$ mode. We find that any such asymmetry must be small, since the difference of the fitted values for the two hemispheres is $\Delta B_{\rm p} = (0.12 \pm 0.07)\,\mu$G.

Inspecting the pixel-by-pixel contributions to the χ^2, we find that the poloidal fit is mainly driven by the Q and U data at longitudes $|\ell| < 60°$. Unless a very peculiar foreground is responsible for these large-scale features in Q and U (see discussion in Appendix B), we confirm the conclusions of Jansson & Farrar (2012a) that the PI cannot be described without the presence of a dipolar X-field in the Galaxy.

We find that the data are described equally well by a power function and a coasting X-field ($\chi^2 = 7926$ and 7923, respectively), since the major differences between the field lines of the two models are at large radii, where the field is small; see Figure 8. There is, however, a clear preference regarding the choice of the radial dependence of the midplane vertical field, Equations (29) and (30). The best fit to the data is obtained for the logistic sigmoid function, i.e., for a vertical field strength that is constant with galactocentric radius and then vanishes to zero at a certain radius $r_{\rm p}$ with a transition width $w_{\rm p}$. The tested alternatives of a Gaussian, hyperbolic secant, or exponential radial dependence result in fits that are worse by $\Delta\chi^2 = +370$, +452, and +508. This clear preference for a logistic radial cutoff remains for all model variations tested (power-function or coasting X-field, twisted X-field, and using different thermal electron models).

The improvement of χ^2 when using a logistic instead of an exponential function originates mostly from the RM ($\Delta\chi^2_{\rm RM} = 315$) and Q data ($\Delta\chi^2_Q = 155$) and only to a lesser extent from the U data ($\Delta\chi^2_U = 36$). Much of the improvement in $\chi^2_{\rm RM}$ is concentrated in one swath of the RM sky located at $\ell \approx (-30° \pm 15°)$ and $90° < b < 150°$, and most of the decrease in χ^2_Q is due to a better description of the data at $15° < \ell < 30°$ and $b > 0°$. Since we cannot be certain that these features at intermediate angular scales are global, we conservatively keep the exponential radial function as an extreme variation in our model ensemble.

The best-fit midplane poloidal magnetic field strengths, derived for different radial functions, are shown in Figure 16. The largest differences of $B_0(a)$ are at small radii, $a \lesssim 4$ kpc, where the fit of the poloidal field strength is unconstrained due

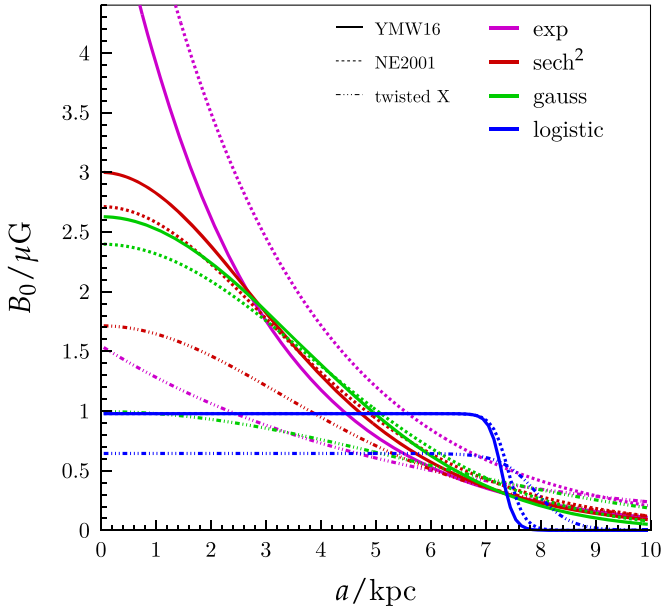

Figure 16. Best-fit radial dependence of the z-component of the poloidal magnetic field at $z = 0$, $B_0(a)$; see Equations (22) and (23). Different radial functions are shown in different colors; see Equations (29) and (30). Variations in the thermal electron density and toroidal field type used during the fit are shown with different line styles, as indicated in the figure legend.

to the large number of Q and U pixels masked at $|\ell| < 30°$. The logistic model used in our `base` model has a midplane vertical field strength of $B_p = (0.98 \pm 0.03)\ \mu$G and cuts off inside the solar circle at $r_p = (7.29 \pm 0.06)$ kpc with a transition width of $w_p = (0.112 \pm 0.029)$ kpc. In the case of the twisted X-field model, the transition is fitted to be at a somewhat large radius, and the transition is broader ($r_p \sim 7.9$ kpc, $w_p \sim 0.3$ kpc). The `expX` model leads to a large vertical magnetic field at the Galactic center, $B_p = (5.8 \pm 0.4)\ \mu$G, that falls off exponentially with a scale length of $r_p = (2.5 \pm 0.1)$ kpc. For comparison, the poloidal field of the JF12 model is of similar strength, with $B_p = (4.6 \pm 0.3)\ \mu$G and $r_p = (2.9 \pm 0.1)$ kpc.

Thus, the `expX` and `base` models bracket the possible range of the radial dependence of the strength of the poloidal field. The corresponding uncertainty of the GMF, quantified here for the first time, must be taken into account when interpreting the arrival directions of ultrahigh-energy cosmic rays and when discussing the radial dependence of cosmic-ray energy spectra derived from gamma-ray observations (e.g., Gabici et al. 2019). A better understanding of the polarized foregrounds is needed to be able to further constrain the GMF fits by including PI data toward the Galactic center.

7.7. Toroidal Field

Fitting for an "explicit" toroidal halo field, we obtain a radial extent of $r_t = (10.2 \pm 0.2)$ kpc and a vertical scale height of $z_t = (4.0 \pm 0.7)$ kpc within our `base` model. The estimate of the radial extent of the halo is very stable with respect to any of the model variations we have studied. The vertical scale is less certain, ranging from 2.9 to 6.1 kpc, where the lowest value is obtained assuming a large cosmic-ray diffusion volume with $h_D = 10$ kpc.

The magnitude of azimuthal field strength in the northern and southern hemispheres was found to vary between about 2 and 5 μG, depending on the model variation under study. For the `base` model, the best-fit values are $B_N = 3.3 \pm 0.3\ \mu$G and $B_S = -3.1 \pm 0.3\ \mu$G. In all the studied variations, the magnitude of the northern and southern magnetic field strength is found to be compatible within the estimated uncertainties,

$$B_N = -B_S, \tag{53}$$

which strongly suggests a common origin of the toroidal field in the two hemispheres.

Our unified halo model (`twistX`) naturally explains the relationship in Equation (53), since the magnetic field in both hemispheres originates from the shearing caused by the same velocity field. Furthermore, the unified halo model has the practical virtue that its built-in connection between the radial extent of the poloidal and toroidal components should make it less prone to overfitting local structures in the data. This suggests that a fitted common radial scale with a large transition width (see the dashed–dotted blue line in Figure 16) might prove to be a more accurate description of the global structure of the GMF.

While the fit quality of the twisted X-field is considerably worse than that of a fit with a separate toroidal and poloidal halo field ($\Delta\chi^2 = +401$ for model a versus b and $\Delta\chi^2 = +462$ for model h versus i), there are only six free parameters for the halo, instead of the 10 parameters needed for the `base` model. On a technical level, the better χ^2 of the `base` model can be due to the freedom of two different radial cutoff values, r_p and r_t, for the toroidal and poloidal components that are available in the fit with an explicit toroidal halo. A future implementation of the unified halo model, in which a physically motivated model limits the buildup of the toroidal field, could introduce additional radial and vertical dependencies to the amount of twist and hence result in a potentially even better description of the halo field.

In summary, the unified halo model describes the data well using only six free parameters for the halo, instead of the 10 parameters needed for the `base` model. This is the first quantitative demonstration of earlier conjectures that the toroidal halo of the Milky Way likely arose dynamically from differential rotation.

7.8. Model Ensemble

Based on the results presented in the previous sections, we compiled a list of viable GMF variations in Table 2. Here we already preselected models with $h_D \geqslant 6$ kpc, see Section 7.2, and used only the most extreme n_e–B anticorrelation of $\kappa = -0.4$; see Section 7.3. This leads to 18 GMF models consisting of seven variations of the parametric models, three variations using NE2001 rather than YMW16, one variation including an n_e–B anticorrelation, three fits with different cosmic-ray electron models, and four fits with different synchrotron products.

How different are these 18 GMF models from each other? One possible way to measure the model differences is to study the motion of charged particles in the respective models and calculate the space-angle difference in their direction after traversing the Galaxy. We performed such comparisons for many particles (rigidity $\mathcal{R} = 10^{19}$ V) starting in different directions from Earth and determined the average deflection difference, its 90% quantile, and the maximum difference for each model combination. The result is shown in Figure 17. Based on these model-to-model comparisons, we can further narrow down the most important variations that encompass the

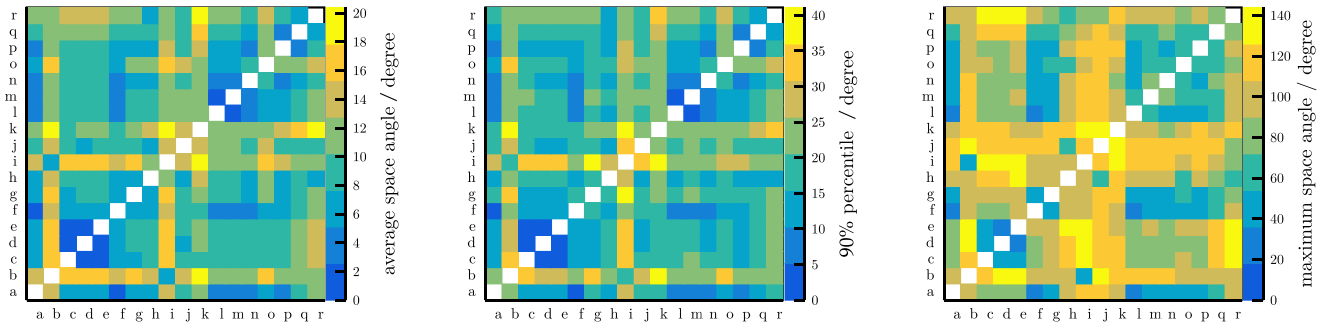

Figure 17. Comparison of models i = a–r and j = a–r (see Table 3) using the space angle $\theta_{ijk} = \arccos(\boldsymbol{u}_{ik}, \boldsymbol{u}_{jk})$ between the direction of charged particles ($\mathcal{R} = 1 \times 10^{19}$ V) backtracked to the edge of the Galaxy analyzed for sky maps of arrival directions k at Earth with a resolution of $N_{\rm side} = 32$. Left: average θ; middle: 90th percentile of θ distribution; right: maximum θ.

GMF uncertainties. For instance, it can be seen that of the four models with different synchrotron products, (a, o, p, q), the COSMOGLOBE model (q) differs the most from the `base` model (a). The difference is similar when comparing the combination of NE2001 and COSMOGLOBE (q) to NE2001 with default synchrotron (h).

Similar comparisons lead us to select the set of eight GMF models identified by the model acronym name in the last column of Table 2. The parameters of the eight members of this final GMF model ensemble are given in Table 3, and their properties can be summarized as follows.

1. `base` is tuned to the data using the YMW16 thermal electron model and a cosmic-ray electron model calculated for a diffusion volume with a half-height of 6 kpc. The parametric model of the GMF is the sum of a spiral disk field, an explicit toroidal halo, and a coasting poloidal X-field.
2. `expX` uses an exponential dependence of the midplane vertical poloidal field instead of the default logistic radial cutoff.
3. `spur` reduces the grand-design spiral disk field to a single local spur (Orion arm).
4. `neCL` replaces thermal electron model YMW16 with NE2001 of Cordes & Lazio (2002).
5. `twistX` has a "twisted X-field" resulting from a unified model of the toroidal and poloidal halos.
6. `nebCor` assumes an anticorrelation between the thermal electron density and the magnetic field strength.
7. `cre10` uses a cosmic-ray electron model in which the half-height of the diffusion halo is increased to 10 kpc.
8. `synCG` swaps the default synchrotron product for the estimate from the COSMOGLOBE analysis.

The total energy of the coherent magnetic field within a 20 kpc radius in these eight models, respectively, is {1.3, 1.5, 1.2, 1.2, 0.6, 2.3, 1.2, 1.0} 10^{55} erg. For the base model, for instance, the disk, poloidal, and toroidal components contribute {0.28, 0.26, 0.75} 10^{55} erg to the total.

8. Applications

Each of the eight GMF model variations introduced in the previous section can be considered a viable estimate of the GMF given the current RM, Q, and U data, and the differences between the models can be regarded as an estimate of the lower limit on the uncertainty of our knowledge of the magnetic field of the Galaxy.

In this section, we discuss two applications in which we propagate the uncertainties of the GMF to uncertainties in the deflection of ultrahigh-energy cosmic rays and the conversion probability of axions in the GMF.

8.1. Cosmic-Ray Deflections

Given the arrival direction $\boldsymbol{v}$ of an ultrahigh-energy cosmic-ray particle at Earth, the knowledge of the GMF can be used to infer its arrival direction at the edge of the Galaxy $\boldsymbol{u}$. In Figure 18, we show sky maps of the *deflection angle* $\theta_{\rm def} = \arccos(\boldsymbol{uv})$ for each of the eight models and the JF12 model at a particle rigidity of 20 EV (1 EV = 10^{18} V). These were obtained by numerically integrating (Cash & Karp 1990; Argiro et al. 2007) the equation of motion of a negatively[20] charged particle in the GMF until it leaves the Galaxy at a Galactocentric radius of $r_{\rm max} = 30$ kpc. The magnitude of the deflection angle is indicated by colors at each of the starting directions $\boldsymbol{v}$ on a HEALPIX grid with $N_{\rm side} = 64$, and the direction of the deflection is indicated by an arrow for a subset of directions on an $N_{\rm side} = 16$ grid if $\theta_{\rm def} > 1°$. As can be seen, all eight models exhibit qualitatively similar deflection patterns but with quantitative differences, as is to be expected from the results presented in the last section. For instance, the `nebCor` model has the largest deflections because in this model, the magnetic field scale is set by the polarized synchrotron data, not by the RMs. And as expected, the `expX` model has the largest deflections for trajectories close to the Galactic center, where it has a 6 times larger poloidal field strength than the `base` model. All models exhibit a left–right asymmetry with deflections being larger if the particle is backtracked toward positive longitudes and smaller for negative longitudes. This is the consequence of the twisted nature of the halo field.

For a closer look at the differences between the models, we show the backtracked directions $\boldsymbol{u}$ in Figure 19 for a small set of arrival directions $\boldsymbol{v}$. The particle rigidity is again 20 EV, and $\boldsymbol{u}$ and $\boldsymbol{v}$ are connected by lines interpolating the backtracked directions at higher rigidities. This figure illustrates the similarity of the models, since in many directions all of them roughly agree on the overall direction of the deflection, but also shows the model uncertainties, visible as a scatter in predicted directions for the ensemble of models. It is worth noting that the deflections predicted by the widely used JF12 model are generally within the range of deflections predicted for the GMF models derived in this work. This is not the case for the

[20] Backtracking a negatively charged test particle yields the forward trajectory of a positively charged cosmic ray.

Table 3
Parameter Values and Uncertainties for the Eight GMF Model Variations

Name	base	expX	spur	neCL	twistX	nebCor	synCG	cre10	Unit
Disk Field									
α	10.11 ± 0.13	10.03 ± 0.13	12.1 ± 0.6	11.9 ± 0.4	12.1 ± 0.4	10.15 ± 0.14	9.90 ± 0.13	10.16 ± 0.13	deg
$z_{\rm d}$	0.794 ± 0.032	0.715 ± 0.024	0.750 ± 0.027	0.674 ± 0.018	0.94 ± 0.05	0.812 ± 0.027	0.622 ± 0.018	0.808 ± 0.033	kpc
$w_{\rm d}$	0.107 ± 0.026	0.099 ± 0.023	0.123 ± 0.024	0.061 ± 0.020	0.15 ± 0.07	0.119 ± 0.025	0.067 ± 0.018	0.108 ± 0.025	kpc
B_1	1.09 ± 0.14	0.99 ± 0.15	-4.30 ± 0.18	1.43 ± 0.26	1.37 ± 0.17	1.41 ± 0.19	0.81 ± 0.12	1.20 ± 0.14	μG
B_2	2.66 ± 0.21	2.18 ± 0.22	⋯	1.4 ± 0.4	2.01 ± 0.30	3.53 ± 0.27	2.06 ± 0.20	2.75 ± 0.21	μG
B_3	3.12 ± 0.15	3.12 ± 0.16	⋯	3.44 ± 0.34	1.52 ± 0.26	4.13 ± 0.21	2.94 ± 0.14	3.21 ± 0.15	μG
ϕ_1	263 ± 9	247 ± 10	155.9 ± 1.4	200 ± 11	236 ± 11	264 ± 8	230 ± 13	265 ± 8	deg
ϕ_2	97.8 ± 2.8	98.6 ± 3.2	⋯	135 ± 12	102 ± 10	97.6 ± 3.2	97.4 ± 3.3	98.2 ± 2.8	deg
ϕ_3	35.1 ± 2.2	34.9 ± 2.4	⋯	65 ± 4	56 ± 6	36.4 ± 2.5	32.9 ± 2.4	35.9 ± 2.2	deg
$w_{\rm S}$	⋯	⋯	10.3 ± 0.6	⋯	⋯	⋯	⋯	⋯	deg
$\phi_{\rm c}$	⋯	⋯	157.2 ± 3.0	⋯	⋯	⋯	⋯	⋯	deg
$L_{\rm c}$	⋯	⋯	31.8 ± 3.0	⋯	⋯	⋯	⋯	⋯	deg
Toroidal Halo									
$B_{\rm N}$	3.26 ± 0.31	2.71 ± 0.19	2.93 ± 0.23	2.63 ± 0.17	⋯	4.6 ± 0.4	2.40 ± 0.12	3.7 ± 0.4	μG
$B_{\rm S}$	-3.09 ± 0.30	-2.57 ± 0.18	-2.60 ± 0.21	-2.57 ± 0.17	⋯	-4.5 ± 0.4	-2.09 ± 0.11	-3.50 ± 0.35	μG
$z_{\rm t}$	4.0 ± 0.7	5.5 ± 0.9	6.1 ± 1.4	4.6 ± 0.8	⋯	3.6 ± 0.6	5.6 ± 0.8	2.9 ± 0.4	kpc
$r_{\rm t}$	10.19 ± 0.17	10.13 ± 0.19	9.75 ± 0.13	10.13 ± 0.20	⋯	10.21 ± 0.17	9.42 ± 0.08	10.41 ± 0.20	kpc
$w_{\rm t}$	1.7 ± 0.4	2.1 ± 0.6	1.42 ± 0.30	1.15 ± 0.29	⋯	1.7 ± 0.4	0.92 ± 0.16	1.7 ± 0.4	kpc
t	⋯	⋯	⋯	⋯	54.7 ± 1.1	⋯	⋯	⋯	Myr
Poloidal Halo									
$B_{\rm p}$	0.978 ± 0.033	5.8 ± 0.4	0.99 ± 0.04	0.984 ± 0.031	0.628 ± 0.020	1.35 ± 0.04	0.809 ± 0.024	0.969 ± 0.034	μG
p	1.43 ± 0.09	1.95 ± 0.14	1.40 ± 0.09	1.68 ± 0.11	2.33 ± 0.10	1.34 ± 0.10	1.58 ± 0.09	1.42 ± 0.09	⋯
$z_{\rm p}$	4.5 ± 0.4	2.37 ± 0.22	4.5 ± 0.4	3.65 ± 0.28	2.63 ± 0.10	4.8 ± 0.5	3.53 ± 0.24	4.6 ± 0.4	kpc
$r_{\rm p}$	7.29 ± 0.06	2.50 ± 0.07	7.20 ± 0.06	7.41 ± 0.05	7.92 ± 0.04	7.25 ± 0.07	7.46 ± 0.05	7.30 ± 0.06	kpc
$w_{\rm p}$	0.112 ± 0.029	⋯	0.123 ± 0.034	0.142 ± 0.030	0.291 ± 0.035	0.143 ± 0.033	0.150 ± 0.022	0.109 ± 0.027	kpc
$a_{\rm c}$	⋯	6.2 ± 0.8	⋯	⋯	⋯	⋯	⋯	⋯	kpc
Other Model Parameters									
κ	0	0	0	0	0	-0.4	0	0	⋯
ξ	0.346 ± 0.034	0.51 ± 0.04	0.330 ± 0.033	0.336 ± 0.029	0.78 ± 0.04	0	0.63 ± 0.04	0.250 ± 0.033	⋯

Note. See Table 1 for a description of the parameters and Table 2 for the definition of each model variation.

deflections calculated with the GMF model of Pshirkov et al. (2011), due to the absence of a poloidal component in that model (see Section 7.6).

Current studies of the anisotropies of ultrahigh-energy cosmic rays indicate the presence of "hot spots" of cosmic-ray clusters at intermediate angular scales of 20° (Abbasi et al. 2014; Abreu et al. 2022). For the identification of extragalactic sources related to these overdensities, a precision in back-tracking through the GMF at least as good as their angular size, $\theta_{\rm max}$, is needed. Figure 20 aims to illustrate this requirement. In the left panel, we show the minimum rigidity such that the deflection for a cosmic ray arriving in the given direction is less than $\theta_{\rm max} = 20°$ in all eight models. Requiring that the deflections in half of the sky are less than $\theta_{\rm max} = 20°$, according to all of these models, requires the rigidity to be greater than or equal to $R_{50}^{\rm nocorr} = 20$ EV.

The minimum rigidity requirement improves considerably if the arrival directions are corrected for their expected deflection in the GMF. The limit on the precision with which we infer the source position arises from the *difference* between the models and not the overall magnitude of the deflection. The differences of the predicted deflections within the model ensemble are smaller than the deflections themselves. Therefore, as shown in the right panel of Figure 20, the required minimum rigidity is lower when the deflections are corrected for. With corrections, the rigidity quantile at which half of the sky can be observed at $\theta_{\rm max} = 20°$ or better decreases to $\mathcal{R}_{50}^{\rm corr} = 11$ EV, giving a much greater observational reach. Note that this discussion is indicative only, since the minimal rigidity requirement may change when random fields are included in the analysis.

8.2. Axions

Another important application of the model ensemble presented in this paper is the prediction of the conversion of astrophysical axion-like particles (e.g., Jaeckel & Ringwald 2010) to photons in the GMF. The general expression for axion–photon conversion in a plasma was derived by Raffelt & Stodolsky (1988). In the limit of small conversion probability, applicable due to known constraints, we can use the expression given in Equation (S5) of Dessert et al. (2020) for the axion-to-photon conversion probability between the source, located at $r_{\rm src}$, and the observer, located at the origin,

$$p_{a\gamma} = \frac{g_{a\gamma\gamma}^2}{4} \sum_{i=1,2} \left| \int_{r_{\rm src}}^{0} {\rm d}r \; B_i(r) e^{i\Delta_a r - i \int_{r_{\rm src}}^{r} dr' \Delta_{||}(r')} \right|^2$$
$$\approx 2.3 \times 10^{-6} \left(\frac{g_{a\gamma\gamma}}{10^{-12}\ {\rm GeV}^{-1}} \sum_{i=1,2} \frac{\int_{r_{\rm src}}^{0} {\rm d}r B_i(r)}{\rm kpc\ \mu G} \right)^2 . \quad (54)$$

The integral is along the line of sight from source to observer, and the subscripts $i = 1, 2$ refer to the transverse components of the magnetic field relative to the line of sight. Current

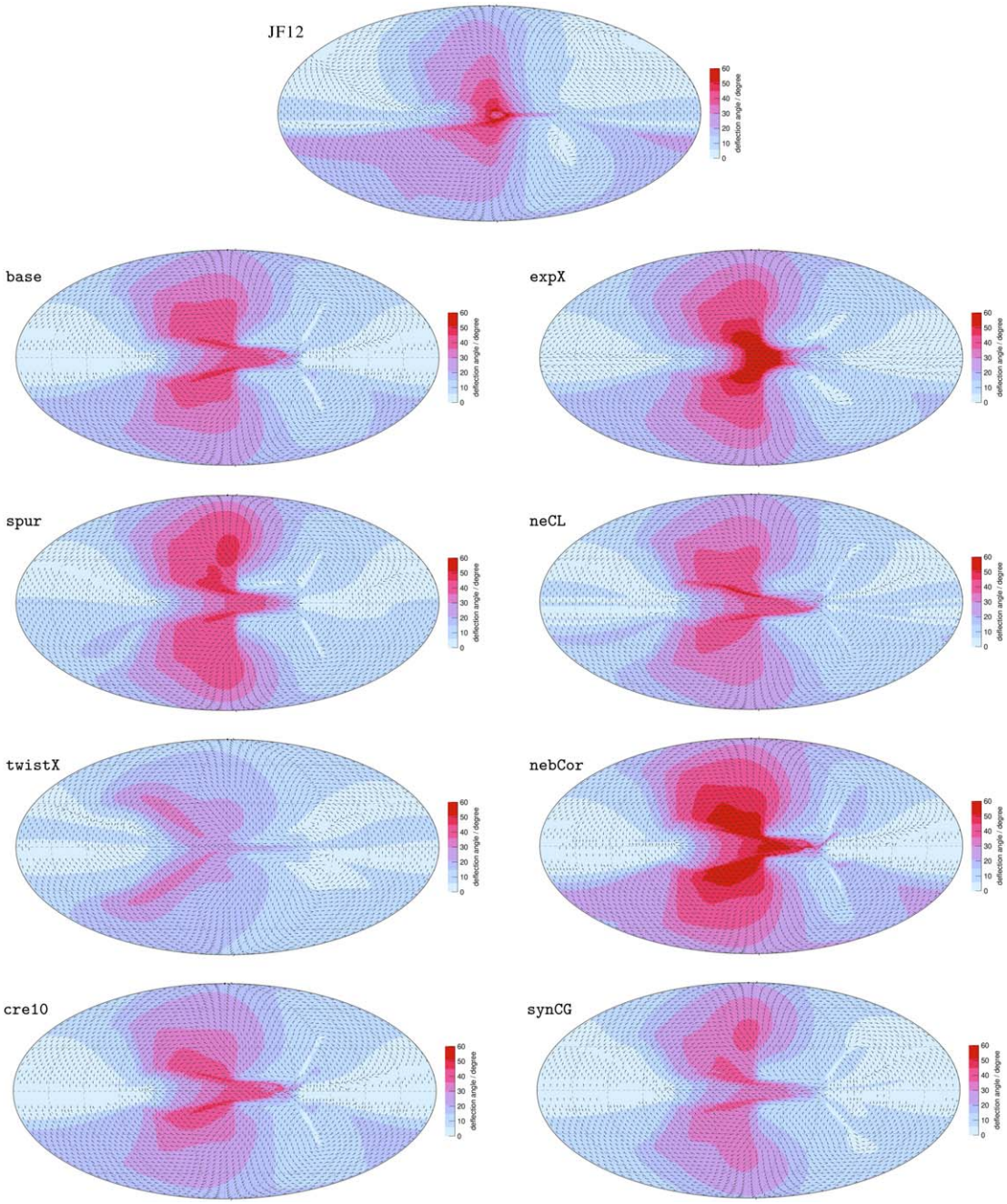

Figure 18. Angular deflections of ultrahigh-energy cosmic rays in the JF12 model (top) and the eight model variations derived in this paper. Colors and arrows denote the size and direction of the deflection in the GMF following the particles from Earth to the edge of the Galaxy. Positions on the sky map denote arrival directions at Earth. The rigidity is 2×10^{19} V.

limits on the axion–photon coupling strength are $g_{a\gamma\gamma} \lesssim$ few $\times\ 10^{-12}\,\mathrm{GeV}^{-1}$ in the low-axion-mass regime ($m_a \lesssim 10^{-6}$ eV; Workman et al. 2022). The effective wavenumbers entering the phase shift are $\Delta_a \equiv -m_a^2/(2E)$ and $\Delta_{||}(r') \equiv -\omega_\mathrm{p}(r)^2/(2E)$, where the plasma frequency $\omega_\mathrm{p} \approx 3.7\ \times 10^{-12}(n_\mathrm{e}/10^{-2}\mathrm{cm}^{-3})^{-1/2}$ eV. Thus, in the limit of large axion energies and low axion mass, the conversion probability simplifies to the last expression that depends only on the coupling constant and the line-of-sight integral of the traverse magnetic field as given in the second line of Equation (54). We checked the validity range of this approximation by comparing it to the conversion probabilities in the JF12 magnetic field calculated with the `gammaALPs` package (Meyer et al. 2022) and found good agreement for $E_a \gtrsim 1$ TeV and $m_a \lesssim 10^{-8}$ eV.

The effects of the new magnetic field models derived in this paper on the predicted axion–photon conversion probabilities are shown in Figure 21, where we assumed $g_{a\gamma\gamma} = 5 \times 10^{-12}\,\mathrm{GeV}^{-1}$. These figures look qualitatively very similar to the ones for the cosmic-ray deflections, Figure 18, since both the conversion probability and the deflection depend on the perpendicular component of the magnetic field. The reason for the asymmetry of the conversion probability in longitude is again the twisted nature of the Galactic halo field. For a given extragalactic axion source candidate, the uncertainty of conversion probability can be

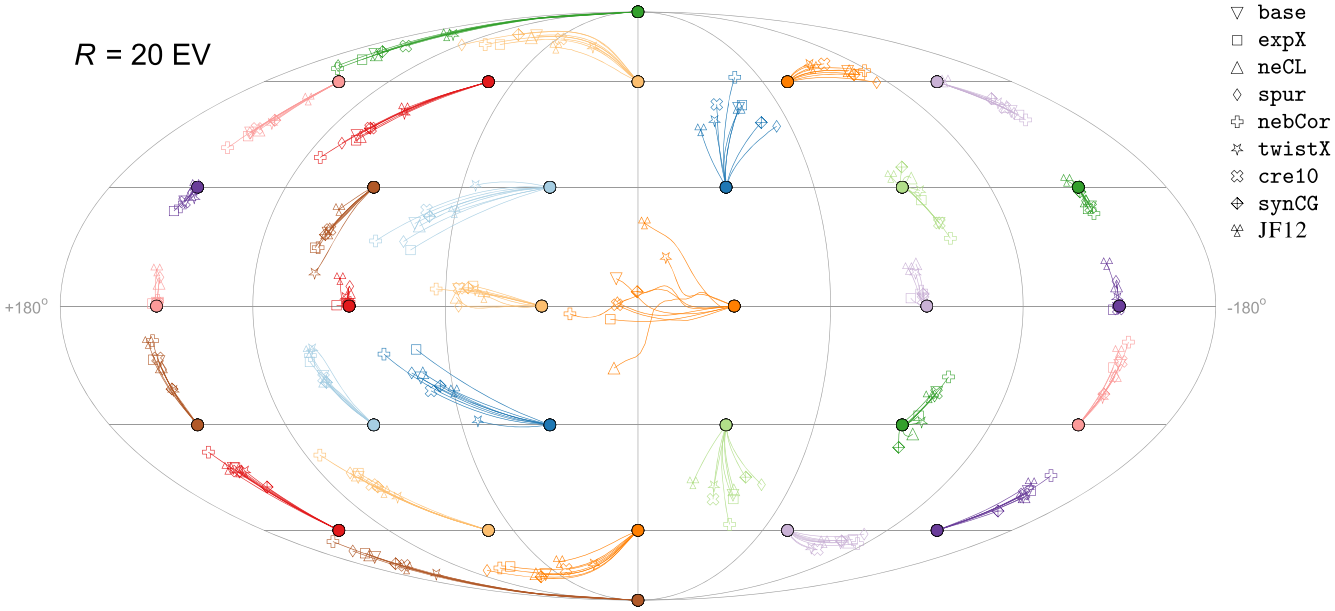

Figure 19. Angular deflections of ultrahigh-energy cosmic rays in the eight model variations derived in this paper and JF12. The cosmic-ray rigidity is 20 EV (2×10^{19} V). Filled circles denote a grid of arrival directions, and the open symbols are the backtracked directions at the edge of the Galaxy.

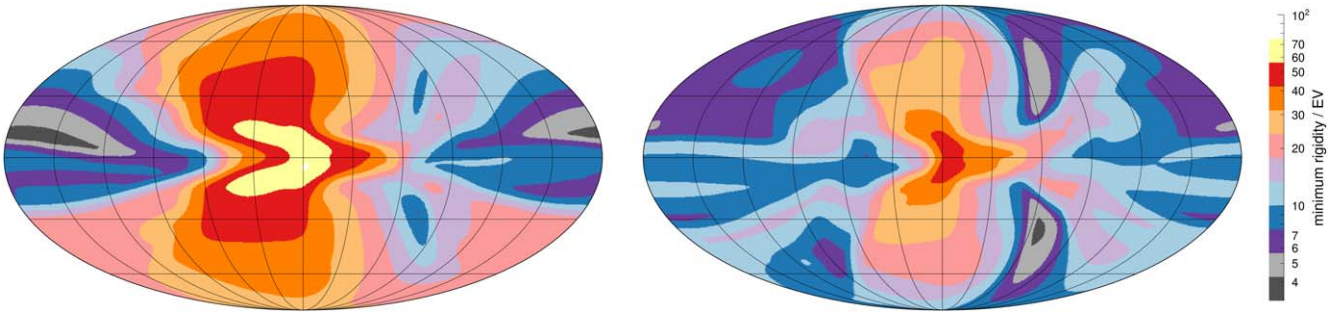

Figure 20. Left: rigidity threshold such that the angular deflection in the given direction is $\leqslant 20^\circ$ in all models. Right: rigidity threshold such that the model predictions of the angular deflection differ by $\leqslant 20^\circ$ (1 EV = 10^{18} V).

estimated by finding the maximum and minimum prediction in the model ensemble in the direction of the source.

9. Summary

In this paper, we have developed new, improved models of the coherent magnetic field of the Milky Way with better functional descriptions of the disk and poloidal fields of the Galaxy, as well as the first step toward a unified model for the toroidal and poloidal magnetic halo. We improve on previous analyses by using more and better variants of auxiliary models for the thermal and cosmic-ray electron densities. The parameters of these new models are constrained with the latest RM and PI data, which we have subjected to detailed scrutiny to resolve or reveal discrepancies.

Equipped with these improvements and with a fast optimization framework that made it computationally feasible to investigate many model variations, we can infer the following insights about the coherent magnetic field of the Milky Way.

1. The local pitch angle of the disk field is $(11^\circ \pm 1^\circ)$.
2. A magnetic field arranged as a grand-design spiral in the Galactic disk fits the data well; interestingly, the inferred field reversals occur at the position of tracers of the spiral arms of the matter density. However, a grand-design spiral is not needed: a model with only a coherent local spur describes the RM and PI data equally well.
3. Within the 10% statistical precision of the data, the magnitude of the toroidal halo field is the same below and above the disk.
4. The vertical scale height of the inferred toroidal halo is anticorrelated to the assumed half-height of the cosmic-ray diffusion volume, with a lower 5σ limit of $h_D \geqslant 2.9$ kpc.
5. Compatibility of the magnetic field strengths inferred from the RM and PI data can be achieved either through a striated random field having about the same energy density as the coherent field or through an anticorrelation between the thermal electrons and magnetic field strength with a coefficient of -0.4.
6. The new data corroborate the existence of the poloidal halo field introduced in JF12 with high significance. The strength of the poloidal field in the inner Galaxy is currently not well constrained due to the need for masking local structures.
7. A simple unified halo model, in which the toroidal field is generated by the shearing of the poloidal field due to the Galactic rotation, fits the data well with only six instead of the usual 10 free halo parameters.

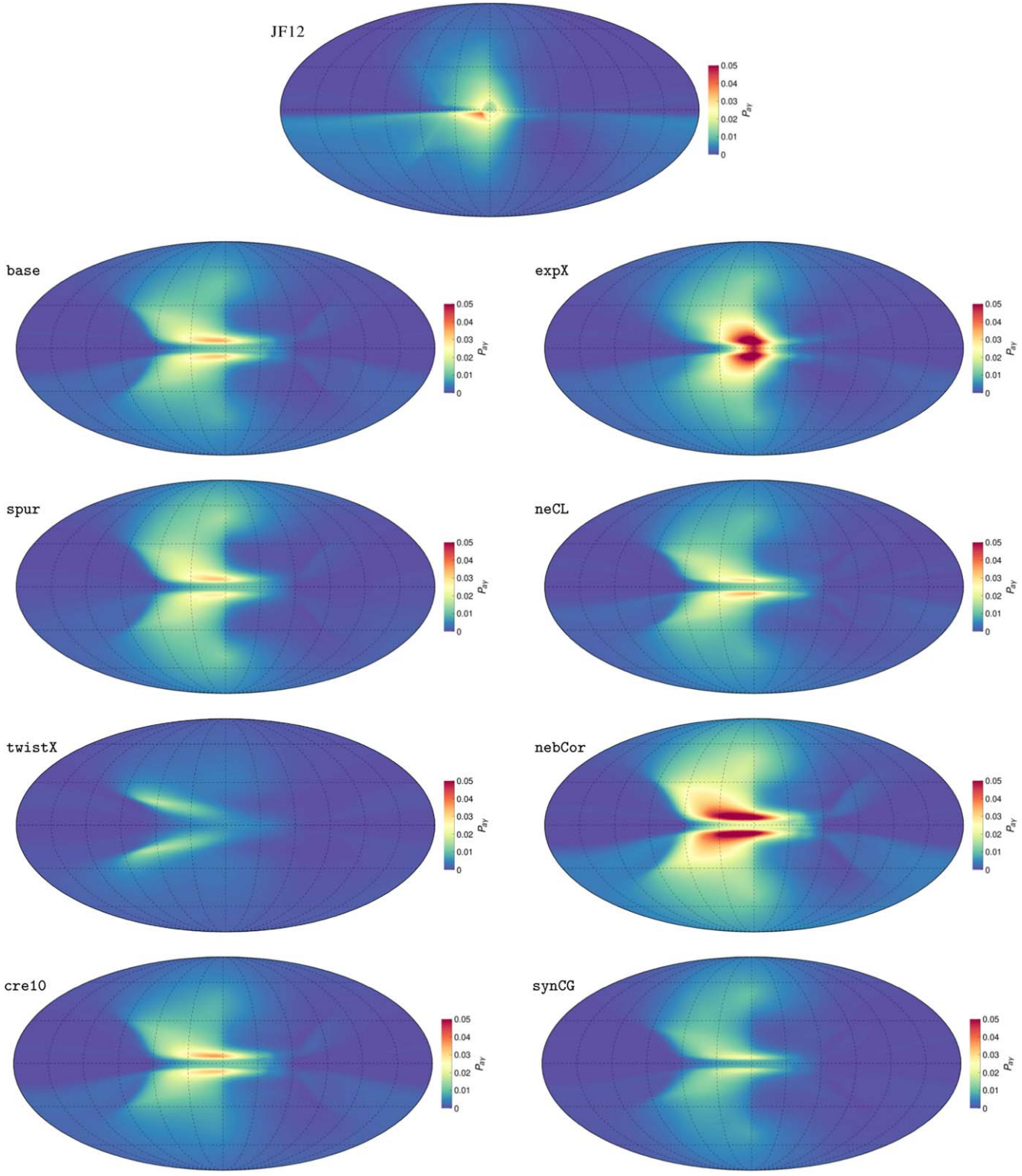

Figure 21. Axion–photon conversion probabilities, $p_{a\gamma}$, for the JF12 model (top) and the eight model variations derived in this paper ($g_{a\gamma\gamma} = 5 \times 10^{-12}\,\mathrm{GeV}^{-1}$, $E_a \gtrsim 1$ TeV, and $m_a \lesssim 10^{-8}$ eV).

We selected an ensemble of eight model variations[21] that encompass a large range of assumptions that are compatible with the data; see Table 3. As a first application, we employed these variations to study the deflections of ultrahigh-energy cosmic rays in the GMF. We find that the deflections predicted by the widely used JF12 model are close to the ones from the new model ensemble. An important conclusion of our work is that the UHECR deflection uncertainties derived from the model ensemble are smaller than the deflection itself for most of the sky at ultrahigh energies, and we can localize the regions of greatest uncertainty.

[21] A C++ implementation of these GMF models can be found in Unger & Farrar (2024).

The comprehensive study presented here significantly improves our knowledge of the global structure of the coherent magnetic field of the Milky Way and for the first time provides a range of model possibilities to explore the impact of GMF uncertainties on GMF-sensitive science. However, it is just a step in the journey to achieving accurate knowledge of the magnetic field of the Galaxy. Directions for future improvements of the GMF modeling have been noted throughout this paper. These include a better understanding of Galactic foregrounds, an investigation of a possible position dependence of the striation factor, and a self-consistent modeling of the diffusion of cosmic-ray electrons in the GMF.

Acknowledgments

We would like to thank Denis Allard, Rainer Beck, Katia Ferrière, Michael Kachelriess, Jens Kleimann, Alexander Korochkin, and Darko Veberič for useful comments on this manuscript. M.U. acknowledges the support of the EU-funded Marie Curie Outgoing Fellowship, grant PIOF-GA-2013-624803, for part of this work and the hospitality of CCPP/NYU. The research of G.R.F. has been supported by NASA grant NNX10AC96G and NSF grants NSF-PHY-1212538, NSF-PHY-1517319, and NSF-PHY-2013199 and by the Simons Foundation.

We acknowledge the use of the Legacy Archive for Microwave Background Data Analysis (LAMBDA), part of the High Energy Astrophysics Science Archive Center (HEASARC). HEASARC/LAMBDA is a service of the Astrophysics Science Division at the NASA Goddard Space Flight Center. This work has benefited from discussions during the program "Toward a Comprehensive Model of the Galactic Magnetic Field" at NORDITA in 2023 April, which is partly supported by NordForsk and the Royal Astronomical Society.

Software: The results of this paper have been derived using the software packages HEALPIX (Górski et al. 2005), Offline (Argiro et al. 2007), and ROOT (Brun & Rademakers 1997).

Appendix A
Comparison of Synchrotron Data Products

Sky maps of the Stokes Q and U parameters of the polarized synchrotron emission are shown in the subpanels along the diagonal of Figure 22. The values are from the 9 yr WMAP

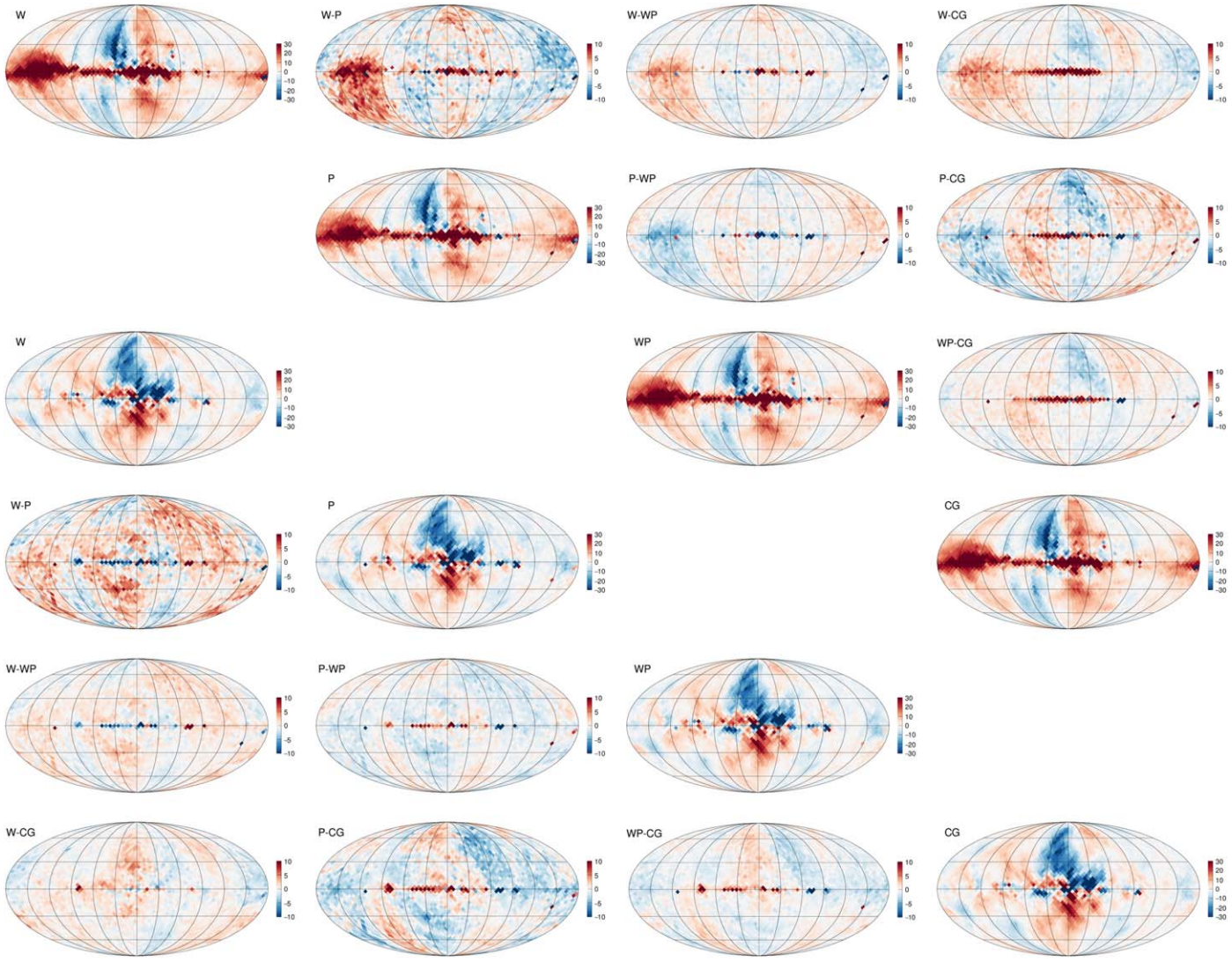

Figure 22. Values (diagonal) and differences (off-diagonal) of Stokes parameters at 30 GHz in μK of WMAP (W), Planck (P), our arithmetic average of WMAP and Planck (WP), and the WMAP–Planck combination of the COSMOGLOBE collaboration (CG). Stokes Q parameters are shown as an upper triangular matrix of plots at the top, and Stokes U parameters are displayed as a lower triangular matrix of plots at the bottom. Values are given in μK.

"base" model (Bennett et al. 2013), the third Planck data release (DR3.0; Akrami et al. 2020), our simple arithmetic average of WMAP and Planck, and the COSMOGLOBE results derived from a combined analysis of WMAP and Planck data (Watts et al. 2023). The difference between each data set is shown as sky maps in the off-diagonal panels. As can be seen, the WMAP and Planck maps exhibit large differences in the Galactic plane that could be related to different levels of temperature-to-polarization leakage in the two data sets (Svalheim et al. 2023). This region of the sky is, however, not relevant for our analysis, as it is masked in the fit. Moreover, there are large-scale systematic differences between the Q and U parameters derived by the two collaborations. Our arithmetic average is by construction in between the two data products, and the values from the global reanalysis from COSMOGLOBE show yet another large-scale distribution of Q and U differences.

Appendix B
Foreground Contamination

An important challenge for the inference of the global structure of the large scale of the GMF is the contamination of the observables with foreground structures (e.g., Section 5.2 in Jaffe 2019). If these structures are sufficiently close to the observer, they can appear as features of large angular extent and could either be mistaken for large-scale global features of the GMF and/or bias the fitted parameters.

A foreground of particular importance is the known loops and spurs of nearby supernova remnants. We performed a few initial tests with a magnetic field compressed at the edge of a local foreground bubble (e.g., Ferriere et al. 1991) using a simple spherical model with magnetic flux conservation but could not find a configuration that described the data. More systematic studies are needed to definitively exclude this possibility, e.g., including the known loops in the PI. It should, however, be noted that we have masked the edges of the classical loops I–IV from our fit, see Section 3.2, also excluding the possible imprint of local filamentary magnetic structures suggested by West et al. (2021). Furthermore, given the angular positions of the loops, it is not obvious how they could conspire to create a foreground that appears as a north–south symmetric poloidal field with $\Delta B_{\rm p} = (0.12 \pm 0.07)\,\mu$G; see Section 7.6.

A similar argument can be brought forward regarding the possibility that the butterfly pattern of the RMs, Equation (9), is the imprint of the local environment as, e.g., suggested by the identification of visually similar features identified in RM sky maps derived from simulated galaxies (e.g., Pakmor et al. 2018; Reissl et al. 2023). Our finding that for all model variations the magnitudes of the northern and southern magnetic field strength of the toroidal component are compatible within a few tenths of μG (see Table 3) is difficult to reconcile with an origin of ordered fields on scales of 1–2 kpc.

For a data-driven test of the influence of unmodeled local structures on the model parameters, we repeat the fit of the `base` model excluding pixels with a large deviation of the data from the model. We exclude pixels if the magnitude of the "pull" = ((data – model)/uncertainty) exceeds 1.5; see Figure 10. The resulting masks for the RMs and PI are displayed in Figure 23, where the additionally masked pixels are shown in blue. As can be seen, the new mask excludes the pixels below the fan region with large RM residuals centered at $(\ell,\ b) \sim (120^\circ,\ -30^\circ)$ and pixels around the already-masked Gum nebula centered at $(\ell,\ b) \sim (105^\circ,\ -9^\circ)$. The additionally masked pixels in PI are mainly at the edge of the existing mask close to the north polar spur (or loop I) and at the northern edge of loop III centered at $(\ell,\ b) \sim (124^\circ,\ 15^\circ)$. Excluding these pixels removes 1320 data points from the fit, i.e., a reduction of about 20%. After reoptimizing the parameters, we find a drastically changed fit quality that improves from a reduced χ^2 of 1.20 for the default fit to 0.47. Note that a reduced χ^2 as low as this value would usually be considered suspicious ("too good") and could indicate that the pull cut is too tight, removing too many pixels. On the other hand, it could result from a small coherence length of the magnetic turbulence, as indicated by our analysis of simulated sky maps discussed in Section 6.

The parameters from the fit with the data-driven mask are compared to the default ones in Figure 24. As can be seen, even after the removal of 20% of the data points, the fit parameters are qualitatively similar. The parameters of the poloidal field are impacted the least by the change of the data set, and also the field strengths and the pitch angle of the disk field component change very little. The most significant changes are observed for the toroidal field for which the magnitudes of the northern and southern field strengths are reduced by about 0.6 μG. We verified that this change is driven by the RM pixels below the fan region. Since similarly low values of the toroidal field strengths were obtained for the `synCG` model, these changes can be considered to be within the overall modeling uncertainties bracketed by the model ensemble presented in this paper.

These studies with a more restrictive mask make it plausible that our modeling is not largely driven by local features.

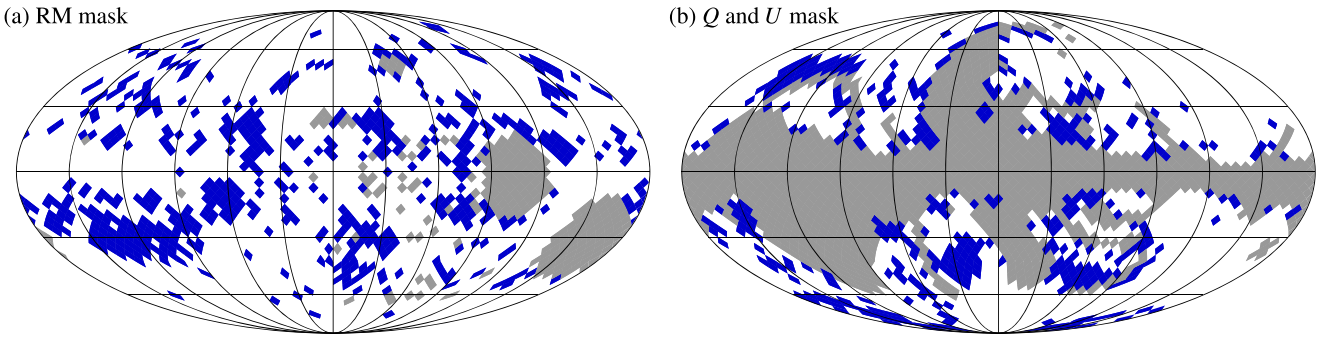

Figure 23. Pixel masks in Galactic coordinates. Left: RM. Right: PI (Stokes Q and U parameters). The gray pixels are masked in the standard analysis (see Sections 3.1 and 3.2), and the additionally masked pixels based on the "pull" are shown in blue (see text).

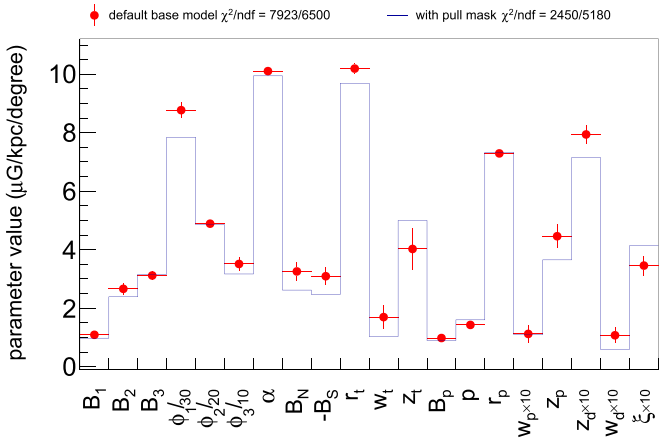

Figure 24. Fit parameters of the `base` model obtained with the standard pixel mask (red points with uncertainties) and with the conservative "pull" mask shown in Figure 23.

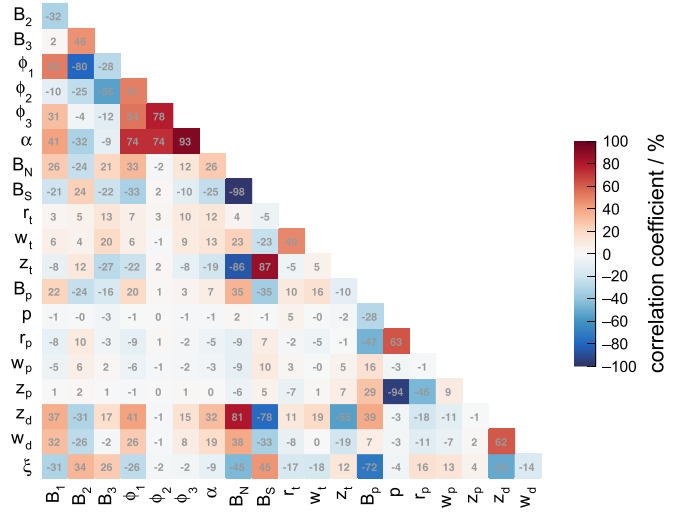

Figure 25. Visualization of the correlation matrix of the 20 parameters of the `base` model.

However, the changes of the model parameters in Figure 24 also demonstrate the gain in precision that could be achieved after including a description of the local magnetized environment to the fit, in particular modeling the Local Bubble and loops along the lines of, e.g., Alves et al. (2018) and Mertsch & Sarkar (2013).

Appendix C
Parameter Correlations

We estimate the covariance matrix $\boldsymbol{V}$ of the best-fit parameters $\hat{\boldsymbol{p}}$ from the second derivatives of the χ^2 at the minimum,

$$V_{ij}^{-1}(\hat{\boldsymbol{p}}) = \frac{1}{2}\left(\frac{\partial^2\chi^2}{\partial p_i \partial p_j}\right)_{\boldsymbol{p}=\hat{\boldsymbol{p}}} \tag{C1}$$

(e.g., Frodesen et al. 1979). We evaluate Equation (C1) using central differences with one Richardson extrapolation (e.g., Press et al. 2002) because for our 20-parameter fits, MINUIT's HESSE algorithm often resulted in numerically unsatisfactory results. The step size for our numerical differentiation is $\Delta x_i = \alpha\,\sigma_i$, where σ_i denotes the uncertainty of parameter i estimated with MINOS (see Section 6). The common scale parameter α is decreased until the differences $||\boldsymbol{V}(\alpha_{k+1}) - \boldsymbol{V}(\alpha_k)||$ between iterations k increase, indicating the onset of numerical noise, typically $\alpha = 0.05$.

As an example, we show the correlation matrix ($\rho_{ij} = V_{ij}/\sqrt{V_{ii}V_{jj}}$) of the parameters of the `base` model in Figure 25. As can be seen, most parameters have low correlation coefficients indicating, e.g., a good factorization of the shape of the toroidal GMF from the other components of the model. However, some parameters are highly (anti) correlated. The two-dimensional profile likelihood contour of the eight parameter combinations with the highest (anti) correlation is shown in Figure 26. Here we also superimposed the approximation derived from Equation (C1) demonstrating good agreement with the numerical scan.

Particularly interesting is the large anticorrelation of the field strengths of the toroidal halo, B_N and B_S. This anticorrelation is introduced by the common scale height z_t. We tested a fit of separate scale heights in the north and south but found only a minor improvement in fit quality when leaving them separately free in the fit ($\delta\chi^2 = -22$).

In addition to being a valuable diagnostic for the correlation of fit parameters, the covariance matrix is essential to propagate the uncertainties of the parameters. For numerical applications, the simplest method for the error propagation is to draw samples $\tilde{\boldsymbol{p}}$ of the parameter vector $\boldsymbol{p}$ that are distributed according to the covariance matrix. This can, for instance, be achieved via

$$\tilde{\boldsymbol{p}} = \hat{\boldsymbol{p}} + \boldsymbol{L}\boldsymbol{n}, \tag{C2}$$

where $\boldsymbol{L}$ is the lower triangular matrix of the Cholesky decomposition of the covariance matrix, $\boldsymbol{V} = \boldsymbol{L}\boldsymbol{L}^\mathrm{T}$, and $\boldsymbol{n}$ denotes a vector of standard-normally distributed random numbers.

How these samples can be used for error propagation is illustrated in Figure 27. Here we show the backtracked directions of particles starting on a grid of arrival directions at Earth similar to Figure 19. For each grid point, we backtracked 100 particles, each through a different version of the `base` model using a different draw of the parameter vector. The point density is a direct measure of the probability of a particular direction given the covariance of the fitted parameters. For most of the grid points, the standard deviation of the points is smaller than the difference between models in Figure 19, showing that the systematic differences between models dominate over the parameter uncertainties. The sampling of the parameters from the covariance matrix can nevertheless be useful, for instance, if instead of a discrete eightfold uncertainty, mapping a smoother distribution is needed, which may be obtained by sampling the parameters of all eight model variants. The numerical values of the elements of V for the eight GMF models as well as an example for the sampling according to Equation (C2) are available in Unger & Farrar (2024).

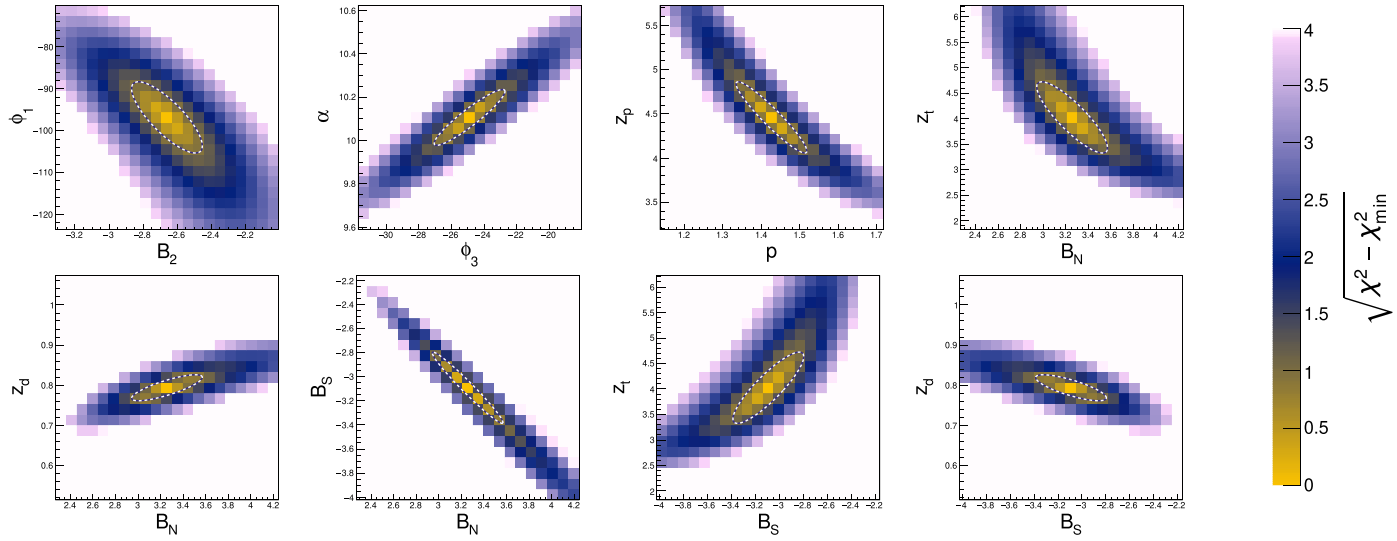

Figure 26. Profile likelihood scan of the eight parameter pairs of the `base` model with the largest (anti)correlation (units are μG, degree, and kpc as in Table 1); the color scale denotes the deviation of the fit quality from the optimum. The dashed ellipses show the approximate 1σ contour derived from the covariance matrix.

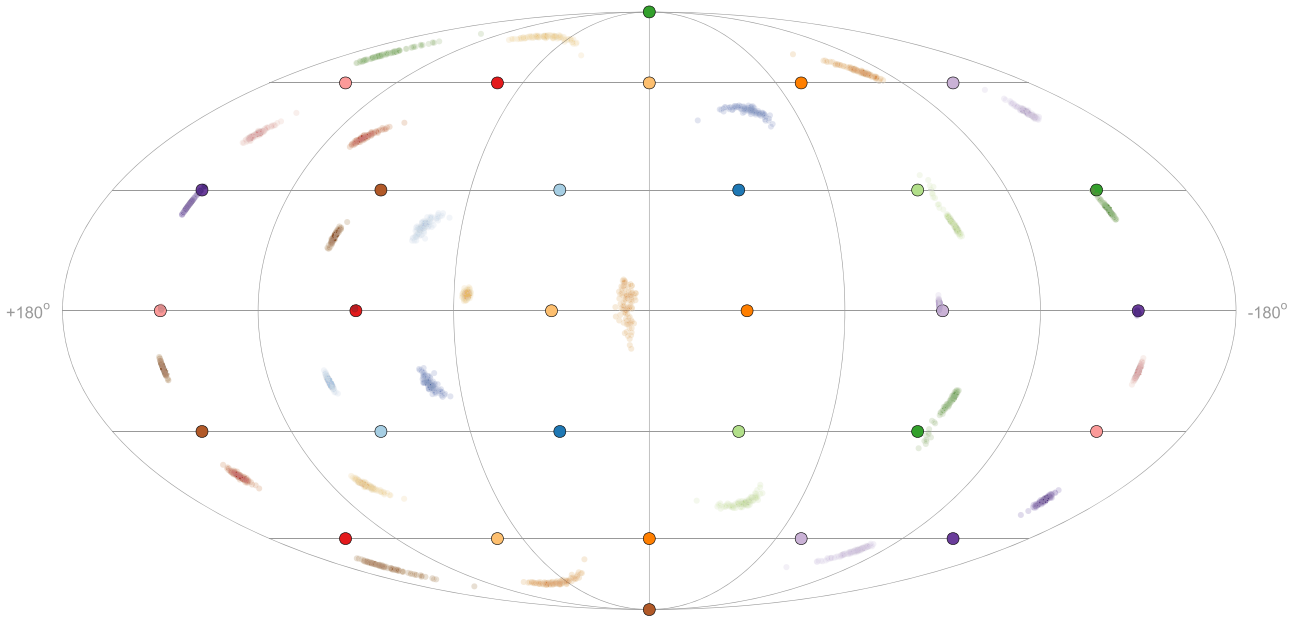

Figure 27. Propagation of parameter uncertainties to deflection uncertainties. Large filled circles denote a grid of arrival directions at Earth. Small transparent points of the same color show the backtracked directions at the edge of the Galaxy using the `base` model and a rigidity of $\mathcal{R} = 20$ EV. For every arrival direction, 100 sets of model parameters are drawn randomly from the covariance matrix, and a cosmic ray is backtracked in the corresponding field.

ORCID iDs

Michael Unger https://orcid.org/0000-0002-7651-0272
Glennys R. Farrar https://orcid.org/0000-0003-2417-5975

References

Abbasi, R. U., Abe, M., Abu-Zayyad, T., et al. 2014, ApJL, 790, L21
Abreu, P., Aglietta, M., Albury, J. M., et al. 2022, ApJ, 935, 170
Abuter, R., Amorim, A., Bauböck, M., et al. 2019, A&A, 625, L10
Ackermann, M., Albert, A., Atwood, W. B., et al. 2014, ApJ, 793, 64
Adam, R., Ade, P. A. R., Alves, M. I. R., et al. 2016, A&A, 596, A103
Ade, P. A. R., Aghanim, N., Arnaud, M., et al. 2014, A&A, 566, A54
Ade, P. A. R., Alves, M. I. R., Aniano, G., et al. 2015, A&A, 576, A107
Adriani, O., Barbarino, G. C., Bazilevskaya, G. A., et al. 2009, Natur, 458, 607
Aguilar, M., Aisa, D., Alpat, B., et al. 2014, PhRvL, 113, 221102
Aguilar, M., Aisa, D., Alpat, B., et al. 2015, PhRvL, 114, 171103
Aguilar, M., Ali Cavasonza, L., Ambrosi, G., et al. 2019, PhRvL, 122, 041102
Akrami, Y., Ashdown, M., Aumont, J., et al. 2020, A&A, 641, A4
AL-Zetoun, A., & Achterberg, A. 2018, MNRAS, 477, 1258
Alves, M. I. R., Boulanger, F., Ferrière, K., & Montier, L. 2018, A&A, 611, L5
Anderson, C. S., Gaensler, B. M., Feain, I. J., & Franzen, T. M. O. 2015, ApJ, 815, 49
Anderson, L. D., Bania, T. M., Balser, D. S., et al. 2014, ApJS, 212, 1
Andreasyan, R. R., & Makarov, A. N. 1988, Ap, 28, 247
Argiro, S., Barroso, S., Gonzalez, J., et al. 2007, NIMPA, 580, 1485
Beck, R. 2016, A&ARv, 24, 4
Beck, R., Shukurov, A., Sokoloff, D., & Wielebinski, R. 2003, A&A, 411, 99
Bennett, C. L., et al. 2013, ApJS, 208, 20
Berkhuijsen, E. M., Haslam, C. G. T., & Salter, C. J. 1971, A&A, 14, 252
Betti, S. K., Hill, A. S., Mao, S. A., et al. 2019, ApJ, 871, 215
Blasi, P. 2023, arXiv:2307.11640
Bradt, H. 2008, Astrophysics Processes (Cambridge: Cambridge Univ. Press)
Brandenburg, A., & Ntormousi, E. 2023, ARA&A, 61, 561
Broderick, J. W., Bryant, J. J., Hunstead, R. W., Sadler, E. M., & Murphy, T. 2007, MNRAS, 381, 341
Broten, N. W., MacLeod, J. M., & Vallee, J. P. 1988, Ap&SS, 141, 303

Brown, J. C., Haverkorn, M., Gaensler, B. M., et al. 2007, ApJ, 663, 258
Brown, J. C., Taylor, A. R., & Jackel, B. J. 2003, ApJS, 145, 213
Brun, R., & Rademakers, F. 1997, NIMPA, 389, 81
Carretti, E., Crocker, R. M., Staveley-Smith, L., et al. 2013, Natur, 493, 66
Cash, J., & Karp, A. 1990, ACM Trans. Math. Soft., 16, 201
Condon, J. J., Cotton, W. D., Greisen, E. W., et al. 1998, AJ, 115, 1693
Cordes, J. M., & Lazio, T. J. W. 2002, arXiv:astro-ph/0207156
Cummings, A. C., Stone, E. C., Heikkila, B. C., et al. 2016, ApJ, 831, 18
Dessert, C., Foster, J. W., & Safdi, B. R. 2020, PhRvL, 125, 261102
Di Bernardo, G., Evoli, C., Gaggero, D., Grasso, D., & Maccione, L. 2013, JCAP, 03, 036
Di Mauro, M., Donato, F., Fornengo, N., Lineros, R., & Vittino, A. 2014, JCAP, 04, 006
Evoli, C., Gaggero, D., Grasso, D., & Maccione, L. 2008, JCAP, 10, 018
Evoli, C., Morlino, G., Blasi, P., & Aloisio, R. 2020, PhRvD, 101, 023013
Farnes, J. S., Gaensler, B. M., & Carretti, E. 2014, ApJS, 212, 15
Farrar, G. R. 2014, CRPhy, 15, 339
Feain, I. J., Ekers, R. D., Murphy, T., et al. 2009, ApJ, 707, 114
Ferrière, K., & Terral, P. 2014, A&A, 561, A100
Ferrière, K., West, J. L., & Jaffe, T. R. 2021, MNRAS, 507, 4968
Ferriere, K. M., Mac Low, M.-M., & Zweibel, E. G. 1991, ApJ, 375, 239
Finkbeiner, D. P. 2003, ApJS, 146, 407
Fletcher, R. 1970, CompJ, 13, 317
Fletcher, R., & Powell, M. J. D. 1963, CompJ, 6, 163
Frodesen, A. G., Skjeggestad, O., & Tofte, H. 1979, Probability and Statistics in Particle Physics (Bergen: Universitetsforlaget)
Gabici, S., Evoli, C., Gaggero, D., et al. 2019, IJMPD, 28, 1930022
Gaensler, B. M., Madsen, G. J., Chatterjee, S., & Mao, S. A. 2008, PASA, 25, 184
Génolini, Y., et al. 2019, PhRvD, 99, 123028
Giacalone, J., & Jokipii, J. R. 1999, ApJ, 520, 204
Giacinti, G., Kachelriess, M., & Semikoz, D. V. 2018, JCAP, 07, 051
Ginzburg, V. L., & Syrovatskii, S. I. 1964, The Origin of Cosmic Rays (Oxford: Pergamon)
Goldreich, P., & Sridhar, S. 1995, ApJ, 438, 763
Górski, K. M., Hivon, E., Banday, A. J., et al. 2005, ApJ, 622, 759
Han, J. L., Manchester, R. N., Berkhuijsen, E. M., & Beck, R. 1997, A&A, 322, 98
Han, J. L., Manchester, R. N., van Straten, W., & Demorest, P. 2018, ApJS, 234, 11
Harvey-Smith, L., Madsen, G. J., & Gaensler, B. M. 2011, ApJ, 736, 83
Haverkorn, M., & Heesen, V. 2012, SSRv, 166, 133
Heald, G., Braun, R., & Edmonds, R. 2009, A&A, 503, 409
Heiles, C., Chu, Y. H., & Troland, T. H. 1981, ApJL, 247, L77
Hogg, D. W., & Foreman-Mackey, D. 2018, ApJS, 236, 11
Hooper, D., Blasi, P., & Serpico, P. D. 2009, JCAP, 01, 025
Hou, L. G., & Han, J. L. 2014, A&A, 569, A125
Iroshnikov, P. S. 1964, SvA, 7, 566
Jaeckel, J., & Ringwald, A. 2010, ARNPS, 60, 405
Jaffe, T. R. 2019, Galax, 7, 52
Jaffe, T. R., Leahy, J. P., Banday, A. J., et al. 2010, MNRAS, 401, 1013
James, F., & Roos, M. 1975, CoPhC, 10, 343
Jansson, R., & Farrar, G. R. 2012a, ApJ, 757, 14
Jansson, R., & Farrar, G. R. 2012b, ApJL, 761, L11
Jansson, R., Farrar, G. R., Waelkens, A. H., & Ensslin, T. A. 2009, JCAP, 07, 021
Joshi, J. C., & Razzaque, S. 2017, JCAP, 09, 029
Joshi, Y. C., Dambis, A. K., Pandey, A. K., & Joshi, S. 2016, A&A, 593, A116
Kaczmarek, J. F., Purcell, C. R., Gaensler, B. M., McClure-Griffiths, N. M., & Stevens, J. 2017, MNRAS, 467, 1776
Kalberla, P. M. W., & Kerp, J. 2009, ARA&A, 47, 27
Kleimann, J., Schorlepp, T., Merten, L., & Becker Tjus, J. 2019, ApJ, 877, 76
Klein, U., Mack, K.-H., Gregorini, L., & Vigotti, M. 2003, A&A, 406, 579
Kraichnan, R. H. 1965, PhFl, 8, 1385
Krause, M., Irwin, J., Schmidt, P., et al. 2020, A&A, 639, A112
Kuhlen, M., Phan, V. H. M., & Mertsch, P. 2022, arXiv:2211.05882
Laing, R. A. 1980, MNRAS, 193, 439
Lallement, R. 2023, CRPhy, 23, 1
Levine, E. S., Blitz, L., & Heiles, C. 2006, ApJ, 643, 881
Levine, E. S., Heiles, C., & Blitz, L. 2008, ApJ, 679, 1288
Longair, M. S. 2011, High Energy Astrophysics (Cambridge: Cambridge Univ. Press)
Lorimer, D. R., Faulkner, A. J., Lyne, A. G., et al. 2006, MNRAS, 372, 777
Ma, Y. K., Mao, S. A., Ordog, A., & Brown, J. C. 2020, MNRAS, 497, 3097
Ma, Y. K., Mao, S. A., Stil, J., et al. 2019, MNRAS, 487, 3432
Majaess, D. J., Turner, D. G., & Lane, D. J. 2009, MNRAS, 398, 263
Manchester, R. N. 1972, ApJ, 172, 43
Manchester, R. N., Hobbs, G. B., Teoh, A., & Hobbs, M. 2005, AJ, 129, 1993
Mao, S. A., Gaensler, B. M., Haverkorn, M., et al. 2010, ApJ, 714, 1170
Mao, S. A., McClure-Griffiths, N. M., Gaensler, B. M., et al. 2012a, ApJ, 755, 21
Mao, S. A., McClure-Griffiths, N. M., Gaensler, B. M., et al. 2012b, ApJ, 759, 25
Maurin, D., Donato, F., Taillet, R., & Salati, P. 2001, ApJ, 555, 585
Maurin, D., Ferronato Bueno, E., & Derome, L. 2022, A&A, 667, A25
Men, H., & Han, J. L. 2003, AcASn, 44, 151
Merten, L., Becker Tjus, J., Fichtner, H., Eichmann, B., & Sigl, G. 2017, JCAP, 06, 046
Mertsch, P. 2018, JCAP, 11, 045
Mertsch, P., & Sarkar, S. 2013, JCAP, 06, 041
Meyer, M., Davies, J., & Kuhlmann, J. 2022, ICRC (Berlin), 37, 557
Moskalenko, I. V., & Strong, A. W. 1998, ApJ, 493, 694
Orlando, E. 2018, MNRAS, 475, 2724
Orlando, E., & Strong, A. 2013, MNRAS, 436, 2127
O'Sullivan, S. P., Purcell, C. R., Anderson, C. S., et al. 2017, MNRAS, 469, 4034
O'Sullivan, S. P., Shimwell, T. W., Hardcastle, M. J., et al. 2023, MNRAS, 519, 5723
Pakmor, R., Guillet, T., Pfrommer, C., et al. 2018, MNRAS, 481, 4410
Pakmor, R., Marinacci, F., & Springel, V. 2014, Astrophys. J. Lett., 783, L20
Parker, E. N. 1979, Cosmical Magnetic Fields: their Origin and their Activity (Oxford: Oxford Univ. Press)
Porter, T. A., Jóhannesson, G., & Moskalenko, I. V. 2017, ApJ, 846, 67
Predehl, P., Sunyaev, R. A., Becker, W., et al. 2020, Natur, 588, 227
Press, W. H., Teukolsky, S. A., Vetterling, W. T., & Flannery, B. P. 2002, Numerical Recipes in C++ : The Art of Scientific Computing (Cambridge: Cambridge Univ. Press)
Price, D. C., Flynn, C., & Deller, A. 2021, PASA, 38, e038
Prouza, M., & Šmída, R. 2003, A&A, 410, 1
Pshirkov, M. S., Tinyakov, P. G., Kronberg, P. P., & Newton-McGee, K. J. 2011, ApJ, 738, 192
Raffelt, G., & Stodolsky, L. 1988, PhRvD, 37, 1237
Reid, M. J., Menten, K. M., Brunthaler, A., et al. 2014, ApJ, 783, 130
Reid, M. J., Menten, K. M., Brunthaler, A., et al. 2019, ApJ, 885, 131
Reissl, S., Klessen, R. S., Pellegrini, E. W., et al. 2023, NatAs, 7, 1295
Riseley, C. J., Galvin, T. J., Sobey, C., et al. 2020, PASA, 37, e029
Ryden, B., & Pogge, R. W. 2021, Interstellar and Intergalactic Medium (Cambridge: Cambridge Univ. Press)
Schnitzeler, D. H. F. M. 2012, MNRAS, 427, 664
Schnitzeler, D. H. F. M., Carretti, E., Wieringa, M. H., et al. 2019, MNRAS, 485, 1293
Schwarz, G. 1978, AnSta, 6, 461
Seta, A., & Federrath, C. 2021, PhRvF, 6, 103701
Simard-Normandin, M., Kronberg, P. P., & Button, S. 1981, ApJS, 45, 97
Spoelstra, T. A. T. 1973, A&A, 24, 149
Stanev, T. 1997, ApJ, 479, 290
Strong, A. W., & Moskalenko, I. V. 1998, ApJ, 509, 212
Sun, X.-H., & Reich, W. 2010, RAA, 10, 1287
Sun, X. H., Reich, W., Waelkens, A., & Enßlin, T. A. 2008, A&A, 477, 573
Svalheim, T. L., Zonca, A., Andersen, K. J., et al. 2023, A&A, 675, A9
Taylor, A. R., Stil, J. M., & Sunstrum, C. 2009, ApJ, 702, 1230
Terral, P., & Ferrière, K. 2017, A&A, 600, A29
Unger, M., & Farrar, G. R. 2018, ICRC (Busan), 301, 558
Unger, M., & Farrar, G. R. 2019, in EPJ Web Conf. 210, Ultra High Energy Cosmic Rays 2018 (UHECR 2018), ed. I. Lhenry-Yvon et al., 04005
Unger, M., & Farrar, G. R. 2024, The Coherent Magnetic Field of the Milky Way, v1.0, Zenodo, doi:10.5281/zenodo.10627090
Vallée, J. P. 2022, NewA, 97, 101896
Van Eck, C. L., Brown, J. C., Shukurov, A., & Fletcher, A. 2015, ApJ, 799, 35
Van Eck, C. L., Brown, J. C., Stil, J. M., et al. 2011, ApJ, 728, 97
Van Eck, C. L., Brown, J. C., Ordog, A., et al. 2021, ApJS, 253, 48
Van Eck, C. L., Gaensler, B. M., Hutschenreuter, S., et al. 2022, RMTable Consolidated Catalog of Faraday Rotation Measures of Astronomical Radio Sources, v1.1.0, Zenodo, doi:10.5281/zenodo.7894467
Van Eck, C. L., Gaensler, B. M., Hutschenreuter, S., et al. 2023, ApJS, 267, 28
Vidal, M., Dickinson, C., Davies, R. D., & Leahy, J. P. 2015, MNRAS, 452, 656
Wardle, J. F. C., & Kronberg, P. P. 1974, ApJ, 194, 249
Watts, D. J., Basyrov, A., Eskilt, J. R., et al. 2023, A&A, 679, A143
Watts, D. J., Fuskeland, U., Aurlien, R., et al. 2024, A&A, 689, A297
Weinrich, N., Boudaud, M., Derome, L., et al. 2020, A&A, 639, A74
West, J. L., Landecker, T. L., Gaensler, B. M., Jaffe, T., & Hill, A. S. 2021, ApJ, 923, 58
Wilks, S. S. 1938, Annals Math. Statist., 9, 60
Workman, R. L., Burkert, V. D., Crede, V., et al. 2022, PTEP, 2022, 083C01
Xu, J., & Han, J.-L. 2014, RAA, 14, 942
Yao, J. M., Manchester, R. N., & Wang, N. 2017, ApJ, 835, 29
Yuan, Q., Lin, S.-J., Fang, K., & Bi, X.-J. 2017, PhRvD, 95, 083007